Quantitative CT Perfusion Analysis in Ischemic Stroke

Edwin Bennink

Quantitative CT Perfusion Analysis in Ischemic Stroke
Edwin Bennink

Ph.D. thesis, Utrecht University, the Netherlands

Quantitative CT Perfusion Analysis in Ischemic Stroke

Kwantitatieve CT-perfusieanalyse bij een herseninfarct
(*met een samenvatting in het Nederlands*)

Proefschrift

ter verkrijging van de graad van doctor aan de Universiteit Utrecht op gezag van de rector magnificus, prof. dr. G.J. van der Zwaan, ingevolge het besluit van het college voor promoties in het openbaar te verdedigen op dinsdag 15 maart 2016 des middags te 4.15 uur

door

Hendrik Eduard Bennink
geboren op 2 april 1982 te Deventer

Promotor: Prof. dr. ir. M.A. Viergever

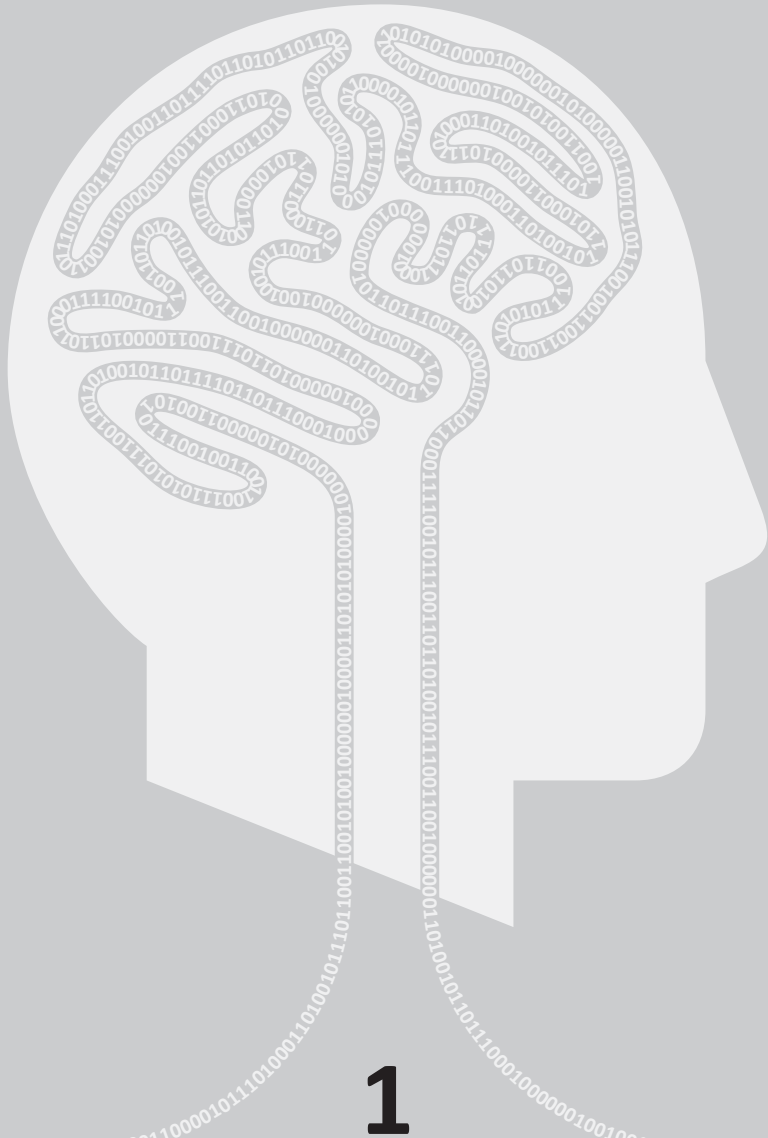Copromotoren: Dr. ir. H.W.A.M. de Jong
                      Dr. B.K. Velthuis
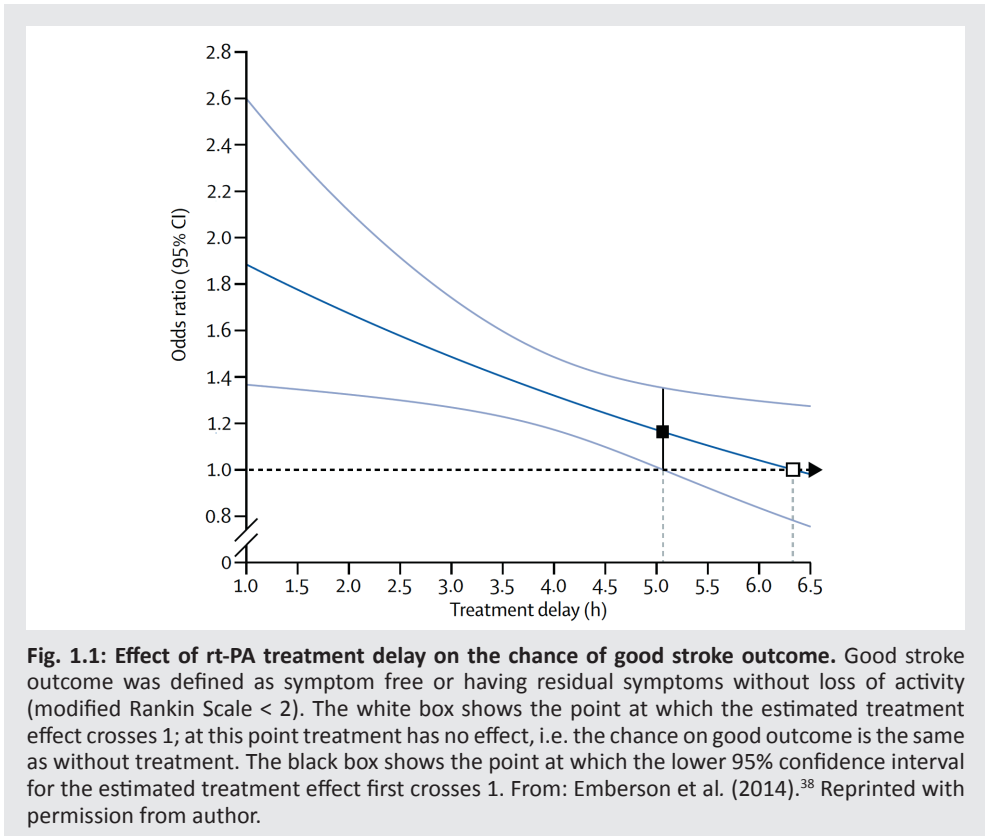
CONTENTS

1

Introduction

CT perfusion imaging has become established as a method of choice for the assessment of ischemic stroke. However, current CT perfusion analysis methods have several shortcomings and do not exploit the imaging technique to its full potential. This thesis presents an analysis method that is intrinsically robust and flexible. The method may furthermore aid in predicting hemorrhagic transformation; an adverse effect of thrombolytic stroke treatment. The application of this method to thin slice, high-resolution scans may well improve the diagnostic and prognostic value of CT perfusion imaging.

1.1 TIME IS BRAIN

"*Time is brain!*" This is a frequently heard phrase in stroke treatment, emphasizing that rapid diagnosis and therapy is required as brain tissue is quickly lost as stroke progresses.[46] Rapid, effective treatment can prevent long-term disability and save lives.

   The clinical use of thrombolytic (blood clot dissolving) drugs in the 1990's, recombinant tissue plasminogen activator (rt-PA) in particular, enabled active treatment of acute ischemic stroke rather than providing supportive therapy alone.[111] rt-PA was first used to treat acute myocardial infarction and later approved for use in ischemic stroke. The earlier rt-PA is used, the more beneficial it is; shorter treatment delay results in a much greater treatment effect (Fig. 1.1). When treated within 3 hours of symptom onset, it results in an overall benefit of 10% with respect to living without disability, although it has the adverse effect of increasing the risk of developing symptomatic intracranial hemorrhages which also increases the risk of early death.[38,89,140] It was found that 2% of stroke patients who do not receive rt-PA treatment develop space-occupying hematoma, versus 10% of the patients who do receive this treatment.[15] The treatment improves outcome if given up to 4.5 hours after onset, but effects of later treatment are unclear and still being tested. No baseline clinical variables are known to predict hemorrhage due to rt-PA treatment.[142]

   A thorough Cochrane review study by Wardlaw et al. (2014), weighing risks and benefits, advises: "*People who think that they are experiencing a stroke should get to hospital quickly, be assessed by a stroke doctor, have a brain scan and receive clot-dissolving treatment as fast as possible.*"[140]

Fig. 1.1: Effect of rt-PA treatment delay on the chance of good stroke outcome. Good stroke outcome was defined as symptom free or having residual symptoms without loss of activity (modified Rankin Scale < 2). The white box shows the point at which the estimated treatment effect crosses 1; at this point treatment has no effect, i.e. the chance on good outcome is the same as without treatment. The black box shows the point at which the lower 95% confidence interval for the estimated treatment effect first crosses 1. From: Emberson et al. (2014).[38] Reprinted with permission from author.

Thus far, treatment delay is the major criterion for deciding whether or not to give rt-PA treatment. Mainly due to this criterion just 11% of the ischemic stroke patients in the Netherlands are currently found to be eligible for intravenous rt-PA treatment.[12] As described below, this number may be increased by using functional imaging in addition to, or even instead of treatment delay as selection criterion. Besides intravenous thrombolysis (IVT), the thrombolytic drugs may also be administered intra-arterial (IAT), i.e. injected through a microcatheter at the occlusion site. Via the same route as IAT, the thrombus may furthermore be retrieved mechanically (mechanical thrombectomy, MT). Although delaying treatment, intra-arterial treatment (IAT and/or MT) was recently proven to be safe and effective in patients with a proximal occlusion of the anterior circulation when administered within 6 hours.[16,44]

Functional brain imaging techniques based on X-ray computed tomography (CT), magnetic resonance (MR), positron emission tomography (PET), or single photon emission computed tomography (SPECT) can provide insight in the size and location of the infarcted area, and may identify salvageable tissue. Because of their relatively high resolution,

wide availability, and short preparation and scanning time, CT and MR imaging are most frequently used in stroke. This includes *CT perfusion* (CTP) imaging, diffusion-weighted MR imaging (DWI), and a variety of perfusion-weighted MR imaging (PWI) techniques. These functional imaging techniques have shown to be effective in influencing the selection of patients within, but also beyond the 3 and 4.5 hour window of treatment delay.[19,47,94] In a review study by Burton et al. (2015) it was found that when CTP imaging is used for rt-PA treatment selection by identifying the volume of infarct and salvageable tissue, patients with a treatment delay beyond 3 hours even showed far lower mortality rates and better outcomes than patients treated within 3 hours.[26] These results suggest that more patients beyond current time windows could benefit from thrombolysis with the aid of functional imaging.

Although MR imaging does not use ionizing radiation and allows full brain coverage, CT is still the preferred modality for stroke diagnosis because of its accessibility and simplicity. CT is widely available in the emergency setting and less time consuming than MR, it can be obtained at less cost, and it can be performed at no risk to a patient with metal foreign bodies or implantable medical devices.[126,149]

The aim of the study presented in this thesis is to develop quantitative analysis methods that could increase the effectiveness of functional CT imaging in selecting patients for rt-PA treatment. This includes enhancing current CTP analysis, the use of CTP imaging to estimate the risk of developing hemorrhages, and high-resolution CTP analysis.

1.2 CT IMAGING IN STROKE

A series of multiple concurrent CT imaging techniques, known as *multi-modal* CT, is currently being used for stroke assessment. Each technique has its own qualities, which are described in the next sections.

1.2.1 Non-contrast CT

In the Netherlands, about 84% of the strokes are caused by blockage of a blood vessel (ischemic strokes), whereas the remaining 16% are caused by an intracranial bleeding (hemorrhagic strokes).[36] The primary goal of imaging in acute stroke is to differentiate between these two types. Since the X-ray attenuation coefficient of blood is higher than that of brain tissue, standard *non-contrast CT* (NCCT) can be used to detect hemorrhages (Fig. 1.2). Furthermore, occlusions of large cerebral arteries in early ischemic stroke may also show up on NCCT, which is known as hyperdense artery sign (Fig. 1.3a). Ischemic infarction may be seen as a hypodense area relative to the surrounding tissue.
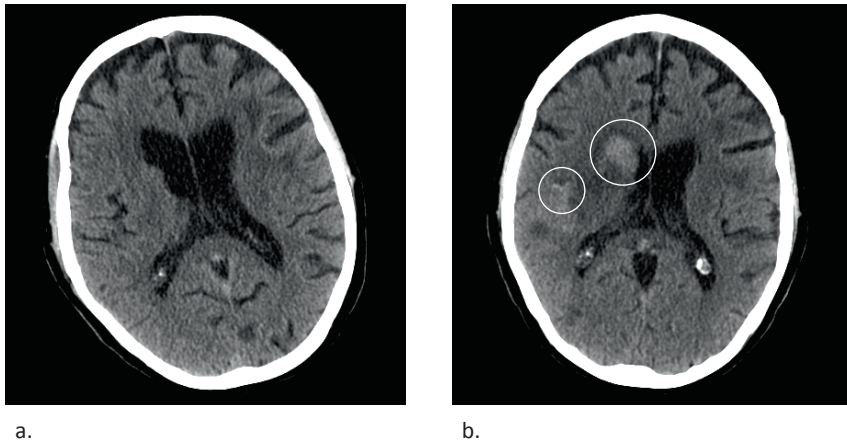
Fig. 1.2: Intracranial bleeding on non-contrast CT. a) A non-contrast CT brain scan without a bleeding. b) A non-contrast CT brain scan showing two hemorrhagic sites in the right hemisphere (encircled).
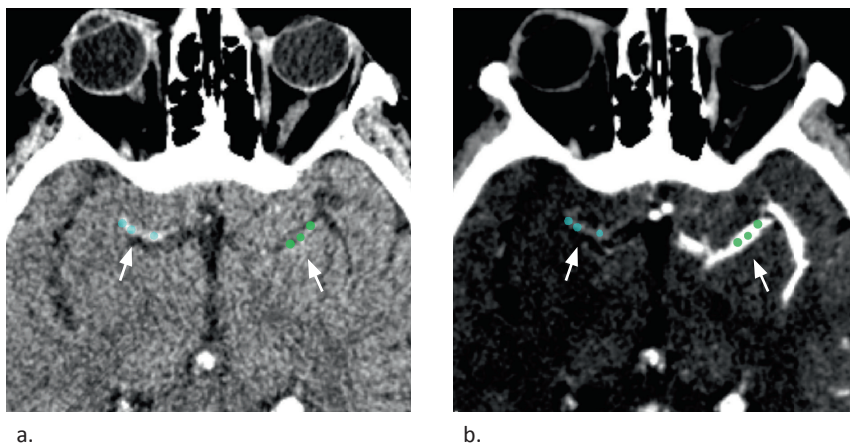
Fig. 1.3: NCCT and CTA showing a hyperdense thrombus. The non-contrast CT image (a) clearly shows a hyperdense right middle cerebral artery thrombus (left in the image). The occlusion due to this thrombus is visible in the CT angiography image (b) as the absence of contrast material. Courtesy of Santos et al. (2015).[122]

1.2.2 CT Angiography

Contrast-enhanced *CT angiography* (CTA) is performed to determine the site and extent of arterial occlusion in ischemic stroke. It is also possible to assess the degree of collateral circulation behind the arterial occlusion. Iodinated contrast material is injected in a

peripheral vein (Fig. 1.4), and the CTA scan is acquired when the intensity of this bolus in the cerebral arteries is maximal (Fig. 1.3b and Fig. 1.5). Since modern CT scanners allow fast helical scanning, a large axial coverage can be achieved, including all vessels ascending from the top of the aortic arch to the vertex of the head.

© MAYO FOUNDATION FOR MEDICAL EDUCATION AND RESEARCH. ALL RIGHTS RESERVED.

Fig. 1.4: Patient undergoing contrast-enhanced CT brain imaging. From left to right; CT scanner, patient on motorized table, dual power injector with contrast material and saline solution, radiologic technologist behind radiation shielding window. Reprinted with permission from Mayo Foundation for Medical Education and Research.

a.

b.

Fig. 1.5: Middle cerebral artery occlusion on CT angiography. A 10 mm thick axial (a) and 15 mm thick coronal (b) maximum-intensity projection showing the cerebral vessels. The arrows indicate the position of the occlusion.

1.2.3 CT Perfusion Imaging

In addition to NCCT and CTA, CTP imaging has become an established method to further diagnose ischemic stroke and individualize treatment. Analogous to CTA, CTP imaging starts with the injection of a bolus of iodinated contrast mater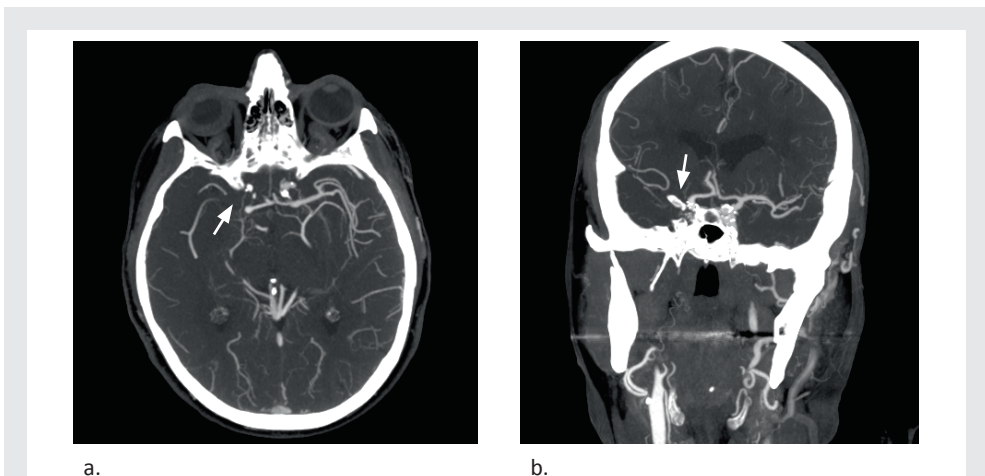ial, but instead of a single CT scan, a series of scans is acquired that tracks the bolus passage through the brain over time (Fig. 1.6). By means of *tracer kinetic analysis*, a number of informative *perfusion maps* can be extracted from this series of scans; this is detailed in Section 1.3. Examination of these perfusion maps gives insight in the perfusion status of the brain tissue, allowing differentiation between healthy tissue, salvageable tissue, and irreversibly infarcted tissue (Fig. 1.7).

Fig. 1.6: Four acquisitions of a CT perfusion series. The first acquisition in the series (0 s) does not show any contrast enhancement yet. The bolus arrived in the brain at about 12 s after, and the large arteries clearly show up enhanced on the scan acquired at 16 s. At 20 s the enhancement is maximal throughout the brain, and at 30s only the veins are still clearly enhanced.

Fig. 1.7: CT perfusion maps. Parameter maps showing cerebral blood flow (a), cerebral blood volume (b), and mean transit time (c). d) A so-called summary map, in which salvageable tissue is colored green, and irreversibly infarcted tissue color red. These images clearly show a perfusion defect in the perfusion area of the middle cerebral artery of the right hemisphere (left in the image). Screenshots from Philips Extended Brilliance Workspace 4.0.

In order to track a complete bolus passage through the brain, the total scan duration needs to be in the order of one minute. For the CTP scans used in the studies in this thesis, 25 CT volumes were acquired at an interval of approximately 2 s, resulting in a total duration of

50 s. Although this is sufficient for calculating the conventional perfusion maps, this duration may be too short to estimate vascular *permeability*, which is explained in more detail in Sections 1.3.2 and 1.3.3. For this reason the standard protocol was *extended* by 6 additional CT volumes at an interval of approximately 30 s, resulting in a total duration of 210 s. Section 1.4 explains the scan protocol in more detail.

Although CT brain perfusion imaging has been possible since the early eighties, clinical practice had to wait for this technology to become available until the introduction of multi-slice CT scanners in the late nineties.[103] Because of the improvements in speed and axial coverage it is now possible to acquire large enough volumes in short enough time. Since it is difficult to acquire spiral CT scans at short intervals, axial coverage is often limited by the detector size. Typical multi-slice coverage varies from 40 to 160 mm, but only the largest, 160 mm, provides full brain coverage. Slice thickness is typically 0.5 to 1 mm. In order to reduce dose, data, and processing time, however, scans are often reconstructed with a slice thickness of 5 mm (Fig. 1.8). The slices, with a field-of-view of approximately 200 mm × 200 mm, are reconstructed in a 512 × 512 matrix.
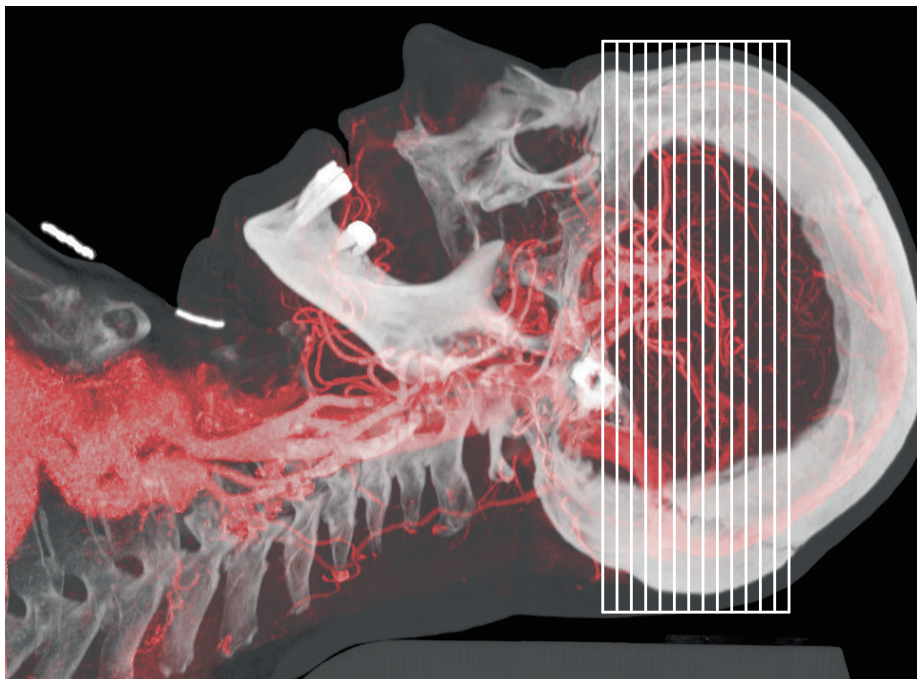

Fig. 1.8: CTA and CTP coverage and slice thickness. A sagittal maximum intensity projection (319 mm × 230 mm) of the vessels in the head and neck as imaged with CT angiography (red), overlaid by a thick sagittal slab highlighting bone (white) and tissue (dark gray). The lines indicate a volume of 13 adjacent 5 mm thick slices as imaged in a typical CT perfusion scan.

Because CTP imaging acquires a contrast bolus passage over time, each voxel of the 3D scan with *N* acquisitions contains a *time-attenuation curve* (TAC) with *N* time points (Fig. 1.9). A voxel with a high blood volume is perfused by high amount of contrast material and therefore it shows high enhancement in its TAC. Because the logarithm of the X-ray attenuation scales linearly with the concentration of contrast material, there also exists a linear relationship between the *enhancement curve* and the change in contrast material concentration. This feature of CT imaging facilitates quantitative analysis. To identify the baseline necessary for calculating contrast enhancement, the contrast material is injected at the same time as the CTP acquisition starts, which means that the first volumes are acquired before the bolus arrives in the brain.
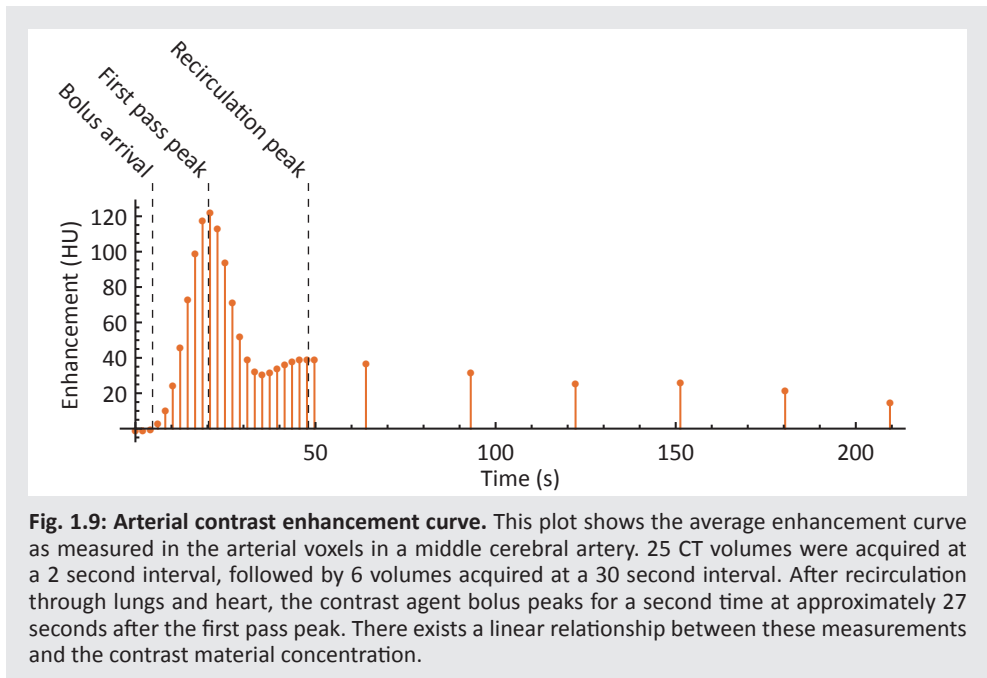
Fig. 1.9: Arterial contrast enhancement curve. This plot shows the average enhancement curve as measured in the arterial voxels in a middle cerebral artery. 25 CT volumes were acquired at a 2 second interval, followed by 6 volumes acquired at a 30 second interval. After recirculation through lungs and heart, the contrast agent bolus peaks for a second time at approximately 27 seconds after the first pass peak. There exists a linear relationship between these measurements and the contrast material concentration.

Despite the many benefits, CT has the disadvantage of exposure to ionizing radiation. A NCCT of the brain is usually acquired at a tube voltage of 120 kV (peak, kVp) and a current-exposure product of 300 mAs.[2] This results in an effective dose of 1 to 3 mSv per acquired volume, which can be compared with an annual effective dose from natural background radiation of approximately 2 to 3 mSv. In order to limit the radiation dose in the sequential acquisition of 25 or more volumes in a CTP series, the volumes are acquired with relatively low X-ray tube current and low exposure time. Most adult brain CTP scans that were used in the studies described in this thesis were acquired at 80 kVp and 150 mAs, as recommended

by the American Association of Physicists in Medicine (AAPM) guidelines.[1] Depending on the axial coverage, this results in an effective dose of 2 to 6 mSv per CTP series. Imaging at 80 kVp instead of 120 kVp not only reduces radiation exposure, but also increases iodine contrast enhancement relative to soft tissue.[148] State-of-the-art iterative reconstruction and filtering techniques may substantially improve image quality and therefore allow acquisition with even lower exposures.

1.2.4 CTP Preprocessing

After image acquisition and tomographic reconstruction, additional preprocessing is required before tracer kinetic analysis can be applied. The acquired volumes need to be aligned in order to correct for head movement, and noise needs to be reduced to obtain perfusion parameters with sufficient precision. Besides the relatively high noise levels as compared to conventional CT scans due to low mAs, the limited contrast material dose and bolus dispersion result in low signal-to-noise ratios.

Severe head movement during X-ray exposure causes artifacts in tomographic reconstruction. Volumes containing such artifacts should be discarded in analysis. Motion in between exposures can be corrected by aligning the volumes. Although moderate to severe head movement occurs in a quarter of the CTP scans in stroke,[39] the brain is unlike most other organs not, or to a lesser extent, affected by non-rigid deformation due to breathing, swallowing and cardiac pulsation. This means that rigid registration is sufficient for proper alignment. The application of 3D rigid registration to thin-slice reconstructed CTP data effectively removes all motion.

Noise reduction is typically performed by application of an isotropic Gaussian filter or an edge-preserving filter to the individual volumes. The latter enables averaging larger regions (in the order of 1 cm³ in CTP) while minimizing *partial volume effects*, i.e. crosstalk between different structures. By using the information in the temporal domain of the CTP series, more effective edge-preserving filters, such as *TIPS*, have been developed recently.[91] Such filters not only compare voxel values, but entire TACs in order to determine the local shape of the filter kernel.

1.3 CT PERFUSION ANALYSIS IN STROKE

1.3.1 Physiology of Brain Tissue Perfusion

Besides the arterial and venous enhancement curves, every tissue voxel is also represented by an enhancement curve, describing mostly the inflow and outflow of contrast material in the capillaries, as described later on in more detail. Since the shape of these tissue TACs is affected by the perfusion properties of the tissue such as the blood volume, analysis of these

curves can provide estimates for these perfusion parameters. Three perfusion parameters that are of importance to stroke imaging are *cerebral blood volume* (CBV), *cerebral blood flow* (CBF) and *mean transit time* (MTT).

CBV is the space occupied by the intravascular blood per unit of brain tissue. Since gray matter has a high metabolic rate due to the vast number of synaptic connections, it has more dense capillary beds and therefore higher CBV than white matter (Fig. 1.10). For the healthy human brain CBVs have been reported between approximately 1.5 to 3 ml/100g for white matter and 3 to 5.5 ml/100g for gray matter.[58,59,86] These volumes only include the smallest of vessels, i.e. arterioles, capillaries, and venules. CBV can be estimated by measuring the scaling factor between the enhancement curve of a voxel with 100% blood volume, i.e. a large artery or vein, and the enhancement curve of the tissue.
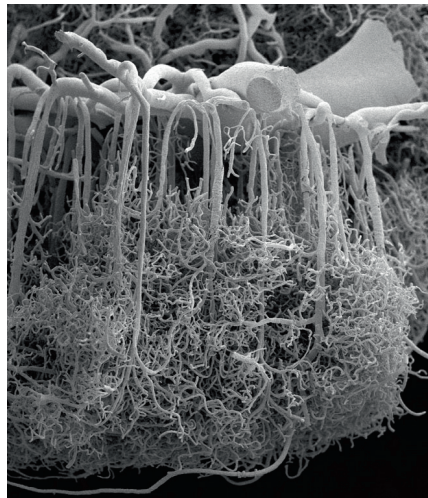
Fig. 1.10: Cortical blood vessels. Scanning electron microscope image of the blood vessels in the human cerebral cortex. This sample shows an artery within the subarachnoid cavity at the surface of the brain (top), which sends down thin, densely branched arterioles to deliver blood throughout the entire cortex. The thickness of the human cerebral cortex, and thus of the imaged capillary beds is approximately 2.5 mm. Reprint from Rodríguez-Baeza et al., as published in Schoonover, Portraits of the Mind, 2010.

CBF is the total volume of blood that flows through a unit of brain tissue per unit of time, and varies between approximately 20 to 30 ml/100g/min for white matter and 40 to 80 ml/100g/min for gray matter.[58,59,151,153] The CBF value scales with the CBV as well as the average blood velocity in the tissue.

The total cross-sectional area available for blood flow increases with decreasing vessel size. Therefore, the pressure and velocity of the blood decrease as it enters the capillaries

(Fig. 1.11). Since the capillary bed provides many different routes, the time for a molecule of contrast material to flow through the capillary bed may vary. MTT is the average time it takes for the contrast material to flow through the smallest vessels and capillary bed. This time varies between approximately 3.5 to 5 s for healthy white matter and 3 to 4 s for healthy gray matter.[58] MTT is, as in whole organ perfusion, interrelated to CBV and CBF according to the *central volume principle*, i.e. MTT = CBV/CBF.[134]

Fig. 1.11: Total cross-sectional area and blood velocity of different vessels. Since the total cross-sectional area increases with decreasing vessel size, the pressure and velocity decrease when blood enters the capillaries. Reprint from Marieb, Human Anatomy and Physiology, 2010.
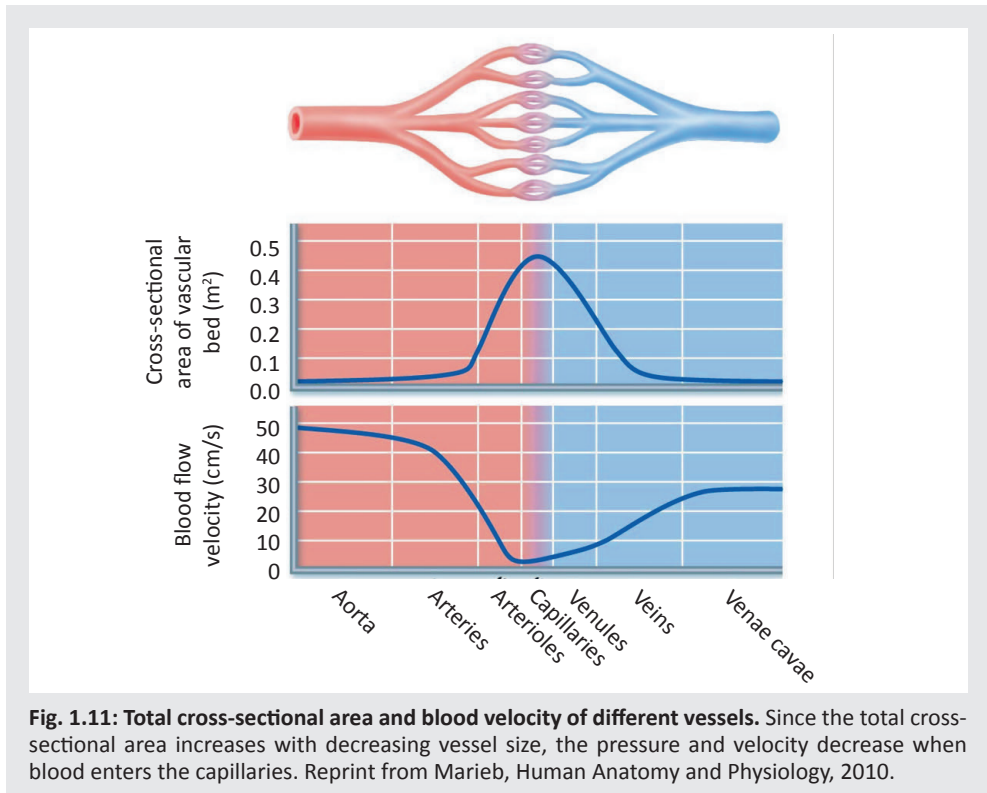
Because CBF and MTT measurement can be rather sensitive to noise, CTP assessment usually includes a fourth parameter map, visualizing the delay between the arterial and tissue *time-to-peak* (TTP). Since TTP depends on MTT, delay in bolus arrival, as well as on bolus shape, it cannot be considered a true property of the tissue. Nevertheless, this parameter is of great value to the observer in the detection of small lesions.

In vessels smaller than approximately 500 μm in diameter, the blood viscosity decreases with vessel diameter. This behavior is known as the Fåhræus-Lindqvist effect and is caused by the formation of a red blood cell free layer near the vessel wall.[41] Due to the difference in velocity between these layers, the volume fraction of red blood cells (the hematocrit)

in small vessels differs from the volume fraction in large vessels; since the velocity of the red blood cells is higher than the velocity of the plasma layer near the vessel wall, the hematocrit in small vessels is approximately 0.25, whereas the hematocrit in large vessels is approximately 0.45 in healthy people.[116] Because the plasma fraction carries the contrast material, the difference in hematocrit biases the observed CBV. In order to correct for this difference, CBV (ml/100g) is calculated as:

$$CBV = \frac{100}{\rho} \frac{\left(1 - Ht_{large}\right)}{\left(1 - Ht_{small}\right)} V_i \qquad \text{Eq. 1.1}$$

In this equation, $\rho = 1.05$ g/ml, which is the average density of brain tissue. $(1 - Ht_{large}) = 0.55$ is the volume fraction of the blood plasma in large vessels and $(1 - Ht_{small}) = 0.75$ is the volume fraction of the blood plasma in small vessels. The unitless value V_i is the observed intravascular blood volume fraction of the tissue, i.e. the scaling factor between the enhancement curve of a large vessels and the enhancement curve of the tissue. The same correction applies to CBF. However, for the sake of readability and simplicity, this correction factor will not be included in the equations in Section 1.3.3 and in the equations in the next chapters, i.e. equations will be presented as if CBV = V_i.

1.3.2 Pathophysiology in Ischemic Stroke

Due to the blockage of a blood vessel, brain tissue affected by an early ischemic stroke is characterized by reduced CBF. The brain is much more susceptible to ischemia than other organs, with brain tissue losing function if deprived of oxygen and glucose for only a few minutes. As the stroke progresses, the central region of lowest CBF (less than 20 to 25 ml/min/100g) will suffer irreversible damage leading to cell death.[96] This *infarct core* then shows reduced CBV. The rim of affected, but potentially salvageable tissue surrounding the infarct core is referred to as the ischemic *penumbra* (neo-Latin: partial shade) and demonstrates reduced CBF with normal CBV, and thus increased MTT, due to low local blood pressure. CBV might even be increased as a result of autoregulatory vasodilation. Collateral circulation from other arteries may provide additional flow in the penumbra. The function loss of brain tissue in the ischemic penumbra may still be restored by timely reperfusion.

The difference between infarct core and penumbra, also known as *target mismatch*, is a predictor for patient outcome after treatment.[79] A small infarct core correlates with reduced risk, whereas a large salvageable penumbra correlates with increased benefit. In such cases it might be beneficial to give rt-PA treatment beyond the 4.5 hour time window, or if the time of onset is unknown, as there is a more favorable risk/benefit ratio.[19]
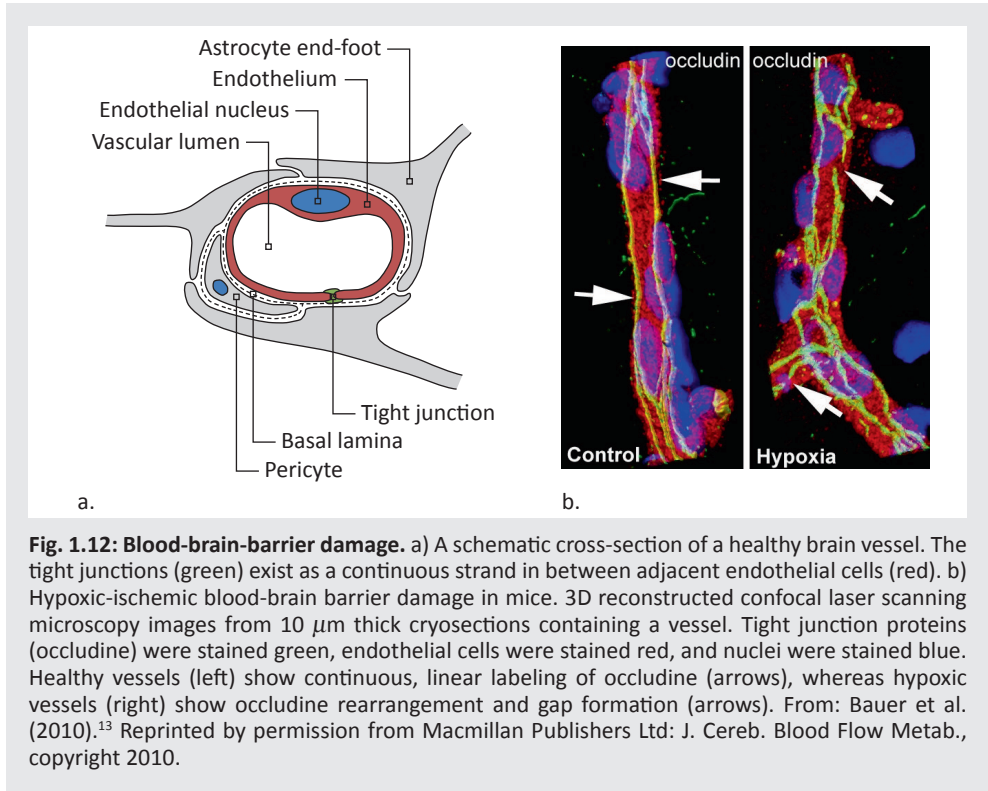
Since true quantitative measurement of perfusion values is difficult, there are currently no established threshold values for CBV, CBF, or MTT for differentiating between infarct core, penumbra and healthy tissue. Relative values for CBF and MTT, i.e. the difference between

the values observed in the ipsi-lateral (side of interest) hemisphere and in the contra-lateral hemisphere, were often found to be more reliable than absolute values. Table 1.1 gives an overview of several CT perfusion thresholds for infarct core and penumbra classification.[32]

Table 1.1: Threshold values for infarct core and penumbra classification. CT perfusion thresholds reported in 10 different studies published before August 2009. Different values for the same threshold are comma separated. rCBF, rCBV and rMTT are ratios between ipsi-lateral and contra-lateral hemisphere. From: Dani et al. (2011).[32]

Parameter	Mixed gray/white matter		Gray matter		White matter	
	Core	Penumbra	Core	Penumbra	Core	Penumbra
CBF (ml/100g/min)	-	<28	-	<25	<9.0	-
CBV (ml/100g)	<2.0	<1.7	-	-	<0.8	-
MTT (s)	>6.1	>6.5, >7.0	-	-	-	-
rCBF (%)	<34	<50, <50	<20	<48	-	-
rCBV (%)	-	<85, <90	-	<60	-	-
rMTT (%)	-	>145, >220	-	>160	-	-

Besides the loss of neurons and glial cells, ischemia in brain tissue may result in *blood-brain barrier* (BBB) damage. BBB opening, i.e. loss of microvascular integrity, has been hypothesized to be a predictor for hemorrhagic transformation (HT, development of an intracranial bleeding) in ischemic stroke.[18,49,88,96] The BBB, which is unique to the capillaries of the brain, is a highly selective permeability barrier consisting of endothelial cells that are connected by tight junctions and surrounded by an extracellular matrix (basal lamina) (Fig. 1.12a). When intact, this barrier prevents passage of large hydrophilic molecules such as CT contrast material. However, when the BBB is damaged (Fig. 1.12b) CT contrast material may penetrate the tight junctions and basal lamina and leak into the extravascular space, which could be quantified by CT perfusion imaging provided that the net outflow is sufficiently large.

Fig. 1.12: Blood-brain-barrier damage. a) A schematic cross-section of a healthy brain vessel. The tight junctions (green) exist as a continuous strand in between adjacent endothelial cells (red). b) Hypoxic-ischemic blood-brain barrier damage in mice. 3D reconstructed confocal laser scanning microscopy images from 10 μm thick cryosections containing a vessel. Tight junction proteins (occludine) were stained green, endothelial cells were stained red, and nuclei were stained blue. Healthy vessels (left) show continuous, linear labeling of occludine (arrows), whereas hypoxic vessels (right) show occludine rearrangement and gap formation (arrows). From: Bauer et al. (2010).[13] Reprinted by permission from Macmillan Publishers Ltd: J. Cereb. Blood Flow Metab., copyright 2010.

1.3.3 Mathematics of Perfusion Analysis

In order to extract perfusion parameters from CTP data, some mathematical abstraction of the perfusion process is required. The shape of the contrast bolus in the arteries and the perfusion parameters introduced in the previous sections, i.e. CBV, CBF, and MTT, as well as permeability, will somehow determine the shape of the enhancement curve as measured in the tissue.

By modelling tissue perfusion as a linear time-invariant (LTI) system, a translation from physiology to mathematics can be made. LTI theory investigates the response of linear and time-invariant dynamic systems to arbitrary input signals. In CTP, the input signal of this system is the *arterial input function* (AIF), $C_a(t)$, which is the enhancement curve observed in a large artery. The enhancement curve observed in a voxel in the tissue of interest, $C_t(t)$, is the response of the system. The system's *impulse response function* (IRF), $h(t)$, characterizes the perfusion as it allows calculating $C_t(t)$ from $C_a(t)$ by means of convolution:

$$C_t(t) = C_a(t) * h(t)$$

$$= \int_{-\infty}^{\infty} C_a(\tau) h(t-\tau) \mathrm{d}\tau$$

Eq. 1.2

1

The IRF $h(t)$ can be thought of a tissue enhancement curve in response to an infinitesimal small arterial bolus. Obtaining the $h(t)$ from the observed $C_t(t)$ and $C_a(t)$ in order to estimate values for the perfusion parameters is a so-called *inverse problem*.

Since there is no general approach to solving inverse problems, different CTP analysis methods exist. Most methods use deconvolution techniques based on either *Fourier transformation* or *singular value decomposition* (SVD) to invert the input signal $C_a(t)$. Table 1.2 gives an overview of methods used in software from different CT vendors. Deconvolution of Eq. 1.2 to obtain $h(t)$ is an *ill-posed problem*; due to measurement noise and the lack of high frequency information caused by dispersion of the arterial bolus, the solutions might be non-physical and very sensitive to small fluctuations in the noise or in the signal. This means that regularization in the form of a smoothness restriction is required in order to find a stable solution. Other methods, such as the *maximum slope method* try to directly estimate perfusion values from $C_t(t)$ and $C_a(t)$, without involving $h(t)$.[93] Those methods however require strict assumptions that do not apply in clinical practice, and thus result in biased measurements.

Table 1.2: CT brain perfusion analysis methods used in software from different CT vendors. Most methods apply deconvolution using singular value decomposition (SVD) or Fourier transformation ('inverse filter'). The 'maximum slope' and 'least mean square' methods apply direct curve fitting to the enhancement curves. The 'box-modulation transfer function' (box-MTF) convolves the AIF with a 2-parameter box-shaped IRF. From Kudo et al. (2013).[76]

Manufacturer	Software version	Algorithm
GE Healthcare	CT Perfusion 3	SVD
GE Healthcare	CT Perfusion 4	SVD
Hitachi Medical Systems	Perfusion Analysis 3.0	'Inverse filter'
Philips Healthcare	EBW 4.0	'Standard SVD'
Philips Healthcare	EBW 4.0	'Beta-SVD'
Siemens Healthcare	Syngo MMWP VE36A	'Maximum slope'
Siemens Healthcare	Syngo MMWP VE36A	'Least mean square'
Toshiba Medical Systems	CBP Study Ph8	'box-MTF'
Toshiba Medical Systems	CBP Study Ph8	'Reformulated SVD'

The method used in this thesis is rather different from common CTP analysis methods. Instead of estimating perfusion values from the deconvolved IRF $h(t)$, a mathematical model for $h(t)$ based on the perfusion parameters is assumed. The method optimizes the values for the parameters in the model for $h(t)$ such that $h(t) * C_a(t)$ matches the observed $C_t(t)$ the best. This approach is explained in more detail in Chapter 2.

The shape of $h(t)$ is best explained by transit times. As explained in Section 1.3.1, the transit time is the time it takes for the contrast material to flow through the smallest vessels and capillary bed. Since this trajectory occupies a volume smaller than a voxel, the contrast material will keep contributing to the signal enhancement of this voxel during the entire transit of this trajectory. The IRF of this single trajectory will therefore be a block-shaped function having a width equal to the duration of the transit. The IRF of the capillary network within a voxel is the sum of the IRFs of all possible trajectories. Since there is a plurality of possible routes through the network, all with distinct transit times, a realistic IRF will have a smooth decay following some distribution rather than a sharp discontinuity. This principle is explained in Fig. 1.13.

Because $C_a(t)$ is usually measured in a large artery at some distance from the tissue of interest, the IRF may be shifted to the right in order to incorporate the delay in bolus arrival. Occasionally, when a collateral artery provides $C_a(t)$, the delay may even be negative as the bolus could arrive earlier in the healthy tissue than in the collateral artery in the affected hemisphere. In that case the IRF should be shifted to the left. It was found that delay-insensitive methods provide more accurate results.[73,77,123] From the commercial methods listed in Table 1.2, only the 'least mean square' method was found to be delay-independent for all perfusion parameters.[76]

In tissue affected by ischemic stroke, the IRF will be lower and wider due to the decreased CBF. In case of leakage due to BBB opening, a fraction of the contrast material might enter and remain in the extravascular space in the tissue until it is washed out. This effectively prolongs the mean transit time and increases the apparent blood volume. When the rate of outflow to the extravascular space (K^{trans}) is small, however, the vascular CBV can be distinguished from the extravascular distribution volume, V_e. The effect of K^{trans} and V_e on $h(t)$ is shown in Fig. 1.14. In the (hypothetical) case that the leakage is irreversible, i.e. contrast material is not washed out of the extravascular space, then $V_e = \infty$ and $h(\infty) = K^{trans}$. Measurement of K^{trans} requires extended scan duration as explained in Section 1.2.3. Fig. 1.15 gives theoretical enhancement curves for tissues with IRFs as in Fig. 1.13f and Fig. 1.14, and an AIF as in Fig. 1.9.
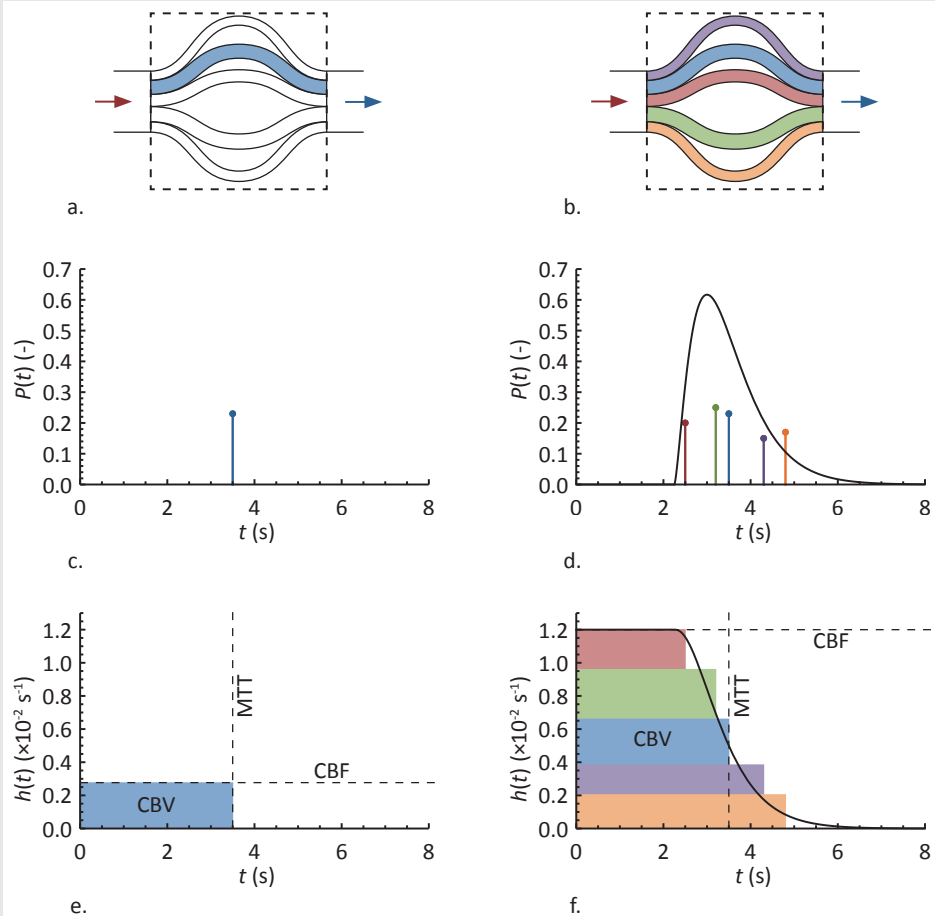
Fig. 1.13: Impulse response function (IRF) of a capillary bed. A single trajectory through a capillary bed (a), has a single transit time (c), and therefore the IRF $h(t)$ is a block-shaped function having a width equal to the duration of the transit (e). The height of this block-shape is equal to the flow, and the area is equal to the volume fraction of the trajectory. A series of trajectories (b), has a series of transit times (d), and therefore the net IRF is the sum of the IRFs of all trajectories (f). Note that the net flow is equal to the sum of the flows and the net volume fraction is equal to the sum of the volume fractions. For a large number of trajectories, as in reality, there is some continuous distribution of transit times $P(t)$ as represented by the black lines in (d) and (f).

Fig. 1.14: Example of an impulse response function with high permeability. In this example the mean transit time (MTT) is 7 s and the cerebral blood flow (CBF) is 0.003 s^{-1}. The rate of outflow to the extravascular space (K^{trans}) is 20% of the CBF; this means extensive blood-brain barrier damage. The extravascular distribution volume (V_e) is 50% of the vascular cerebral blood volume (CBV). In the (hypothetical) case that the leakage is irreversible, then $V_e = \infty$ and $h(t{\rightarrow}\infty) = K^{trans}$ (dashed curve).
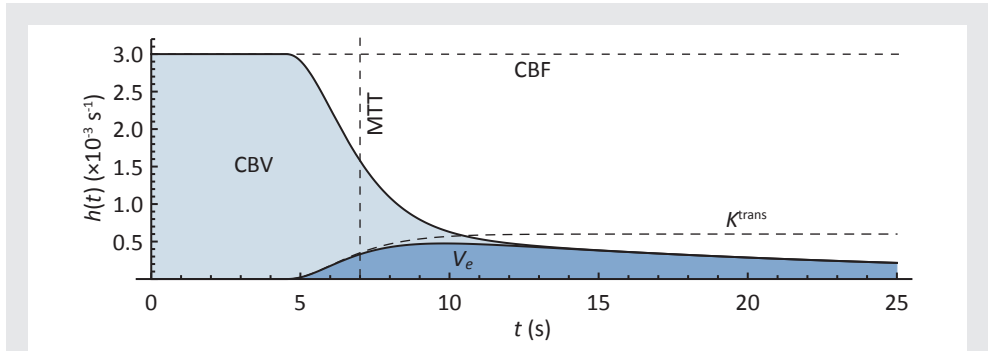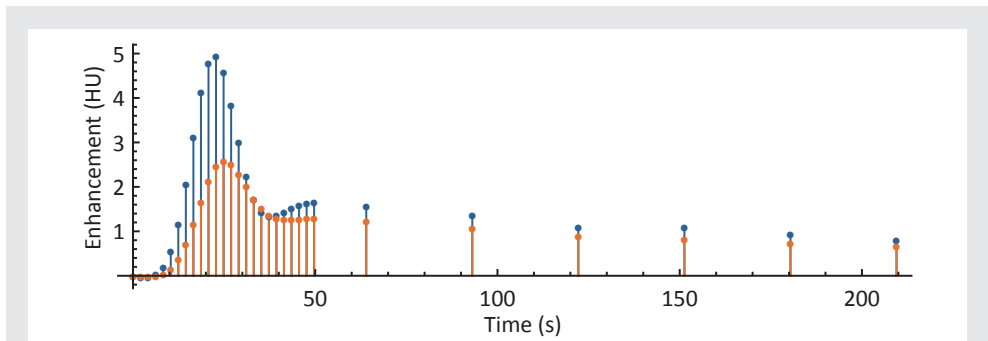

Fig. 1.15: Tissue time enhancement curves. These noise-free, theoretical tissue enhancement curves were generated by convolving the arterial input function in Fig. 1.9 with the impulse response functions (IRF) in Fig. 1.13f (blue) and in Fig. 1.14 (red). Due to the low flow and long transit time, the red curve has a lower amplitude and a larger width. Due to leakage, the amplitude of the 'tail' of the red curve is relatively high with respect to its first pass bolus peak.

1.4 CLINICAL STUDY PROTOCOL

1.4.1 Dutch Acute Stroke Study

All clinical scans that were used in this study are from the Dutch acute stroke study (DUST).[129] In brief, DUST was a large prospective multicenter cohort study, which aimed to assess the prognostic value of CTP and CTA in ischemic stroke patients for 90-day clinical outcome. The DUST study enrolled 1476 patients in 14 Dutch centers between May 2009 and August 2013. The DUST study was approved by the local institutional ethical review boards of the

participating centers, and all patients or family gave signed informed consent. In case a patient died before informed consent could be obtained, the medical ethics committee waived the need for informed consent. Inclusion criteria for DUST were: age above 18 years, suspected ischemic stroke of less than 9 hours duration and a National Institutes of Health Stroke Scale (NIHSS, a stroke severity scale)[25] score ≥2, or 1 if an indication for rt-PA therapy is present. Exclusion criteria were known renal failure or contrast allergy. On admission, all patients underwent NCCT, as well as CTP and CTA. Follow-up NCCT imaging was performed after three days or earlier in case of discharge or in case of clinical deterioration. The DUST study protocol and main findings have been published by Van Seeters et al (2014, 2015).[129,130]

1.4.2 CTP Acquisition Protocol

CTP was performed on admission before or immediately after possible rt-PA treatment. Scans were acquired on 40 to 320-slice scanners (Philips, Siemens, GE, Toshiba), generally at 80 kVp and 150 mAs. The scans had a total acquisition time of about 210 seconds, divided into a first part of 25 acquisitions with an approximately 2 second interval starting at contrast injection, followed by another 6 acquisitions with an approximately 30 second interval starting at 60 seconds after contrast injection. The second part of 6 acquisitions was required for permeability measurements (used in the studies described in Chapters 3, 4, and 5). Before scanning, 40 ml of non-ionic contrast agent was injected intravenously at a rate of 6 ml/s, followed by a 40 ml saline flush.

Axial CTP coverage ranges from 40 mm to full-brain, covering at least the basal ganglia and the upper part of the lateral ventricles, thus ensuring inclusion of both levels of the Alberta Stroke Program Early CT Score (ASPECTS).[10] The scan volume was lowered if a posterior circulation stroke was suspected. The slices had a field-of-view of approximately 200 mm × 200 mm. The scans were reconstructed in a 512 × 512 matrix using filtered backprojection with a medium smooth reconstruction kernel (vendor-specific), yielding a pixel size of approximately 0.4 mm × 0.4 mm. All CTP scans were reconstructed to a slice thickness of 5 mm, but in addition a large number of thin slice reconstructions (0.625 to 1.25 mm) were also computed.

1.5 OUTLINE OF THE THESIS

This thesis is concerned with the development of quantitative analysis methods that could increase the effectiveness of functional CT imaging in selecting patients for rt-PA treatment. Model-based perfusion analysis with non-linear regression provides the core of the research.

Chapter 2 introduces a simple, but flexible and robust model-based analysis method allowing measurement of cerebral blood volume, cerebral blood flow, and mean transit

time. This method is compared with the current state-of-the-art method and a commercial method by means of a digital perfusion phantom and with the aid of 50 clinical CT perfusion scans.

Chapter 3 extends this method with permeability measurement. Vascular permeability could be a predictor of hemorrhagic transformation (HT) after rt-PA treatment. The reliability of the permeability parameters are evaluated in comparison with frequently used Patlak analysis. Confidence intervals are estimated using simulated time-attenuation curves and clinical data from 20 patients.

In **Chapter 4**, the predictive power for HT development is compared between different perfusion and permeability parameters. Receiver-operating characteristic analyses are performed on the admission CT scans of 20 patients with HT on follow-up CT, and 40 patients without HT.

Chapter 5 assesses the influence of reconstruction slice thickness on the CT perfusion and permeability measurements. Thin slices may increase sensitivity for stroke detection. The CT perfusion scans from 50 patient studies are analyzed at four slice thicknesses. Specifically, the influence of Gaussian and bilateral filtering, the arterial input function, and motion correction on the perfusion values is investigated.

The study in **Chapter 6** compares the performance for small lesion (<20 mm) detection between standard thick slice and thin slice reconstruction. The CTP parameter maps of 41 cases and 82 controls are randomized and evaluated for the presence of a small focal deficit. Performance is compared using McNemar's test.

Chapter 7 summarizes the previous chapters, and gives an overall discussion and future outlook.

1.6 LIST OF ABBREVIATIONS

Abbreviation	Full phrase
AAPM	American Association of Physicists in Medicine
AATH	Adiabatic approximation to the TH model
AIF	Arterial input function
ASPECTS	Alberta Stroke Program Early CT Score
AUC	Area under the curve
BAT	Bolus arrival time
BBB	Blood-brain barrier
CBF	Cerebral blood flow
CBV	Cerebral blood volume
CI	Confidence interval
CT	Computed tomography
CTA	CT angiography
CTP	CT perfusion
DCE	Dynamic contrast enhancement
DUST	Dutch stroke study
DWI	MR Diffusion weighted imaging
FWHM	Full width at half maximum
HT	Hemorrhagic transformation
HU	Hounsfield units
IAT	Intra-arterial thrombolysis
IQR	Interquartile range
IRF	Impulse response function
IVT	Intra-venous thrombolysis
MR	Magnetic resonance
MT	Mechanical thrombectomy
MTT	Mean transit time
NCCT	Non-contrast CT
NIHSS	National Institutes of Health Stroke Scale
NLR	Non-linear regression
PET	Positron emission tomography
PS	Permeability-surface area product
PVE	Partial volume effect
ROC	Receiver operating characteristic
ROI	Region of interest
SD	Standard deviation
SNR	Signal-to-noise ratio
SPECT	Single photon emission computed tomography
SVD	Singular value decomposition
rt-PA	Recombinant tissue plasminogen activator
TAC	Time-attenuation curve
TH	Tissue homogeneity model
TIPS	Time-intensity profile similarity
TTP	Time-to-peak
VOF	Venous output function

2

Model-based Perfusion Analysis

ABSTRACT

Although CT perfusion (CTP) imaging enables rapid diagnosis and prognosis of ischemic stroke, current CTP analysis methods have several shortcomings. We propose a fast non-linear regression (NLR) method that has important advantages over the current state-of-the-art method, block-circulant singular value decomposition (bSVD), notably improved robustness to local tracer delay, fewer tuning parameters, and extensibility to permeability estimation.

The method is compared with bSVD and with a commercial SVD-based method. The three methods were quantitatively evaluated by means of a digital perfusion phantom, described by Kudo et al. (2013),[76] and qualitatively with the aid of 50 clinical CT perfusion scans.

All three methods yielded high Pearson correlation coefficients (>0.9) with the ground truth in the phantom. The NLR perfusion maps of the clinical scans showed higher correlation with bSVD than the perfusion maps from the commercial method. Furthermore, it was shown that NLR estimates are robust to noise, truncation and tracer delay.

In conclusion, the proposed fast NLR method provides a simple, robust, and flexible way of estimating perfusion parameters from CTP scans. This suggests it could be a viable alternative to current commercial and academic methods.

2.1 INTRODUCTION

CT perfusion (CTP) imaging of the brain enables rapid diagnosis of ischemic stroke by generating maps of the cerebral blood volume (CBV), cerebral blood flow (CBF), and mean transit time (MTT). Low CBV is an indicator for infarction, whereas tissue at risk shows low CBF but normal CBV. The tissue at risk, or penumbra, may be saved by prompt and correct diagnosis and treatment.

Brain perfusion parameters are commonly derived from a so-called impulse response function (IRF) of the local tissue. The analysis to retrieve this IRF usually involves deconvolution algorithms. Block-circulant singular value decomposition (bSVD) is considered the state-of-the-art deconvolution method because it has been shown to give the most accurate and delay-insensitive estimates.[77] The latter property is important in regions that experience a delayed arrival of the tracer bolus, as is often the case in tissue supplied by collateral flow. It was found that tracer delay-sensitive methods underestimate the CBF and therefore overestimate the final infarct area, whereas the values from delay-insensitive methods correspond well with the infarct area.[78] However, bSVD use is limited to measuring CBV, CBF, and MTT, whereas permeability measurements might be of interest for predicting hemorrhagic transformation (see Chapters 3 and 4). bSVD furthermore requires various algorithm parameter settings, such as the method and strength of noise reduction, or the way in which CBV and MTT are calculated.

We propose the use of a flexible, model-based, non-linear regression (NLR) method that has some advantages over deconvolution methods and is aimed at having better performance than bSVD. The method provides a unified way of estimating CBF, CBV, and MTT, and it can be extended to account of vascular permeability, which is detailed in the next chapter. Because extrapolation of data requires a model, it is furthermore hypothesized that the model-based NLR method will be more robust to time-attenuation curve (TAC) truncation. Truncation is a common issue in CTP scans of patients with poor cardiac output or large vessel occlusion, in which case the acquisition times are too short to capture complete TACs.[22,72]

The performance of the NLR method will be evaluated against bSVD and against the delay-insensitive deconvolution method found in the Philips EBW 4.5 Brain Perfusion package (Philips Healthcare, Best, the Netherlands). This will be done quantitatively, on the basis of the digital perfusion phantom developed by Kudo et al. (2013),[76] and qualitatively on the basis of 50 clinical CT brain perfusion scans.

2.2 METHODS

2.2.1 Digital Perfusion Phantom

In order to compare the performance of the three methods in quantifying CT brain perfusion, the digital perfusion phantom of Kudo et al. was analyzed. In their publication the phantom was described in detail.[76] It was used for assessment of bSVD and various other methods for CT and MR perfusion analysis. The phantom consists of 15 slices with 7 × 7 matrices of tiles with synthetic TACs with uncorrelated Gaussian noise. There are 30 samples per TAC with an interval of 2 seconds. The standard deviation of the noise is 7.2 HU, which is realistic for e.g. 5 mm thick slices acquired at 80 kVp and 150 mAs. The arterial input function (AIF) and venous output function (VOF) were modelled as gamma-variate curves. Recirculation was not taken into account.

Each tile represents a patch of uniform tissue, and consists of voxels with identical perfusion parameters and equal Gaussian noise level, but different noise realizations. Horizontally in the tiles the MTT was varied (24, 12, 8.0, 6.0, 4.8, 4.0, and 3.4 s), while vertically the tracer delay was varied (0.0 to 3.0 s in steps of 0.5 s). The 15 slices of the phantom have 5 different CBV values (1.0 to 5.0 ml/100g) and three types of IRFs (exponential, linear, and box-shaped). The CBF can be determined through the central volume principle: MTT = CBV/CBF.

Prior to analysis, the slices in the phantom were filtered with a 2D Gaussian kernel with a standard deviation of 2.5 pixels. No additional filtering was applied.

2.2.2 Non-linear Regression Method

As explained in Section 1.3.3 of the first chapter, tissue perfusion can be modeled by means of an impulse response function (IRF) $h(t)$. Convolution of the measured AIF, $C_a(t)$, with a computed estimate of $h(t)$, gives an estimate of the enhancement curve of the tissue, $C_t(t)$:

$$C_t(t) = C_a(t) * h(t) + \varepsilon(t)$$

Eq. 2.1

The residual term $\varepsilon(t)$ is the difference between the estimated and measured TACs, caused both by measurement noise in $C_t(t)$ and $C_a(t)$ and by shortcomings of the model.

Non-linear regression is used to iteratively adapt the parameters in $h(t)$, i.e. CBV, MTT, and tracer delay, to minimize the sum of squares of $\varepsilon(t)$. Weights might be used in the regression to incorporate additional constraints or prior knowledge. A relatively simple box-shaped IRF enables fast NLR analysis which is advantageous in time-critical stroke analysis (see Fig. 3.11 in the next chapter for computation times):

$$h_{\text{box}}(t) = \text{CBF}\big(\text{U}(t - t_d) - \text{U}(t - t_d - \text{MTT})\big)$$ Eq. 2.2

In Eq. 2.2, U(t) is the unit step function and t_d is the delay in bolus arrival between the AIF and the tissue curve. A similar model, the so called box-modulation transfer function (box-MTF), was introduced by Nambu et al. (1996)[101]. This model, however, did not include a delay parameter and was thus found to be tracer delay-sensitive. Accordingly, it was outperformed by the bSVD method[76].

The convolution in Eq. 2.1 , with the IRF $h_{\text{box}}(t)$ as given in Eq. 2.2, can also be defined in terms of differential equations, i.e. as the solution of:

$$\frac{\text{d}C_t(t)}{\text{d}t} = \text{CBF}\big(C_a(t - t_d) - C_a(t - t_d - \text{MTT})\big) + \frac{\text{d}\varepsilon(t)}{\text{d}t}$$ Eq. 2.3

When Eq. 2.3 is integrated, the convolution can be calculated efficiently by sampling the integral of the arterial enhancement curve:

$$C_t(t) = \text{CBF}\left(\int_0^{t-t_d} C_a(\tau)\text{d}\tau - \int_0^{t-t_d-\text{MTT}} C_a(\tau)\text{d}\tau \right) + \varepsilon(t)$$ Eq. 2.4

To prevent aliasing artifacts owing to sampling, frequency components in the IRF above the Nyquist frequency should be suppressed. A Bartlett kernel (triangular) with a width of twice the sample interval was therefore used to sample the integral of $C_a(t)$ and to filter $C_t(t)$. Section 3.2.4 of the next chapter explains this in more detail.

The shape of the IRF is the only choice to be made for application of this NLR method in CTP analysis.

2.2.3 bSVD Deconvolution

The convolution in Eq. 2.1 can be written as the matrix operation **b** = **Ax** + **ε**, where vector **b** is $C_t(t)$, **A** is a matrix with zero-padded, circularly shifted versions of the AIF $C_a(t)$ at regular intervals of t, vector **x** is the IRF, and vector **ε** is a residual term. The least-squares solution of the IRF **x** can be found by inverting **A**. The bSVD method uses singular value decomposition (SVD) to find a pseudo-inverse of **A**, which for circulant matrices is mathematically equivalent to applying a Fourier transform.

In order to suppress noise in the resulting IRF, the least significant eigenvectors are consecutively removed until **x** has an oscillation index below a certain threshold.[45] In this study a threshold of 0.095 is used, as suggested by Wu et al. (2003).[152] The CBF is defined as the maximum value in the vector **x**. The CBV is estimated by calculating the ratio between the integrals of $C_t(t)$ and $C_a(t)$.

The commercial method (Philips) is also SVD-based, but no detailed technical information about this algorithm is available. The code for the both the NLR method and the bSVD method was developed in-house; the bSVD method was implemented following the description of Wu et al. (2003).[152]

2.2.4 Clinical Data

Fifty consecutive patients were included retrospectively from a single center (University Medical Center Utrecht) participating in the Dutch acute stroke study (DUST). The inclusion criteria and the CTP acquisition protocol are described in Section 1.4.

All scans included in this study were acquired on a 256-slice Philips Brilliance iCT scanner (Philips Healthcare, Best, the Netherlands) at 80 kVp and 150 mAs. The scans had a total acquisition time of about 50 seconds, divided into 25 acquisitions with an approximately 2 second interval. Since standard perfusion analysis does not require extended acquisition, the second (extended) part of the CTP scans was not used (see Section 1.4.2). This resulted in an effective radiation dose of 2.7 mSv. The axial coverage was 60 to 65 mm and the field-of-view was approximately 200 mm × 200 mm. The scans were reconstructed to a slice thickness of 5 mm, and the pixel size was 0.39 mm × 0.39 mm.

2.2.5 Preprocessing

Prior to analysis the scans were corrected for motion using a rigid registration method[67] and filtered using a bilateral filter.[137] This filter computes a bilateral weight based on the Euclidean distance between two voxels and the squared difference in average intensity between the TACs of those voxels. The values of the 3D bilateral kernel $b(\boldsymbol{\xi},\mathbf{x})$ at coordinate $\boldsymbol{\xi}$ is defined by

$$g(\boldsymbol{\xi},\mathbf{x}) = \exp\left(-\tfrac{1}{2}\left(\frac{\|\boldsymbol{\xi}-\mathbf{x}\|}{\sigma_d}\right)^2\right)$$

$$b(\boldsymbol{\xi},\mathbf{x}) = g(\boldsymbol{\xi},\mathbf{x})\exp\left(-\tfrac{1}{2}\left(\frac{\left(\overline{I}(\boldsymbol{\xi})-\overline{I}(\mathbf{x})\right)^2}{\sigma_r}\right)^2\right) , \qquad \text{Eq. 2.5}$$

where $\mathbf{x}$ is the coordinate of the center voxel, σ_d is the spatial standard deviation (SD) of the kernel, and σ_r is the similarity SD. $\overline{I}(\boldsymbol{\xi})$ and $\overline{I}(\mathbf{x})$ are the mean CT values at coordinates $\boldsymbol{\xi}$ and $\mathbf{x}$ (averaged over time). The bilateral filter thus weighs both by spatial distance as well as by the squared error on the mean intensity.

The spatial SD of this filter was σ_d = 3 mm, and the intensity SD was σ_r = 20 HU^2. These settings resulted in similar noise levels as in the filtered phantom.
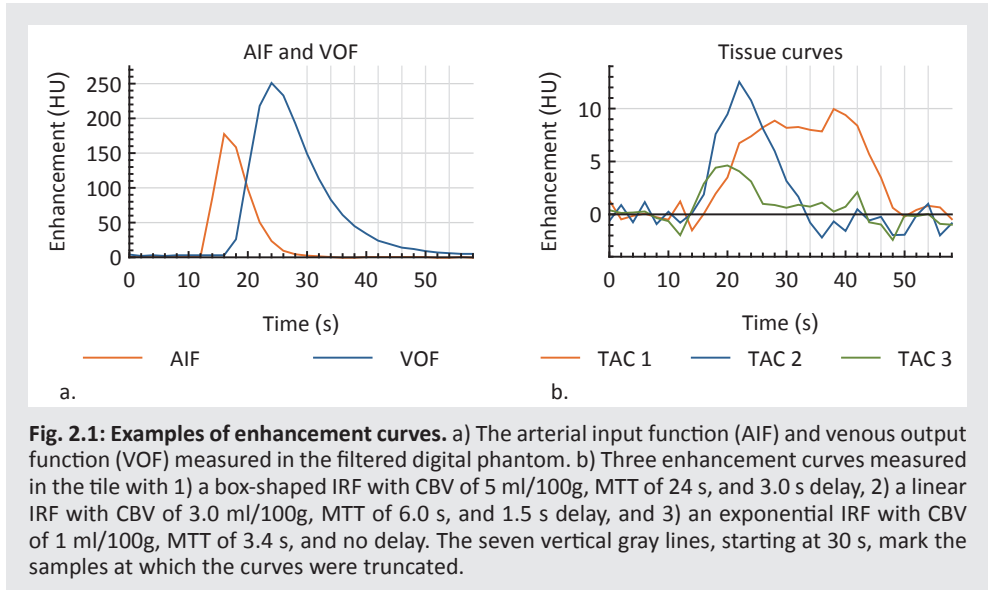
2.2.6 Analysis

Whenever possible an internal carotid artery was chosen to provide the AIF. If this location happened to be outside the imaged volume, a middle or anterior cerebral artery was chosen. VOFs were selected in the superior sagittal sinus or the transverse sinus near the torcular herophili. The same AIF and VOF locations were used for all three methods.

All three analysis methods generated CBV, MTT, and CBF perfusion maps for the digital phantom and for the clinical data. It should be noted that, although three parameters were measured, these perfusion parameters just capture two degrees of freedom because of their interrelation (central volume principle): MTT = CBV/CBF. The area under the curve of the VOF was used to correct the CBV and CBF values for partial volume effects in the AIF. CBV and CBF values were furthermore corrected for the difference in hematocrit between large and small vessels (see Eq. 1.1 in Section 1.3.1).[71]

Similarly to the approach by Kudo et al. (2013), the average perfusion value in each tile was calculated by averaging all pixels in a 28 × 28 pixel region centered on each 32 × 32 pixel large tile.[76] In order to compare the observed values with the ground truth, linear fits through the origin and Pearson correlation coefficients (ρ) were calculated for the three IRF types separately, and for the IRF types combined. Good correlation was defined as $\rho > 0.9$.

To assess the effect of noise on the perfusion values, the phantom data were filtered with eight 2D Gaussian filter kernels with decreasing radius. This resulted in 8 increasing noise levels, ranging from 0.84 HU (SD) at a kernel size of 2.5 pixels (SD) to 2.3 HU at a kernel size of 0.93 pixels. At each noise level Pearson coefficients of correlation with the ground truth were calculated, as well as the median and the interquartile range of the bias in average tile value as compared with the lowest noise level. Pearson coefficients were calculated per IRF and then averaged.

The effect of truncation of the attenuation curves was assessed by truncating the phantom data from 58 to 30 s in steps of 4 s, i.e. by 2 samples (vertical lines in Fig. 2.1a and b). In each step, Pearson coefficients of correlation with the ground truth were calculated, as well as the median and interquartile range of the bias in average tile value as compared with data of 58 s duration. Again Pearson coefficients were calculated per IRF and then averaged.

Fig. 2.1: Examples of enhancement curves. a) The arterial input function (AIF) and venous output function (VOF) measured in the filtered digital phantom. b) Three enhancement curves measured in the tile with 1) a box-shaped IRF with CBV of 5 ml/100g, MTT of 24 s, and 3.0 s delay, 2) a linear IRF with CBV of 3.0 ml/100g, MTT of 6.0 s, and 1.5 s delay, and 3) an exponential IRF with CBV of 1 ml/100g, MTT of 3.4 s, and no delay. The seven vertical gray lines, starting at 30 s, mark the samples at which the curves were truncated.

For the analysis of the clinical data, bSVD was considered the reference method. The perfusion maps of the commercial method and of the NLR method were each compared with that obtained by using bSVD. Linear fits through the origin and Pearson correlation coefficients were calculated per patient, using all parenchymal voxels. Mean CBF, CBV, and MTT values were calculated in the brain tissue in both the ipsilateral and the contralateral hemisphere. Symmetry lines were drawn manually to separate the hemispheres.

The acquisitions before bolus arrival, which is estimated by curve-fitting of the AIF, were averaged to obtain a non-contrast CT image. Only the voxels that had an average CT value >17 HU and <55 HU were classified as parenchymal tissue and included in the analysis. Voxels with a blood volume >9 ml/100g were classified as vessels and excluded from the analysis.

2.3 RESULTS

2.3.1 Phantom Data
Fig. 2.2 shows an example of the ground truth and estimated perfusion maps of one of 2D slices in the phantom. Although all three methods were supposed to be delay-insensitive, the perfusion maps of the commercial method and bSVD both showed diagonal bands in the CBF and MTT maps. Also, the response to high CBF and low MTT values seemed to be reduced for both methods. The commercial method furthermore showed overestimated CBV values.

Fig. 2.2: Example of digital phantom perfusion maps. Ground truth maps and measured perfusion maps of the last slice of the digital phantom, i.e. a box-shaped IRF and CBV of 5 ml/100g. The phantom was filtered using a 2D Gaussian kernel with an SD of 2.5 pixels. All tiles in this slice have the same box-shaped IRF and a CBV of 5 ml/100g, while the MTT was varied horizontally (24 to 3.4 s, from left to right), and the tracer delay was varied vertically (0 to 3 s, from top to bottom). The CBF can be determined by the central volume principle: CBV = CBF × MTT.

The slopes and correlation coefficients of the average measurements with respect to the ground truth are given in Table 2.1. All methods showed good correlation with the ground truth for each of the three IRF shapes ($\rho > 0.90$). For the three IRF types combined, however, the Pearson coefficients for CBF measured with the commercial method and NLR were smaller than 0.9. The R^2 values and the correlation coefficients were highest for CBV and were comparable amongst the three methods. The bSVD and NLR methods showed higher R^2 values and correlation coefficients for CBF and MTT than the commercial method.

Table 2.1: Responses to digital phantom. Slope and goodness of fit (R^2) and Pearson correlation coefficient (ρ) for the relation between the observed perfusion values and the ground truth values of the phantom. The slopes and R^2 values were calculated for a linear fit through the origin. The values were measured for each IRF shape separately (exponential, linear, and box-shaped) as well as for the three shapes combined ('All'). The best fits and highest correlation coefficients are bold-faced.

		Slope (R^2)			Pearson ρ		
		Commercial method	**bSVD**	**NLR**	**Commercial method**	**bSVD**	**NLR**
	CBF	0.55 (0.84)	0.58 (0.93)	**0.47 (0.96)**	0.96	0.97	**0.98**
Exponential	**CBV**	1.12 (0.96)	**0.95 (0.96)**	0.86 (0.95)	0.98	**0.98**	0.97
	MTT	1.13 (-0.18)	1.02 (0.32)	**1.25 (0.59)**	**0.96**	0.96	0.93
	CBF	0.66 (0.83)	0.71 (0.95)	**0.68 (0.98)**	0.95	0.98	**0.99**
Linear	**CBV**	1.18 (0.98)	**0.98 (0.99)**	0.96 (0.99)	0.99	**1.00**	0.99
	MTT	1.09 (0.59)	0.99 (0.85)	**1.22 (0.90)**	0.98	**0.98**	0.97
	CBF	0.76 (0.69)	0.83 (0.85)	**1.12 (0.98)**	0.90	0.94	**0.99**
Box-shaped	**CBV**	1.20 (0.98)	0.99 (0.99)	**1.00 (1.00)**	0.99	1.00	**1.00**
	MTT	0.91 (0.51)	0.83 (0.85)	**0.96 (0.99)**	0.97	0.98	**0.99**
	CBF	0.65 (0.72)	**0.71 (0.85)**	0.76 (0.71)	0.89	**0.93**	0.84
All	**CBV**	1.17 (0.97)	**0.97 (0.98)**	0.94 (0.96)	0.98	**0.99**	0.98
	MTT	1.04 (0.34)	0.95 (0.68)	**1.14 (0.81)**	0.93	**0.94**	0.92

2.3.2 Response to Noise

Fig. 2.3 shows an example of the ground truth and estimated perfusion maps of one of 2D slices in the phantom, filtered with a smaller 2D Gaussian kernel (SD 0.93 pixels, vs. 2.5 pixels for Fig. 2.2). This resulted in perfusion maps with higher noise level than those in Fig. 2.2. The visual differences between maps of the same method in Fig. 2.2 and Fig. 2.3 were small. The CBV and MTT maps showed a rather uniform noise level throughout each slice, but the noise level of the CBF seemed to increase with the CBF value (top right map in Fig. 2.3).

As concerns correlation with the ground truth, all methods showed a similar trend in response to noise (Fig. 2.4). Only the MTT values showed a linear decrease in correlation as a function of the noise level, in roughly the same fashion for each of the methods (Fig. 2.4c).

The bias with respect to the low-noise maps as a function of noise level (Fig. 2.5) differed substantially between the three methods. Median CBF measured with the commercial method and with NLR increased with the noise level, but decreased when measured with bSVD. Median CBV values measured with bSVD and NLR were not strongly influenced by noise, but CBV values measured with the commercial method increased with noise level. Median MTT measured with NLR showed no bias due to noise, but increased with noise when measured with the commercial method and with bSVD.

2
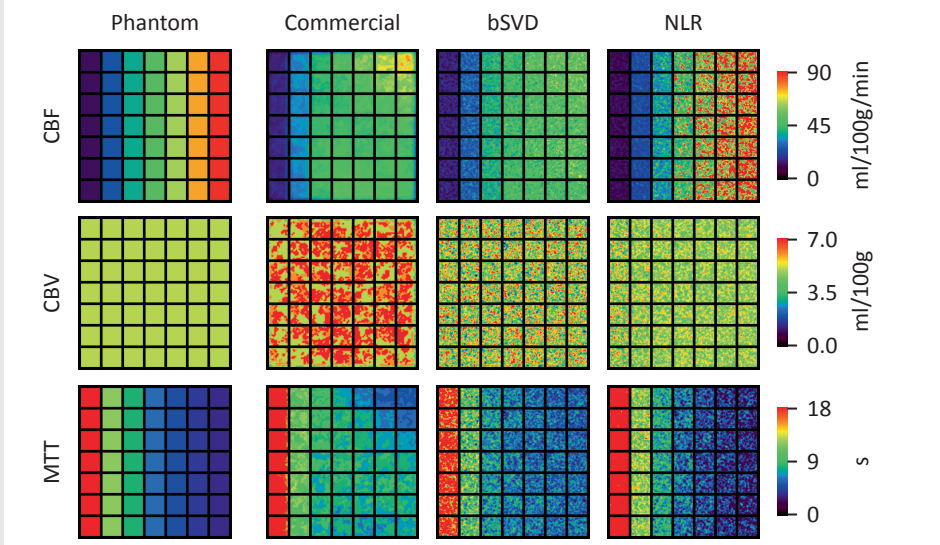
Fig. 2.3: Example of digital phantom maps with increased noise. Ground truth maps and measured perfusion maps in the same phantom slice as shown in Fig. 2.2. In this case, however, the phantom was filtered using a 2D Gaussian filter with an SD of just 0.93 pixels, resulting in a higher noise level (noise SD=2.3 HU).
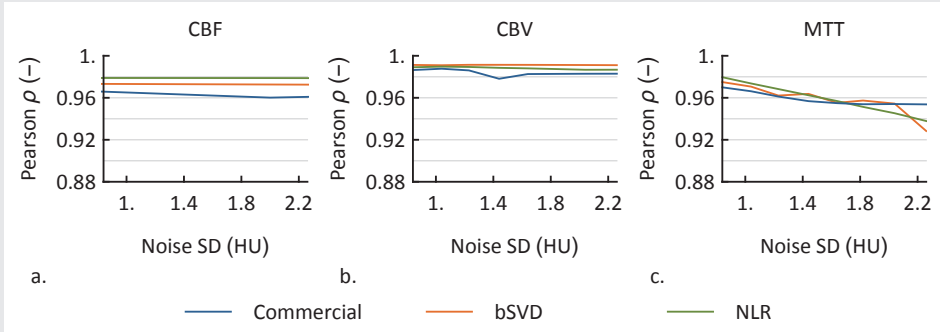
Fig. 2.4: Correlation with ground truth as a function of noise level. a) Cerebral blood flow, b) cerebral blood volume, and c) mean transit time. The figures show the Pearson coefficients of the correlation of the estimated perfusion values with the ground truth in the phantom, as a function of the noise level.

Fig. 2.5: Bias of the perfusion analysis methods due to noise. a) Cerebral blood flow, b) cerebral blood volume, and c) mean transit time. The figures show the median and interquartile ranges of the bias of the estimated perfusion values to low-noise estimates, as a function of noise level.
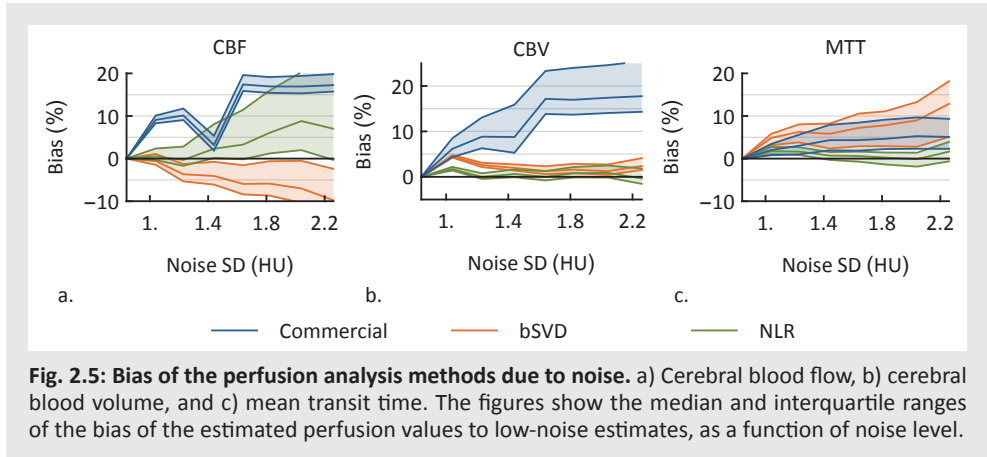
2.3.3 Response to Truncation

The commercial and bSVD methods gave visually similar responses to truncation of attenuation curves, as is illustrated in Fig. 2.6. The NLR method showed the smallest differences with the analysis on the full curves (Fig. 2.2). The estimates in the first row (MTT = 24 s) were the most affected by truncation, resulting in underestimated CBV values for the commercial and bSVD methods, and increased noise in CBV values for the NLR method.
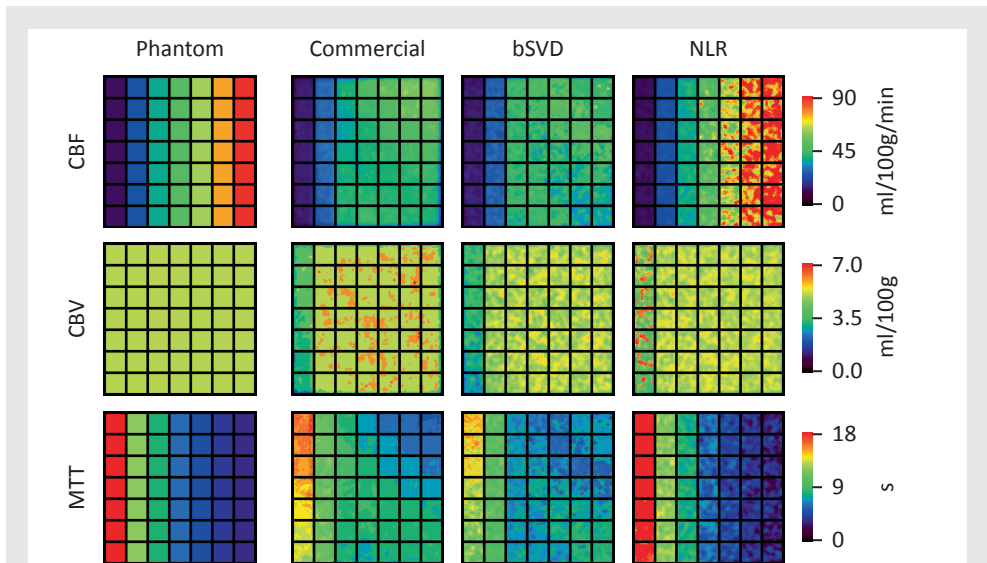

Fig. 2.6: Example of digital perfusion phantom maps with truncated attenuation curves. Ground truth maps and measured perfusion maps in the same phantom slice as shown in Fig. 2.2. In this case, however, just 18 out of 30 samples (34 s) were analyzed, resulting in truncated attenuation curves (Fig. 2.1b). The phantom was filtered using a 2D Gaussian filter with an SD of 2.5 pixels.

The NLR method correlated better with the ground truth than the commercial method and bSVD (Fig. 2.7), especially when large numbers of samples were removed. The Pearson coefficients of the commercial method and bSVD showed similar trends.
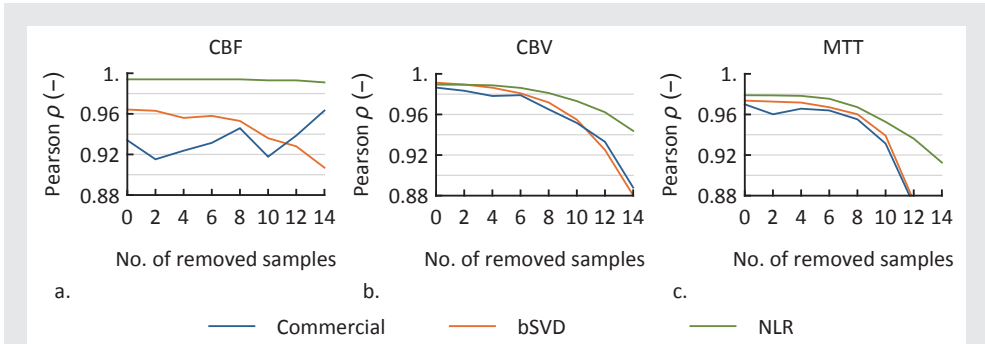
2

Fig. 2.7: Correlation with ground truth as a function of truncation level. a) cerebral blood flow, b) cerebral blood volume, and c) mean transit time. The figures show the Pearson coefficients of the correlation of the estimated perfusion values with the ground truth in the phantom versus the number of removed samples.

As for bias owing to truncation of the TACs: The bSVD method showed a negative bias in CBF and CBV as result of truncation, the NLR method seems to have no bias in either of the parameters, and the commercial method showed rather irregular biases as a function of the number of removed samples (Fig. 2.8). When 14 samples were removed, the commercial method failed to estimate the area under the VOF, for which reason the CBF and CBV were overestimated by 42% and 27%, respectively.
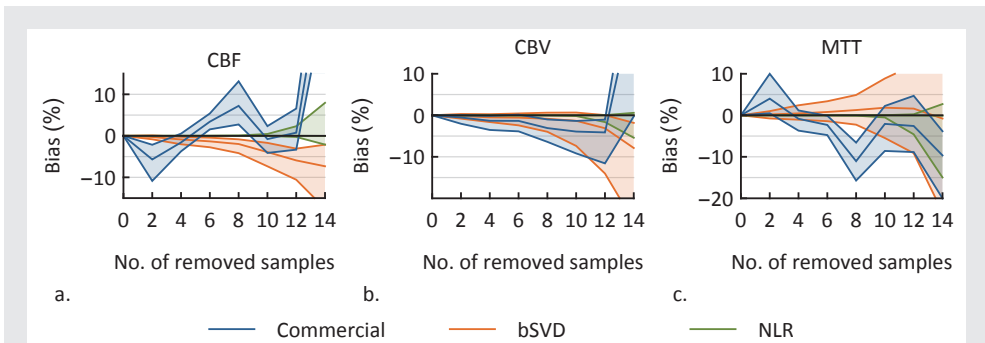

Fig. 2.8 Bias of the perfusion analysis methods due to truncation. a) Cerebral blood flow, b) cerebral blood volume, and c) mean transit time. The figures show the median and interquartile ranges of the bias of estimated perfusion values to the estimates without removed samples, as a function of the number of removed samples.

2.3.4 Clinical Data

Although the commercial method and bSVD were about five times faster than NLR, all three methods were able to analyze single clinical CTP slices within a second on a high-end desktop computer, and are therefore fast enough for clinical use.

Fig. 2.9 shows an example of three NLR perfusion maps of clinical data. The slopes and Pearson coefficients of the correlation of the commercial method and NLR with the bSVD standard are given in Table 2.2, along with the ipsilateral and contralateral perfusion values.

The NLR method provided higher correlation with bSVD than the commercial method in all cases. There were however considerable differences between the average perfusion values measured by the three methods. The CBF values measured with NLR were more than 2× as high as measured with bSVD, and those measured with the commercial method 1.5× as high. CBV values were comparable between NLR and bSVD inasmuch as both the slope and correlation coefficient were close to 1. The CBV values measured with the commercial method were 1.4× higher than those measured with bSVD. The average MTT values were comparable between the commercial method and bSVD, although the correlation coefficients were low. The MTT values measured with NLR were lower than those measured with bSVD.

Table 2.2: Responses to clinical data. Slopes and Pearson coefficients of the correlation of the commercial and NLR methods with the bSVD standard, and the ipsilateral and contralateral CBF (ml/100g/min), CBV (ml/100g), and MTT (s). The presented values are medians of the 50 CT perfusion scans, with interquartile ranges between brackets.

|		Commercial method	bSVD	NLR
Linear correlation with bSVD: Slope	CBF	1.55 (1.37, 1.83)	1	2.34 (1.92, 2.65)
	CBV	1.38 (1.22, 1.53)	1	1.06 (1.02, 1.09)
	MTT	0.97 (0.85, 1.09)	1	0.74 (0.54, 0.82)
Linear correlation with bSVD: Pearson ρ	CBF	0.66 (0.56, 0.76)	1	0.80 (0.76, 0.84)
	CBV	0.73 (0.69, 0.75)	1	0.99 (0.99, 0.99)
	MTT	0.51 (0.39, 0.76)	1	0.65 (0.54, 0.76)
Ipsi-lateral value	CBF	34.5 (23.9, 41.5)	23.0 (15.5, 26.2)	44.8 (28.7, 60.7)
	CBV	3.70 (3.08, 4.29)	2.62 (2.05, 3.11)	2.85 (2.01, 3.37)
	MTT	8.33 (6.85, 10.1)	8.00 (7.23, 8.76)	6.27 (4.11, 7.95)
Contra-lateral value	CBF	38.1 (28.1, 50.9)	24.9 (16.3, 29.6)	57.2 (37.1, 74.0)
	CBV	3.77 (2.98, 4.45)	2.70 (2.08, 3.14)	2.88 (1.93, 3.39)
	MTT	6.30 (5.58, 7.33)	7.01 (6.34, 7.72)	3.71 (3.22, 4.63)

| Filtered | CBF | CBV | MTT |
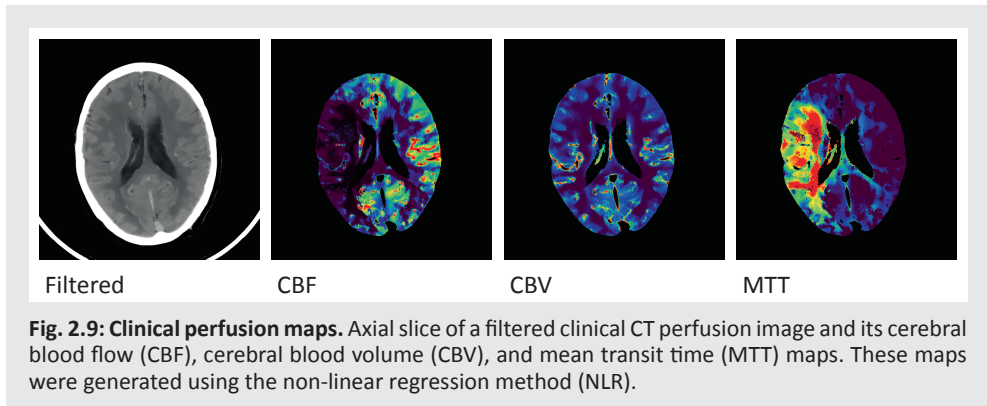
Fig. 2.9: Clinical perfusion maps. Axial slice of a filtered clinical CT perfusion image and its cerebral blood flow (CBF), cerebral blood volume (CBV), and mean transit time (MTT) maps. These maps were generated using the non-linear regression method (NLR).

2.4 DISCUSSION

This study has demonstrated that the proposed NLR method for CT brain perfusion analysis competes with current commercial and academic state-of-the-art methods. NLR provides a unified way of estimating CBF, CBV, and MTT, it requires few tuning parameters, and it can be extended to account of vascular permeability and to include additional constraints or prior knowledge about the IRF. The method was found to be robust to noise, to truncation, and to tracer delay.

2.4.1 Phantom Data

The commercial method, NLR, and bSVD all showed high Pearson correlation coefficients with the ground truth ($\rho > 0.9$).

Both being SVD-based, the commercial method and bSVD showed perfusion maps with visually similar trends. Both methods underestimated CBF values and overestimated MTT values in hyperperfused areas, i.e. at the right side of the phantom. It is likely that this occurred because of regularization (smoothing) of the IRF, which decreased the amplitude. The responses of the NLR method were more linear, which is reflected by the higher R^2 values for the linear fits.

All methods, but NLR in particular, showed that the perfusion values measured in the phantom were dependent on IRF shape. It was found that when the distribution of transit times in the IRF becomes wider (the exponential IRF having the widest distribution and the box-shaped IRF the smallest), the estimated CBF values decreased and MTT values increased. For both SVD-based methods this is most likely the result of the SVD regularization, which decreases the amplitude of the IRF as described above, whereas for the NLR method this is caused by the underlying model assuming a flat, box-shaped IRF.

2.4.2 Response to Noise

The effect of noise on the correlation of the perfusion maps with the ground truth was similar for all methods. The bias of the median perfusion values due to noise exhibited different trends, however, owing to fundamental differences between NLR and the SVD-based methods.

The NLR method showed a positive bias on CBF, but no bias on CBV and MTT. This can be explained by the fact that it is difficult to estimate high flow values since the dispersed AIF acts as a low-pass filter that limits temporal resolution. The noise on CBF therefore increases with increasing CBF (note that CBF = CBV/MTT), which results in a skewed distribution and a positive bias.

The commercial method and bSVD, both SVD-based, apply adaptive regularization to suppress noise in the IRF. An increased noise level requires stronger smoothening of the IRF, resulting in a wider curve with lower amplitude, i.e. higher MTT and lower CBF. For this reason both methods showed a positively biased median MTT due to noise. The bSVD method furthermore showed a negatively biased CBF. The CBF of the commercial method was however positively biased due to the overestimated CBV.

Although all three methods showed biased CBF values due to noise, the impact of these biases in clinical applications will probably be moderate. As discussed above, the biases are most significant in the hyperperfused (healthy) areas, and are therefore unlikely to affect tissue classification.

2.4.3 Response to Truncation

It was found that the NLR method was more robust to truncation than the commercial and bSVD methods, since it yielded perfusion values with higher correlation to the ground truth, and no bias in median value due to truncation. Whereas the SVD-based methods do not assume a model, the box-shaped IRF model used by the NLR method allows extrapolation of the truncated curves, resulting in unbiased estimates.

It was unclear why the commercial method showed a rather irregular bias in CBF and MTT due to truncation.

The commercial method furthermore showed severely overestimated CBV and CBF values when the attenuation curves were truncated by 14 samples. This was caused by erroneous curve-fitting of the truncated VOF.

2.4.4 Clinical Data

With respect to the clinical scans, the NLR perfusion maps showed higher correlation with bSVD than the maps generated by the commercial clinical software.

The CBF estimates in the 50 perfusion scans were more than 2× higher when measured with the NLR method than measured with the bSVD method, and were also higher than

measured with the commercial method. This large difference can be explained by the opposite biases due to noise found in the phantom study, and also by the difference in slope as measured with the box-shaped phantom IRF (Table 2.1). This suggests that the physiological IRF mostly resembles this box-shape, which is supported by simulations published by Bredno et al. (2010), and assumed in many tracer-kinetic models for tissue perfusion.[24,69,80,132]

MTT values measured with NLR were lower than those measured with bSVD. This is also in line with the biases due to noise as found in the phantom study.

The commercial method showed higher CBV values than bSVD and NLR in the 50 perfusion scans, as well as elevated CBV values with respect to the ground truth in the perfusion phantom. Possible explanations are differences in hematocrit correction or in curve fitting of the AIF and VOF.

Although ground truth perfusion values for the clinical scans were not available, which is a limitation of this study, highly quantitative Xe-CT and ^{15}O-PET studies confirmed average literature CBF values of about 50 ml/100g/min and average transit times of about 3 to 5 s in the healthy hemisphere (gray and white matter combined).[58,151,153] The NLR method provided better matching values (57 ml/100g/min and 3.7 s) than the commercial method (38 ml/100g/min and 6.3 s) and bSVD (25 ml/100g/min and 7.0 s). A previous study also reported that bSVD underestimates quantitative CBF values, presumably due to image noise.[123]

2.4.5 Limitations

The study has other limitations besides the lack of ground truth clinical perfusion values as mentioned in the previous paragraph. Although the IRF of cerebral tissue is frequently modeled as a box function, the true physiological shape is unknown. To our knowledge no accurate IRF has ever been measured with high resolution. The phantom study showed, however, that the investigated methods all correlated well with the ground truth, regardless of the IRF shape used.

It should also be noted that the commercial method uses a different curve fitting algorithm for partial volume correction than the NLR and bSVD methods. This means that the differences in CBV and CBF might have been influenced by the robustness of curve fitting, especially in the case of the truncated VOF curves. MTT values are not changed by partial volume correction.

2.5 CONCLUSIONS

Being model-free, i.e. being independent of an assumption of IRF shape, is often presented as an advantage of SVD-based methods. This study showed, however, that the use of a tracer kinetic model has some striking advantages over SVD-based methods. Least-squares fitting of the IRF model does not require regularization, it enables extrapolation in case of truncated data, and all required parameters can be modeled and measured in a unified way. This results in better robustness to noise, to truncation, and to tracer delay. However, since the clinically used thresholds were established on perfusion estimates that were most likely biased, they cannot be applied to perfusion maps generated by a different method and may therefore need revision.

In conclusion, the proposed fast NLR method provides a simple, flexible, and reliable way of estimating perfusion parameters from CT perfusion scans. This suggests it could be a viable alternative to the current commercial and academic perfusion analysis methods.

3
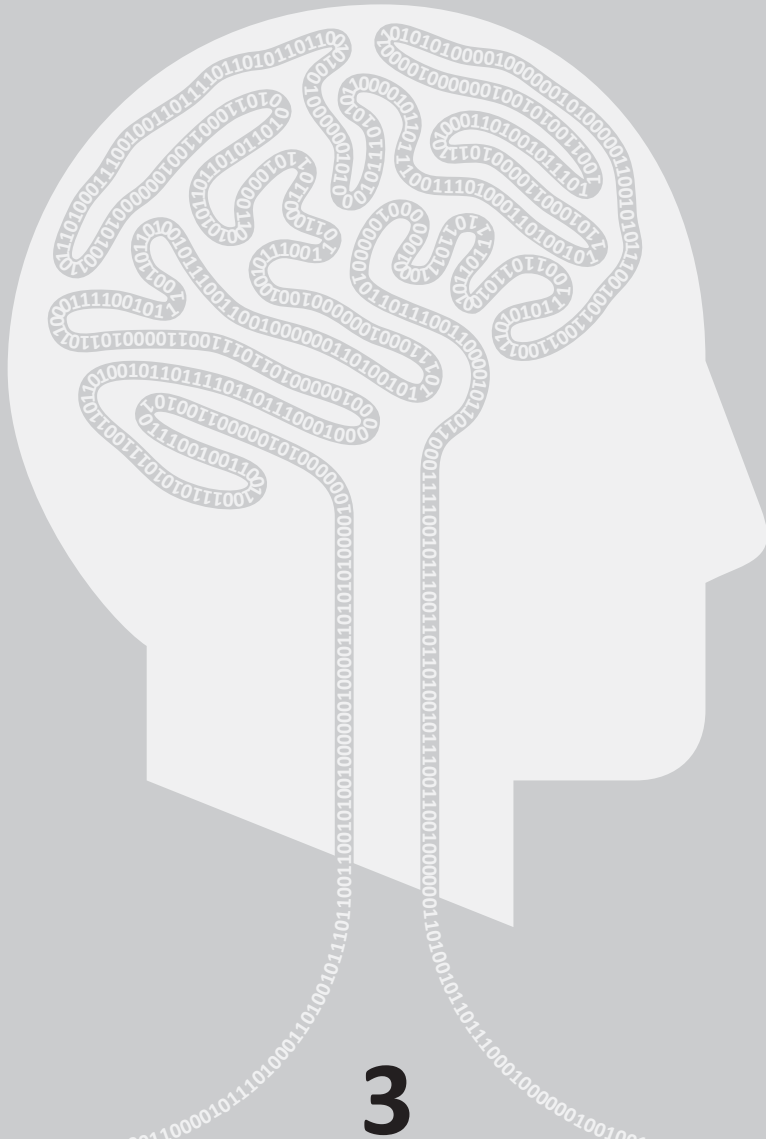
Model-based Permeability Analysis

ABSTRACT

Blood-brain-barrier damage, which can be quantified by measuring vascular permeability, is a potential predictor for hemorrhagic transformation in acute ischemic stroke. Permeability is commonly estimated by applying Patlak analysis to CT perfusion data, but this method lacks precision. Applying more elaborate kinetic models by means of non-linear regression (NLR) may improve precision, but this is more time-consuming and therefore less appropriate in an acute stroke setting. We propose to extend the fast method introduced in Chapter 2 to include permeability and obtain a simplified NLR method that may be faster and still precise enough for clinical use.

The aim of this study is to evaluate the reliability of in total 12 variations of Patlak analysis and NLR methods, including the simplified NLR method. Confidence intervals for the permeability estimates were evaluated using simulated CT time-attenuation curves with realistic noise, and clinical data from 20 patients.

Although fixating the blood volume improved Patlak analysis, the NLR methods yielded significantly more reliable estimates, but took up to 12× longer to calculate. The simplified NLR method was approximately 4× faster than other NLR methods, while maintaining the same confidence intervals.

In conclusion, the simplified NLR method is a new, reliable way to estimate permeability in stroke, fast enough for clinical application in an acute stroke setting.

3.1 INTRODUCTION

It has previously been hypothesized that blood-brain-barrier (BBB) damage is a predictor for hemorrhagic transformation (HT) in acute stroke.[18,33,88] With CTP imaging, frequently used for the evaluation of acute stroke, BBB damage can be quantified by measuring vascular permeability. Along with other perfusion parameters, including cerebral blood volume (CBV) and flow (CBF), vascular permeability is a tissue property that can be estimated by comparing tissue time-attenuation curves (TACs) to the curve of a reference artery or arterial input function (AIF). Whereas CBF and CBV can be measured by imaging the first pass bolus passage, leakage of contrast agent to the extravascular space is a slower process, only discernible in a delayed phase, and therefore requiring longer scan times. In stroke imaging, permeability is most frequently estimated using linearized regression, i.e. by graphical analysis of a Patlak plot.[33,81,88,109,110] This technique transforms the data in the enhancement curves so that, in case of irreversible leakage, the data points lie on a straight line when the capillary tracer concentration reaches steady-state. The permeability transfer constant K^{trans} is the slope of this line, and the relative blood volume is the intersection with the *y*-axis. Patlak analysis is used in e.g. Extended Brilliance Workspace 4.5 (Philips Healthcare, Best, the Netherlands), syngo Volume Perfusion-CT Neuro 2010 (Siemens Healthcare, Erlangen, Germany), and Vitrea fX 6.4 (Toshiba Medical Systems, Otawara-shi, Japan).

The Patlak method is preferred in the acute stroke setting, because it is fast, despite some inherent drawbacks. First, due to the linearized regression, only the steady-state data points, i.e. the last part of the scan, can be used. The estimated values are therefore dependent on the definition of the onset of this steady-state, and potentially useful information in the first part of the signal is disregarded. Second, linear least-squares regression assumes that the errors on the samples are normally distributed. For linearized data this is not the case and therefore the result will not be an optimal least-squares fit.[97] Third, other parameters, such as the CBV and CBF, are estimated using a different method, which usually includes Gaussian or gamma variate curve fits, or a regularized inverse filter.[78] Because two different methods are used for estimating parameters that essentially describe the same tissue model, the results may disagree. For example, the CBV, which should measure the intravascular volume only, may be overestimated by methods that do not take into account the additional extravascular distribution volume due to increased permeability of the BBB.[71,119]

A tissue perfusion model, as described in the previous chapter, extended to account of permeability, could serve as an alternative to the Patlak method. Such a model, applied with non-linear regression (NLR), utilizes the full length of the TACs, does not transform the measurement errors, and allows simultaneous measurement of all perfusion parameters. For these reasons NLR methods may provide a superior alternative to the use of Patlak plots in stroke imaging.[18,85,132] However, NLR methods rely on iterative algorithms that are

relatively time-consuming. A rapid diagnosis is crucial for treatment of acute stroke, and therefore these methods may not be practical in an acute stroke setting.

The purpose of this study was to compare the reliability and computation time of permeability estimation using various implementations of the Patlak method and NLR methods using clinical and simulated data. In addition, a novel simplified NLR method is proposed as a faster potential alternative to existing NLR methods.

3.2 METHODS

This section first describes a first pass bolus model that is required for the calculation of some of the Patlak methods. Second, details are provided for the theory and technical implementation of different Patlak and NLR methods. Third, a novel method for non-linear regression, based on the AATH model, is introduced.[83] Table 3.1 summarizes all in this study included methods for estimating permeability. Finally, methods for evaluating the models' reliability of estimating K^{trans} in both simulated data and clinical CTP scans are presented.

Table 3.1: Overview of the methods. An overview of the studied methods and their free and fixed parameters, according to Eq. 3.10. MTT = 0 means that the method does not account of transit time, $V_e = \infty$ assumes irreversible leakage, and $t_d = 0$ indicates a delay-sensitive method.

Method	Free parameters	CBV	MTT	K^{trans}	V_e	t_d
Patlak	2	✓	0	✓	∞	0
Patlak + delay	3	✓	0	✓	∞	✓*
Patlak fixed	2	✓*	0	✓	∞	0
Patlak fixed + delay	3	✓*	0	✓	∞	✓*
AATH	4	✓	✓	✓	✓	0
AATH + delay	5	✓	✓	✓	✓	✓
NLR	3	✓	✓	✓	∞	0
NLR + delay	4	✓	✓	✓	∞	✓
NLR + V_e	4	✓	✓	✓	✓	0
NLR + V_e + delay	5	✓	✓	✓	✓	✓
Simpl. NLR	3	✓	✓	✓	∞	0
Simpl. NLR + delay	4	✓	✓	✓	∞	✓

*Estimated using gamma variate curve fitting.

3.2.1 First Pass Bolus Fitting
Some implementations of the Patlak plot (described below) require estimates of the CBV and time-to-peak (TTP). To obtain these values, and estimates for the CBF and mean transit time (MTT), the enhancement curves can be analyzed using a broad range of methods. Despite that more sophisticated methods exist for estimating the CBF and MTT, this study uses gamma variate curve fitting of the first pass bolus for obtaining the CBV and TTP,

because the variability in outcome between the methods for estimating these parameters was found to be very small.[78]

A gamma variate fit gives a robust estimate of the area under the curve (AUC) and TTP of the first-pass bolus in the enhancement curves.[6,43,95] Subsequently, the CBV can be estimated by dividing the AUC of the tissue curve by the AUC of the AIF.[71] The bolus arrival time (BAT), which is in this study used to define the start of contrast enhancement, is defined as the 0.05% quantile of the gamma variate fit (Fig. 3.6b).

3.2.2 Patlak Linearized Regression

An underlying assumption of Patlak analysis is that the vascular leakage is unidirectional, i.e. irreversible during the acquisition time (Fig. 3.1). In that case the total tracer concentration in the tissue, $C_t(t)$, can be described as a function of the capillary concentration $C_c(t)$, the intravascular CBV, and a transfer constant K^{trans} that represents the flow from the intra- to the extravascular space:

$$C_t\left(t\right) = K^{trans}\int_0^t C_c\left(\tau\right)\mathrm{d}\tau + \mathrm{CBV}C_c\left(t\right)$$

<div align="right">Eq. 3.1</div>
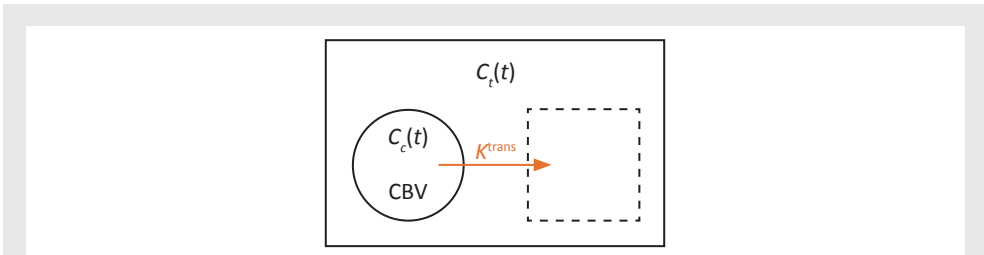
Fig. 3.1: Unidirectional two-compartment model. The solid circle represents the intravascular compartment, and the dashed square represents the extravascular, extracellular compartment. The Patlak model assumes irreversible leakage, meaning unidirectional flow from the intravascular compartment to the extravascular, extracellular compartment. The magnitude of this flow is equal to $K^{trans} \times C_c(t)$. Note that the tissue concentration, $C_t(t)$, is the weighted sum of both the intravascular concentration, $C_c(t)$, and the extravascular concentration (Eq. 3.1).

If both sides of the equation are divided by $C_c(t)$, a parametric relationship is found that should be linear when the capillary concentration reaches a steady state:

$$y\left(t\right) = \frac{C_t\left(t\right)}{C_c\left(t\right)} = K^{trans}x\left(t\right) + \mathrm{CBV}$$

<div align="right">Eq. 3.2</div>

$$x\left(t\right) = \frac{\int_0^t C_c\left(\tau\right)\mathrm{d}\tau}{C_c\left(t\right)}$$

<div align="right">Eq. 3.3</div>

Eq. 3.2 shows that when a linear fit $y(t) = ax(t) + b$ is applied to the Patlak plot of the delayed phase[33] of the enhancement curves, the slope of the fit (a) and its intersection with the y-axis (b) give an estimation of respectively the transfer constant K^{trans} and the CBV (Fig. 3.2).

The onset of the delayed phase, in which steady state is reached, is in this study empirically defined as the arterial TTP plus 3.5× the standard deviation of the first pass bolus, measured using a gamma variate curve fit as described above. This is a reliable method since gamma variate fits give a robust estimate of the width and position of the first pass bolus peak.
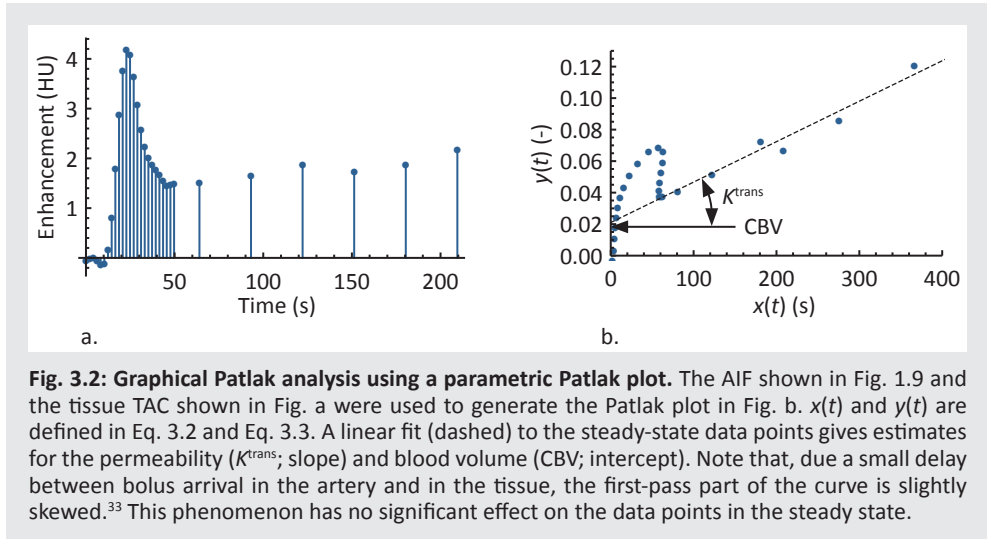

Fig. 3.2: Graphical Patlak analysis using a parametric Patlak plot. The AIF shown in Fig. 1.9 and the tissue TAC shown in Fig. a were used to generate the Patlak plot in Fig. b. $x(t)$ and $y(t)$ are defined in Eq. 3.2 and Eq. 3.3. A linear fit (dashed) to the steady-state data points gives estimates for the permeability (K^{trans}; slope) and blood volume (CBV; intercept). Note that, due a small delay between bolus arrival in the artery and in the tissue, the first-pass part of the curve is slightly skewed.[33] This phenomenon has no significant effect on the data points in the steady state.

Patlak Analysis with a Fixed Offset

The blood volume can be read from the Patlak plot. Alternatively, if an estimate of CBV is available from e.g. first pass bolus analysis, K^{trans} can be estimated more robustly, using the prior estimated CBV as a fixed offset (see Eq. 3.2).[23]

For comparison, both the 'standard' and the 'fixed' Patlak methods are examined (Table 3.1).

Patlak Analysis with Delay Correction

In CTP imaging the arterial concentration $C_a(t)$ rather than the capillary concentration $C_c(t)$ is measured to solve Eq. 3.2. In comparison to $C_a(t)$, the average capillary tracer concentration can be affected by an arterial delay and the transit time in the tissue. Schneider et al. (2011) suggested correcting for such a delay by incorporating the difference in TTP between the tissue curve and the AIF, t_{dTTP}, taken from gamma variate curve fits to the first pass bolus, into Eq. 3.2:[128]

$$y(t) = \frac{C_t(t)}{C_c(t - t_{\text{dTTP}})}$$

Eq. 3.4

$$x(t) = \frac{\displaystyle\int_0^{t - t_{\text{dTTP}}} C_c(\tau)\,\mathrm{d}\tau}{C_c(t - t_{\text{dTTP}})}$$

Eq. 3.5

In line with this, both the 'standard' and 'fixed' Patlak methods are also extended with a delay correction (Table 3.1). The gamma variate fits to the AIF and tissue enhancement curves provide a robust estimate of the TTP values if the leakage is small.

3.2.3 Non-linear Regression

Permeability-enabled Perfusion Models

As explained in Section 1.3.3, tissue perfusion can be modeled by means of an impulse response function (IRF) $h(t)$. Convolution of the measured AIF, $C_a(t)$, with a computed estimate of $h(t)$, gives an estimate of the enhancement curve of the tissue, $C_t(t)$:

$$C_t(t) = C_a(t) * h(t)$$

Eq. 3.6

Sawada et al. (1989) found that the detailed Tissue Homogeneity (TH) model, describing the blood flow and permeability using a complex set of differential equations, fitted the physiology of the brain the best because of the high density and tortuous nature of the brain capillary network.[61,124,132] The full TH model, however, lacks a closed-form time domain solution. Lawrence and Lee (1998) noticed that, because the contrast agent concentration in the extravascular space changes slowly relative to that in the intravascular space, the impulse response function of the TH model can be very well approximated by a box function followed by an exponential decay.[83] In this adiabatic approximation to the TH model (AATH), a box function with a width of t_t seconds (the transit time) represents the intravascular phase, and an exponential decay represents the extravascular phase:

$$h_{\text{AATH}}(t) = \mathrm{CBF}\left(1 - U(t - t_t)\right) + K^{\text{trans}}\,U(t - t_t)\,\mathrm{e}^{-\frac{K^{\text{trans}}}{V_e}(t - t_t)}$$

Eq. 3.7

In Eq. 3.7, $U(t)$ is the unit step function and V_e is the extravascular distribution volume (Fig. 3.3). Note that the intravascular CBV equals $t_t \times$ CBF. Because this model gives estimates for t_t and CBF as opposed to models that only estimate CBV, this type of model is often referred to as a *distributed parameter model*, in contrast to *lumped parameter models* like the extended Tofts model (ETM).[136]
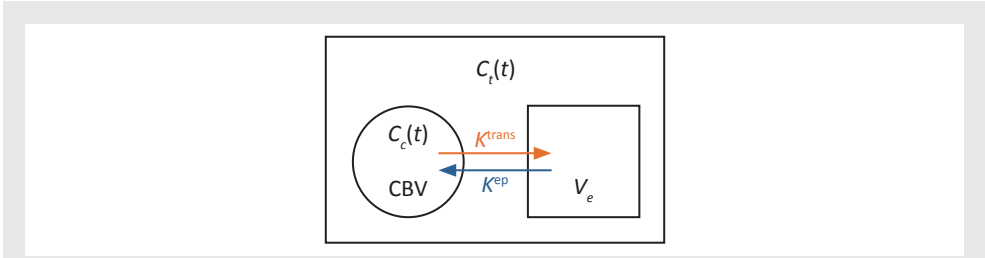
Fig. 3.3: Bidirectional two-compartment model. The circle represents the intravascular compartment, and the square represents the extravascular, extracellular compartment. In contrast to the Patlak model, the AATH model also takes leakage from the extravascular, extracellular compartment to the intravascular compartment into account. V_e is the apparent volume fraction of this extravascular compartment. Note that the inverse permeability rate constant, K^{ep}, equals K^{trans}/V_e.

The AATH model describes the tracer concentration dynamics in a small volume containing a single capillary vessel with a uniform (plug) flow. In reality, however, brain tissue is heterogeneous and even a small volume contains capillaries with variable lengths. This heterogeneity causes a small tissue volume to have a distribution of transit times $P(t_t;\text{MTT})$, rather than one unique transit time t_t (see Section 1.3.3). MTT is the mean transit time of this distribution. When this distribution is taken into account, the full model that is used in this study becomes:

$$h_{\text{full}}\left(t;\text{MTT}\right)=\int_0^\infty h_{\text{AATH}}\left(t;t_t\right)P\left(t_t;\text{MTT}\right)\mathrm{d}t_t \qquad \text{Eq. 3.8}$$

In this equation, $h_{\text{AATH}}(t;t_t)$ is the IRF of the AATH model for transit time t_t, and $P(t_t;\text{MTT})$ is the probability for t_t given an MTT.

Bredno et al. (2010) found, using highly detailed simulations, that an exponential decay with a delay of $a \times \text{MTT}$ is a good approximation for $P(t_t;\text{MTT})$ in case $a = 0.632$.[24] The equation for this distribution can be written as:

$$P\left(t_t;\text{MTT}\right)=k_t\,\mathrm{U}\left(u\right)\mathrm{e}^{-k_t u}\,,$$

$$\text{with } u=t_t-a\text{MTT and } k_t=\frac{1}{\left(1-a\right)\text{MTT}} \qquad \text{Eq. 3.9}$$

Solving the model assumes knowledge about the capillary concentration. In practice, due to resolution and noise limits, the AIF is measured in a large artery, often located away from the tissue of interest, so extra travel time for the contrast to arrive in the tissue needs to be accounted for. This is particularly important in the study of tissue regions that are fed through collateral routes. It has been shown that the performance of other deconvolution methods is improved by making them delay-insensitive.[73,77] This can be done by introducing

an additional parameter for the delay, t_d. In the rare case that a collateral artery is chosen for the AIF, t_d could even be negative at the contralateral side. By substituting Eq. 3.7 and Eq. 3.9 into Eq. 3.8, and introducing t_d, the following solution is obtained:

$$h_{full}(t) = CBF\left(U(t - t_d) - U(u)\right) + CBF\ U(u)\left((1 - p)e^{-k_t u} + p e^{-k_p u}\right),$$

$$\text{with } u = t - t_d - a\text{MTT}, k_p = \frac{E\text{CBF}}{V_e}, k_t = \frac{1}{(1-a)\text{MTT}}, \text{and } p = \frac{1}{1 - k_p / k_t}$$

Eq. 3.10

The parameter E ($0 \le E \le 1$) in this equation is the fraction of the flow that leaks into the extravascular space, i.e. $K^{trans} = E \times \text{CBF}$.

The AATH model (Eq. 3.7), and also the tracer-kinetic models used by Larson et al. (1987), are subclasses of $h_{full}(t)$ in which a approximates 1 and $t_d = 0$.[80] The extended Tofts model, frequently used in DCE-MR analysis, reduces complexity by combining the flow and transit time into a single variable for the blood volume (a lumped parameter), requiring that MTT approximates 0 and $t_d = 0$. The IRF for the standard Patlak model, i.e. assuming irreversible leakage, would require that MTT approximates 0, $t_d = 0$ and $V_e = \infty$.[109]

Simplified Non-Linear Regression

Non-linear regression with 5 unknown variables is a computational intensive task. Bottlenecks involve the calculation of exponentials, divisions, and a convolution operation in each iteration.

However, the computational complexity is highly reduced by two simplifications to $h(t)$. Assuming that a approximates 1 and $V_e = \infty$, the two exponentials can be reduced to respectively 0 and 1, and $h(t)$ can be written as the sum of two step functions:

$$h_s(t) = \lim_{a \to 1^-, V_e \to \infty} h(t) = CBF\ U(t - t_d) - (1 - E)CBF\ U(t - t_d - t_t)$$

Eq. 3.11

What is even more important is that it is now no longer necessary to apply a convolution in each iteration. The convolution of the AIF, $C_a(t)$, with a shifted unit step function $U(t - t_d)$ equals:

$$\int_{-\infty}^{t} C_a(\tau)U(t - t_d - \tau)d\tau = \int_{0}^{t - t_d} C_a(\tau)d\tau, \forall t \ge t_d$$

Eq. 3.12

The integral of $C_a(t)$ just needs to be calculated once, and the convolution of the $C_a(t)$ with $h_s(t)$ can be reduced to two interpolations into this integral, at respectively $t - t_d$ and $t - t_d - t_t$. This simplified version of $h(t)$ can be used to give estimates of MTT, CBF, K^{trans}, and t_d that would be found if the full model was used. These estimates are also used as initial parameters to initialize fitting the full model.

3.2.4 Discretization

A crucial step in numerical NLR (and signal-processing in general) is proper band-limiting. According the Nyquist criterion, the small discrete number of CTP samples in a TAC allow only certain frequencies to be reconstructed from the signal. Other frequencies need to be removed from the signal; if $h(t)$ is not band-limited, then high-frequency aliasing causes spurious local minima that spoil the regression. To suppress frequency components above the Nyquist frequency, both $h(t)$ and $C_t(t)$ were band-limited using a Bartlett kernel (triangular). To fulfill the Nyquist criterion, the FWHM of the kernel was set to 2× the sample interval, which is in this case 2× 2 s.

Fig. 3.4 shows an example of an analytical, continuous IRF $h(t)$ and its band-limited, sampled version.

Fig. 3.4: Band-limited IRF. An example of $h(t)$ (solid line) and its band-limited, sampled version (dots). In this case $a = 0.632$, and the values of the perfusion variables are MTT = 7 s, CBF = 30 ml/100g/min, K^{trans} = 3 ml/100g/min, V_e = 2.5 ml/100g and t_d = 1 s.
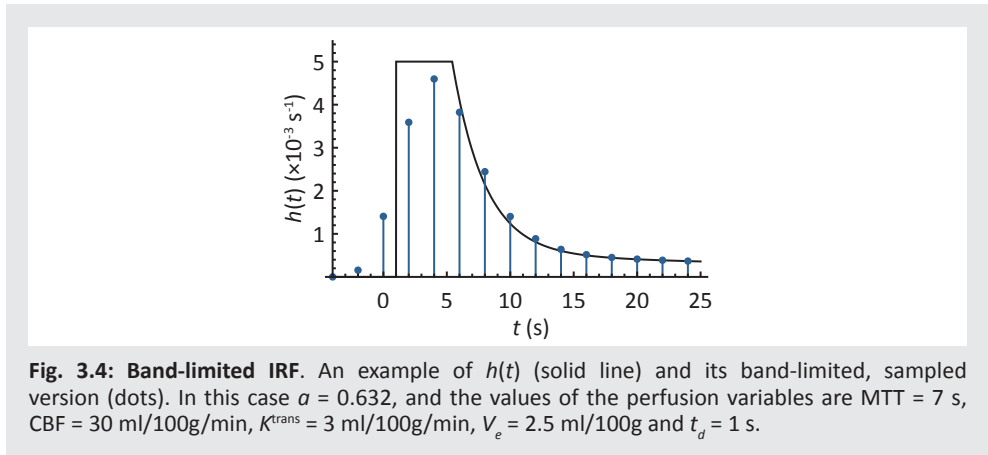
Band-limited sampling of analytical functions is usually done by computing a high-resolution version of the function, followed by downsampling with a band-limiting (smoothing) kernel. The convolution of the basis functions of $h(t)$, the unit step function $U(t)$ and the truncated exponential $U(t)e^{-kt}$, with a Bartlett kernel $b(t;d)$, however, have relatively simple analytical solutions. These solutions are given in Eq. 3.13 and Eq. 3.14, and shown in Fig. 3.5. The parameter d is the FWHM of the triangular Bartlett kernel. These solutions enable the band-limited IRF to be expressed in analytical form, which is more precise and does not require the computation of a high-resolution version.

$$\int_{-\infty}^{\infty} U(\tau)b(t-\tau;d)\,d\tau = \frac{1}{2d^2}\begin{cases} 0 & t \leq -d \\ d^2 + 2dt + t^2 & d < t \leq 0 \\ d^2 + 2dt - t^2 & 0 < t < d \\ 2d^2 & t \geq d \end{cases} \qquad \text{Eq 3.13}$$

$$\int_{-\infty}^{\infty}\mathsf{U}(\tau)e^{-k\tau}\,b(t-\tau;d)\,\mathrm{d}\tau = \frac{1}{d^2k^2}\begin{cases} 0 & t \leq -d \\ e^{-kt-dk}-1+kt+dk & d < t \leq 0 \\ e^{-kt-dk}-2e^{-kt}+1-kt+dk & 0 < t < d \\ e^{-kt-dk}-2e^{-kt}+e^{-kt+dk} & t \geq d \end{cases} \qquad \text{Eq 3.14}$$
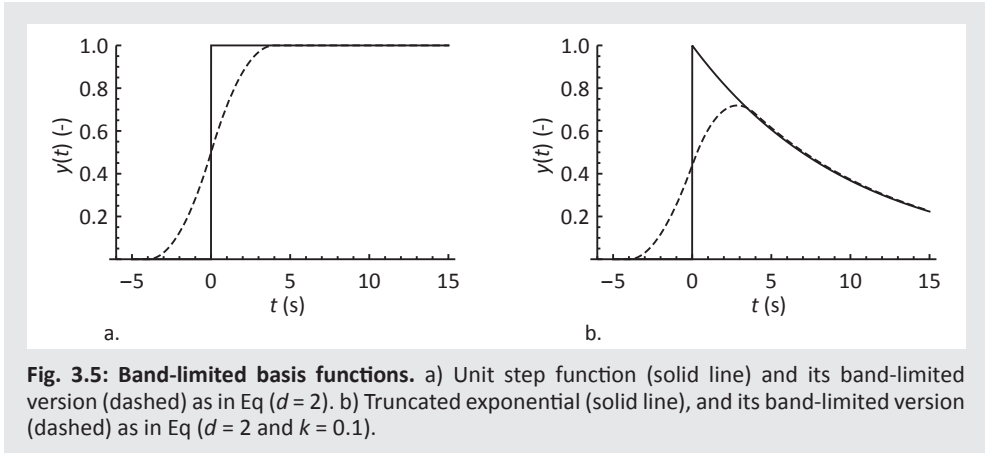
3

Fig. 3.5: Band-limited basis functions. a) Unit step function (solid line) and its band-limited version (dashed) as in Eq ($d = 2$). b) Truncated exponential (solid line), and its band-limited version (dashed) as in Eq ($d = 2$ and $k = 0.1$).

It should be noted that the functions in Eq. 3.14 become numerically unstable near $kt = 0$. This problem is solved by using a Taylor series approximation near that point.

In case of the simplified NLR method, the IRF $h(t)$ does not need to be calculated. In that circumstance it is sufficient to band-limit the AIF instead, which just needs to be done once.

3.2.5 Model Variations

A total of 12 different methods were compared. Both Patlak and the NLR methods include parameters that are either free for estimation or fixed to a predefined value. The full tissue response model $h(t)$ (Eq. 3.10) has 5 perfusion parameters, CBV, MTT, K^{trans}, V_e, and t_d. Table 3.1 gives an overview of all methods and parameters. The initial values for NLR were CBV = 4 ml/100g, MTT = 4 s, K^{trans} = 1.5 ml/100g/min, V_e = 20 ml/100g, and t_d = 1 s, and the initial step sizes were respectively 2 ml/100g, 5 s, 1.5 ml/100g/min, 25 ml/100g, and 2 s. The initial parameters for the full NLR model are optimized by first applying the simplified NLR model. For all NLR methods a generic Nelder-Mead downhill simplex method with linear constraints was used for optimization.[102,114]

If global optima are found, which is not guaranteed, then increasing the number of free parameters will result in a better fit (a higher R^2), but as a counter-effect it may decrease the reliability of the estimated values. In other words, adding complexity to a model may not necessarily improve the results.

All methods were implemented in a similar fashion in C routines that are accessible in Matlab (version 2011b, The MathWorks Inc., Natick, MA) through the Matlab MEX programming interface.

Simulations were applied to gain insight in the response of the models to noise and varying perfusion parameters, and CT brain perfusion scans were analyzed to estimate the reliability of the measured permeability in clinical practice.

3.2.6 Simulated Data

To evaluate in a setting with controlled noise levels and perfusion parameters, tissue TACs were simulated by convolving a measured AIF with a generated IRF, and adding Gaussian noise. An AIF (Fig. 3.6a) was extracted from a clinical CTP brain scan as described below.

The AATH model (Eq. 3.7) was used to generate the IRFs, because the TH model is thought to match the physiology of the brain better than other published models.[61,83,124,132] The blood flow *F* was kept constant at a rate of 15 ml/100g/min, which is comparable to an ischemic penumbra, and the leakage was assumed to be irreversible.[143]

The noise level, K^{trans}, MTT, and delay were varied between the simulations. Four sets of simulations were made. The first is a series of Monte Carlo simulations in which the K^{trans} was randomized between 0 and 2 ml/100g/min, MTT between 4 and 20 s, and the delay between 0 and 5 s. 1000 random simulations were made at noise levels of 0.5, 1.0, and 2.0 HU (SD).

In the remaining three sets, one out of three parameters was varied while the others were fixed to respectively 1 HU for the noise level, 0.5 ml/100g/min for the K^{trans}, 12 s for MTT. The delay was fixed to 0 s. In the second set only the standard deviation of the noise was varied between 0 and 2 HU, in the third set only the K^{trans} was varied between 0 and 2 ml/100g/min, and in the fourth set only MTT was varied between 4 and 20 s.

The simulated TACs were analyzed using all methods listed in Table 3.1, while keeping track of the mean, standard error, and approximate standard error of the estimated K^{trans} values.

Fig. 3.6a, c, and d give an overview of the measured AIF, and the default IRF and enhancement curve. Both the IRF and the AIF were band-limited using a Bartlett kernel (triangular) with a FWHM of 4 s. Fig. 3.6e and f show how the shape of $h(t)$ (Eq. 3.10) and the resulting enhancement curves change with different parameters.

3
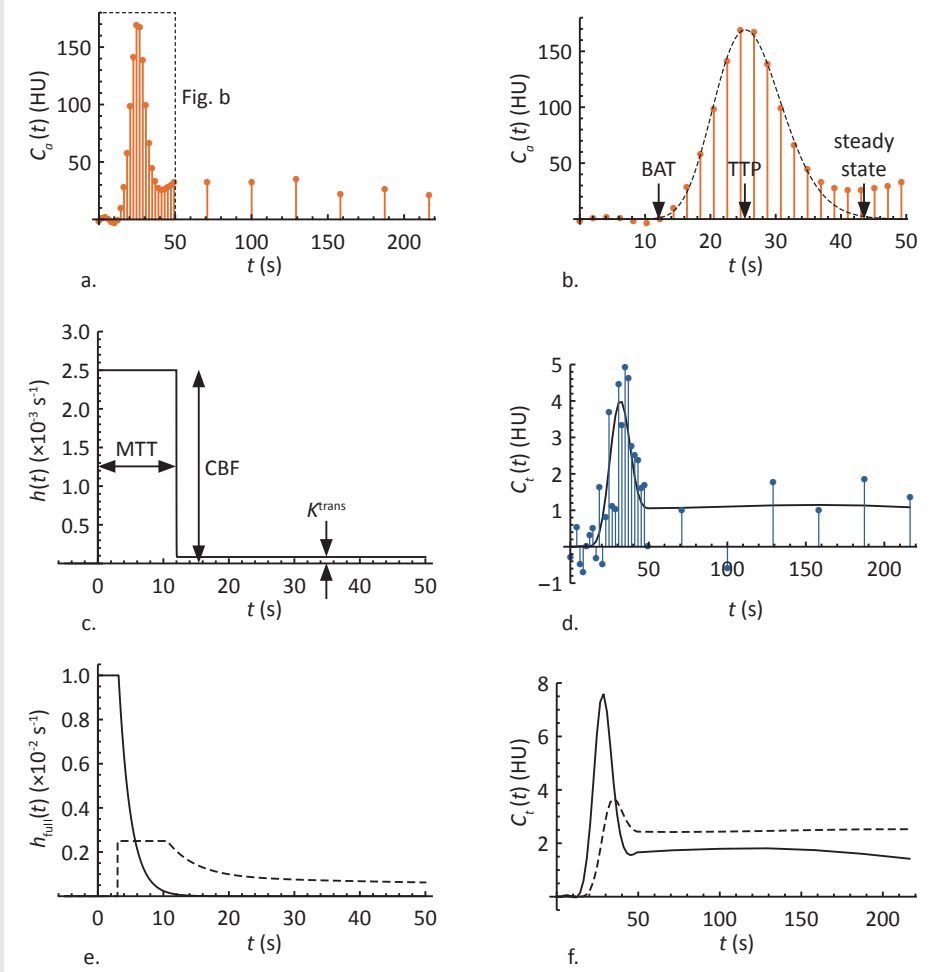
Fig. 3.6: Time enhancement curves. An overview of the AIF, and simulated impulse response functions and tissue enhancement curves. a) The full measured AIF. b) The first 50 seconds of the AIF showing the bolus arrival time (BAT) and time-to-peak (TTP), and steady state, estimated using a gamma variate fit (dashed line). c) The default impulse response function with an MTT of 12 s, a CBF of 15 ml/100g/min, and irreversible leakage with a K^{trans} of 5 ml/100g/min. d) A simulated enhancement curve, created by convolving the measured AIF (a) with the calculated IRF (c), and adding Gaussian noise with a standard deviation of 1 HU (dots). e) An example of $h_{full}(t)$ for CBV = 5 ml/100g, MTT = 5 s, t_d = 0 s, and no leakage (solid line), and $h_{full}(t)$ for CBV = 3 ml/100g, MTT = 12 s, t_d = 3 s, and reversible leakage with K^{trans} = 5 ml/100g/min, and V_e = 10 ml/100g (dashed line). f) Simulated tissue enhancement curves, created by convolving the measured AIF (a) with the IRFs in (e).

3.2.7 CT Brain Perfusion Scans

Data Acquisition

CTP scans of 20 consecutive acute ischemic stroke patients were included retrospectively from a single center (University Medical Center Utrecht) participating in the Dutch acute stroke study (DUST). The inclusion criteria and the CTP acquisition protocol are described in Section 1.4.

All included scans were acquired on a Philips Brilliance iCT scanner (Philips Healthcare, Best, the Netherlands) at 80 kVp and 150 mAs. These scans had an axial coverage of 65 mm at most and a field-of-view of approximately 200 mm × 200 mm. All scans had a total acquisition time of 210 s (see Section 1.4.2 and Fig. 3.6a) and were reconstructed into thin slices.

Pre-Processing

The open source registration toolbox Elastix was used to register the original, 3D high resolution CT perfusion data (voxel size 0.39 × 0.39 × 0.83 mm^3) to the first acquired volume.[67] Next, slabs of six adjacent registered slices were averaged to obtain 8 to 13 slabs of approximately 5 mm per volume.

Noise reduction is crucial in CT perfusion analysis. Because of the limited radiation dose, the unfiltered scans have a very low signal-to-noise ratio (SNR), especially in the areas with low perfusion where BBB damage is to be expected. Sophisticated noise filtering, where e.g. temporal information is used to adapt the filter kernel to its spatial neighborhood, is therefore desirable.

A temporal Gaussian filter with a standard deviation of 4 s, followed by a 3D bilateral filter (TIPS) with a spatial standard deviation (σ_d) of 4 mm and a profile-similarity standard deviation (σ_ξ) of 50 HU^2 were applied to reduce the noise with a minimum loss of resolution.[91]

Arterial Input Function

The AIF was semi-automatically selected in either an internal carotid or in the basilar artery by drawing a circular region of interest in which the TAC with the highest enhancement was chosen. To correct the AUC of the AIF for partial volume effect, a venous output function (VOF) was in the same way semi-automatically selected in a great sinus perpendicular to the slices, which is in line with the clinical protocol.[125] A gamma variate curve was fitted to both the AIF and VOF to estimate their AUCs, the arterial BAT, and the steady state concentration time (see Section 3.2.1).

Post-Processing

Only the voxels that were classified as penumbra (tissue at risk) were used for statistical analysis. This was done because the SNR of the TACs in the infarct (irreversible ischemia) is low, which might hamper reliable measurements. The K^{trans} in the remainder of the brain (healthy tissue) should in theory be nearly zero.

To extract the penumbra and exclude vessels, tissue types in the brain were segmented based on the CT values in the first acquisitions of the TIPS filtered scan, before the BAT. By removing voxels with a CT value smaller than 17 HU or larger than 55 HU (unenhanced), air, fat, and bone are excluded from the analysis, while gray and white matter remain included. Within the brain tissue the infarct and penumbra were defined based on the CBV and relative MTT (rMTT) that were estimated by the simplified NLR method.

In order to calculate the rMTT, a symmetry plane was manually drawn to separate the hemispheres. The original MTT map is mirrored over this plane and blurred by a 3D Gaussian kernel with a standard deviation of 3 mm. The rMTT values are found by dividing the original MTT map by the mirrored, blurred map.

Wintermark et al. (2006) found that the CBV most accurately describes the infarct, with an optimal threshold at 2.0 ml/100g, and that the rMTT most accurately describes the penumbra, with an optimal threshold at 145% and the infarct excluded.[147] A CBV threshold at 9 ml/100g was used to exclude vessels.

A correction factor $(1 - Ht_{large})/(1 - Ht_{small})$ was applied to correct the tracer concentration for the difference between in hematocrit (see Eq. 1.1 in Section 1.3.1).[71] The values used for Ht_{large} and Ht_{small} are respectively 0.45 and 0.25.[116] This correction affects all perfusion parameters that scale with the tracer concentration, i.e. CBV and CBF, but also K^{trans} and V_e.

Statistical Analysis

Besides the K^{trans} estimate itself, the approximate standard error on the estimated K^{trans} for each method was calculated in all voxels. 95% confidence intervals (CIs) were calculated by applying Student's *t*-distribution to these standard errors. Average CIs are more suitable for estimating the reliability than the standard deviation for two reasons. First, the standard deviation might represent a true variability instead of an error, which is what we like to measure. Second, the standard deviation might be biased due to constraints to the estimated parameter, i.e. K^{trans} cannot be negative, nor can it be larger than the flow.

The estimated values and CIs in the penumbra regions were averaged per patient and a Wilcoxon signed-rank test was applied to each pair of methods to test if the differences between the methods were significant ($p < 0.001$).

3.3 RESULTS

3.3.1 Simulated Data

Fig. 3.7 shows the standard error on the K^{trans} estimates in the Monte Carlo simulations for each method and at different noise levels. Fig. 3.8 shows graphs of the average K^{trans} estimates and CIs versus the varied input parameters (noise level, K^{trans}, and MTT). A narrower CI indicates a more reliable estimate. The results for the 6 delay corrected methods (Table 3.1) were very similar to the uncorrected methods, and for that reason the results for the delay corrected methods are not shown to make the graphs more readable. The NLR and simplified NLR methods showed very similar results, which caused these lines to overlap in all of the plots.

Fig. 3.7: Standard errors of the K^{trans} estimates for different noise levels. The bars show the standard errors of the K^{trans} estimates on Monte Carlo simulated TACs with a noise SD of respectively 0.5, 1.0, and 2.0 HU.
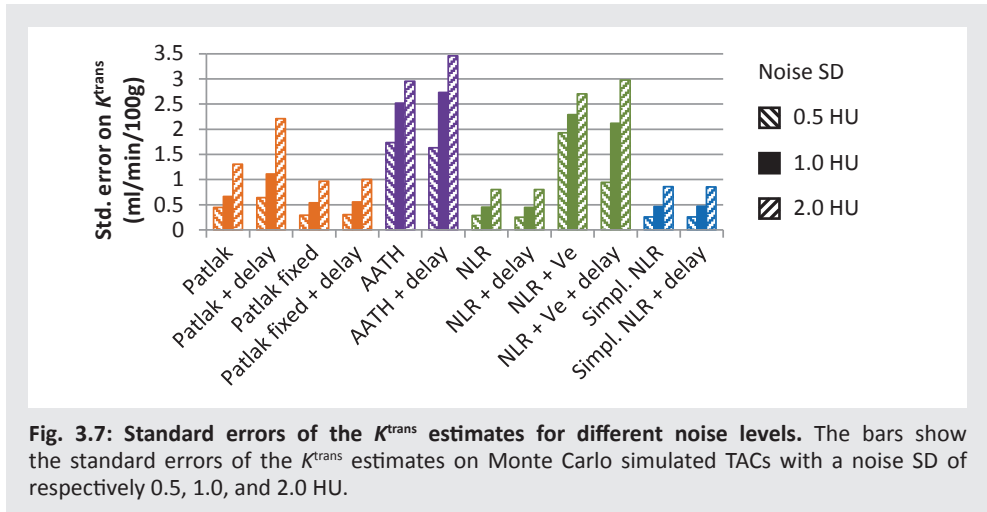
Because the steady state time was defined as the TTP plus 3.5× the standard deviation of the first pass bolus, 9 acquisitions were included for Patlak analysis.

The results showed that noise gives a positive bias to the average K^{trans} estimates (Fig. 3.8a), affecting the standard Patlak, AATH, and NLR+V_e the most. Fig. 3.8c shows that, at the default noise level of 1.0 HU, all methods had a positive bias for small K^{trans} values, whereas the methods that assume irreversible leakage ($V_e = \infty$) gave unbiased estimates for larger K^{trans} values. The bias for the methods that assume reversible leakage (AATH and NLR+V_e) is also reflected in the high standard errors in Fig. 3.7. Fig. 3.8e shows that the average K^{trans} is not affected by the MTT for transit times shorter than 12 s. For long transit times, the AATH and NLR+V_e methods overestimated the K^{trans}, whereas the standard Patlak method returned underestimated K^{trans} values.

3
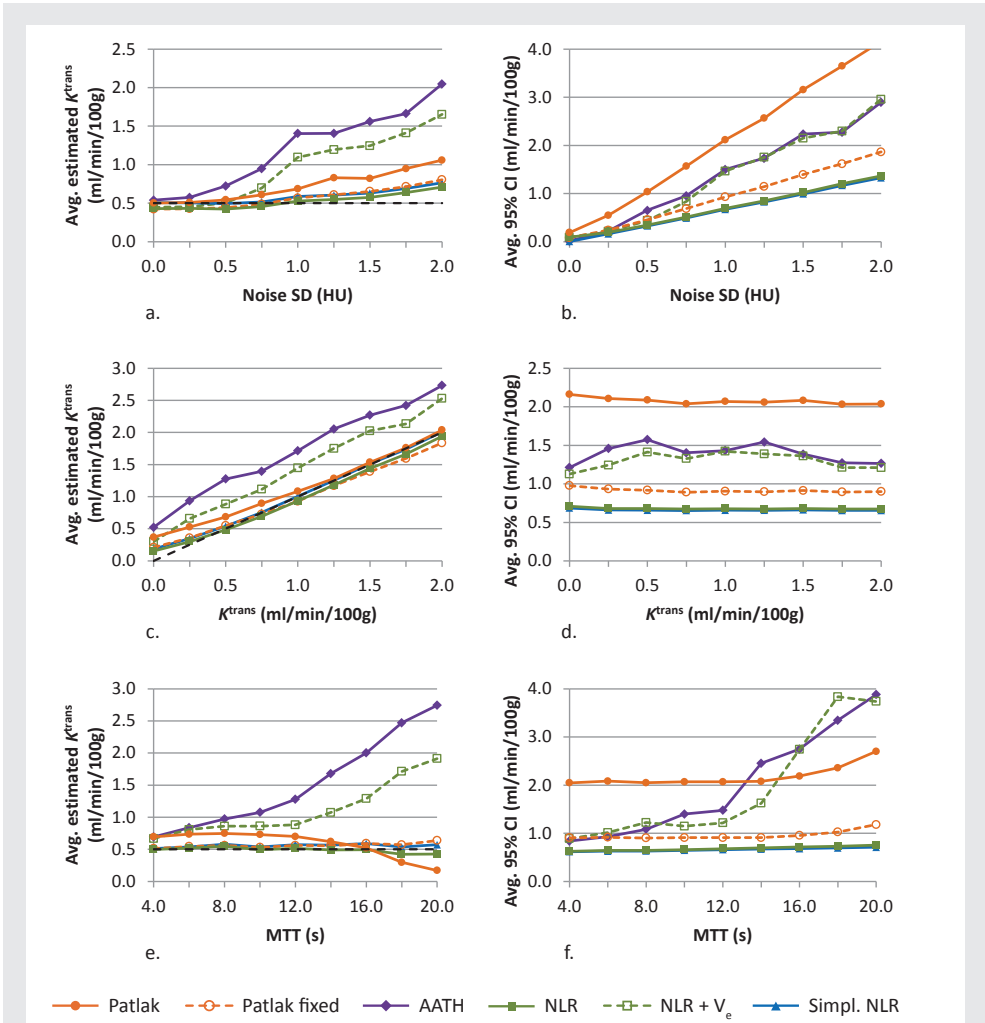
Fig. 3.8: Results of simulated enhancement curves. Graphs a, c, and e show average K^{trans} estimates of the simulated data, and graphs b, d, and f show their average 95% confidence intervals (CI). A narrower CI suggests a more reliable estimate. The NLR and simplified NLR methods showed very similar results, which caused these lines to overlap in all of the plots.

In all cases with noise, the NLR methods with irreversible leakage were found to have the smallest Cis, whereas the standard Patlak method had the largest CI, implying that it is least reliable (Fig. 3.8b, d, and f). All methods gave estimates of which the width of the CI scaled linearly with the noise level (Fig. 3.8b). Fig. 3.8d shows that the confidence of the estimation did not scale with the K^{trans} for the methods that assume irreversible leakage ($V_e = \infty$). The methods that assume reversible leakage, AATH and NLR+V_e, showed an increased CI for

K^{trans} values in the order of 1 ml/100g/min. For K^{trans} values higher than 2 ml/100g/min (not shown in the graph), however, the CI of these methods decreases again to reach a steady state of 0.4 ml/100g/min at a K^{trans} of 10 ml/100g/min, while CIs of the other methods are unaffected. In line with Fig. 3.8e, Fig. 3.8f shows that the average CI was not affected by the MTT for transit times shorter than 12 s. For long transit times, the AATH, NLR+V_e, and standard Patlak methods showed an increased CI.

3.3.2 CT Brain Perfusion Scans
K^{trans} maps and CI maps for K^{trans} were generated for 20 CTP scans (Fig. 3.9).

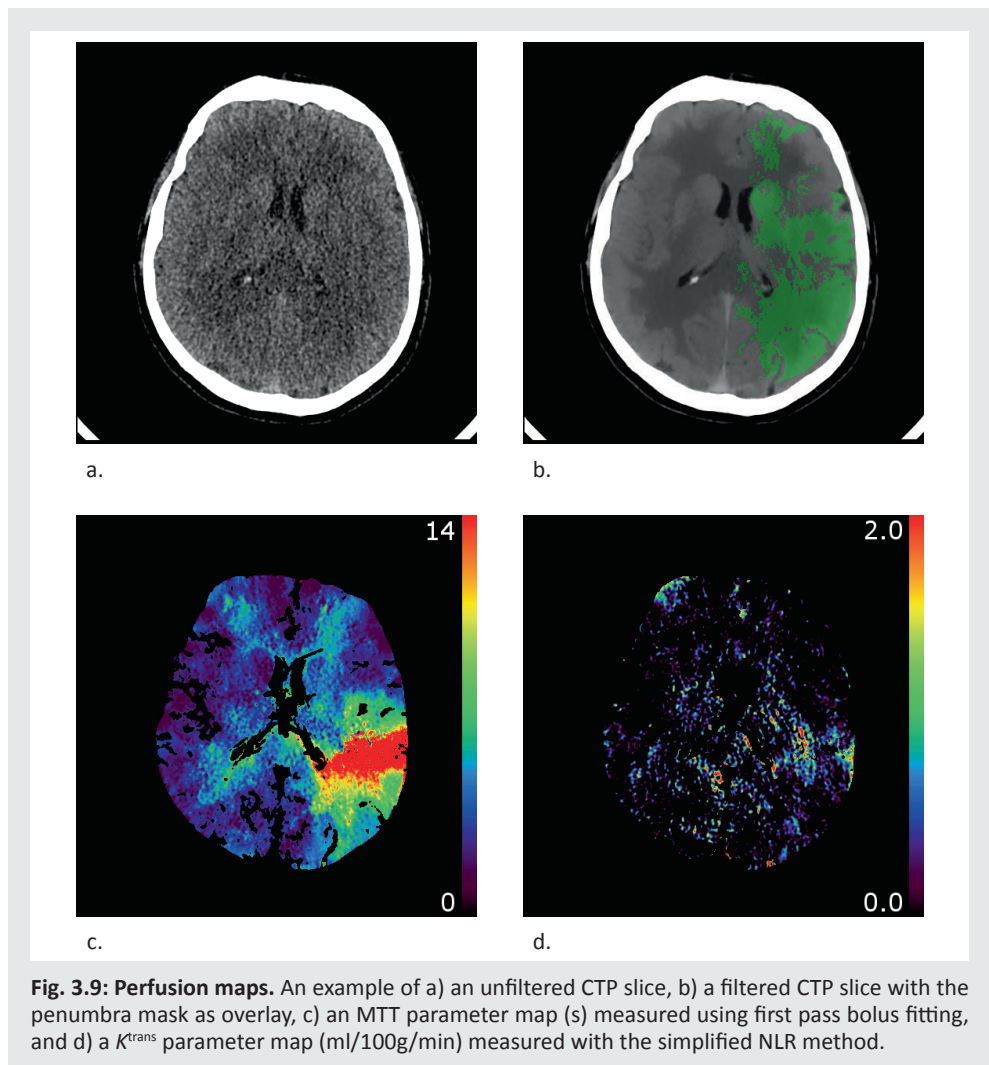**Fig. 3.9: Perfusion maps.** An example of a) an unfiltered CTP slice, b) a filtered CTP slice with the penumbra mask as overlay, c) an MTT parameter map (s) measured using first pass bolus fitting, and d) a K^{trans} parameter map (ml/100g/min) measured with the simplified NLR method.

There was a large variance in K^{trans} and CI between the patients (Table 3.2), but the Wilcoxon signed-rank tests (Table 3.3) demonstrated that the average CIs were significantly different between most methods that assume irreversible leakage.

Table 3.2: K^{trans} values and confidence intervals. The K^{trans} values and 95% confidence intervals (ml/100g/min) in the clinical data and in the simulations (default parameters). The values are ordered to the width of the confidence interval in the clinical data. The average confidence intervals are visualized in the graph in Fig. 3.10.

Method	Mean K^{trans}		Mean 95% CI width	
	Clinical data	Simulation	Clinical data	Simulation
Simpl. NLR	0.39 ± 0.23	0.59	0.82 ± 0.29	0.67
Simpl. NLR + delay	0.36 ± 0.21	0.57	0.82 ± 0.29	0.66
NLR	0.34 ± 0.21	0.53	0.85 ± 0.31	0.69
NLR + delay	0.33 ± 0.19	0.53	0.85 ± 0.32	0.67
Patlak fixed	0.43 ± 0.33	0.57	1.42 ± 0.49	0.93
Patlak fixed + delay	0.45 ± 0.35	0.58	1.53 ± 0.56	1.03
AATH	0.87 ± 0.89	1.40	1.95 ± 0.94	1.50
NLR + V_e + delay	0.72 ± 0.73	0.85	1.97 ± 1.06	1.25
AATH + delay	0.83 ± 0.88	0.95	2.04 ± 1.07	1.21
NLR + V_e	0.77 ± 0.77	1.10	2.18 ± 1.20	1.46
Patlak	0.73 ± 0.45	0.69	2.65 ± 1.33	2.11
Patlak + delay	0.78 ± 0.48	0.96	2.78 ± 1.45	2.10

Table 3.3: Significance of the difference in confidence interval. *p*-values for the Wilcoxon signed-rank tests on the 95% CIs for K^{trans} between the different methods. Probabilities smaller than 0.001 are considered significant and written as 0.

	Patlak	Patlak + delay	Patlak fixed	Patlak fixed + delay	AATH	AATH + delay	NLR	NLR + delay	NLR + V_e	NLR + V_e + delay	Simpl. NLR
Patlak + delay	0.001										
Patlak fixed	0	0									
Patlak fixed + delay	0	0	0								
AATH	0.056	0.035	0.015	0.052							
AATH + delay	0.13	0.073	0.012	0.030	0.018						
NLR	0	0	0	0	0						
NLR + delay	0	0	0	0	0	0	0.82				
NLR + V_e	0.23	0.15	0.009	0.017	0.005	0.15	0	0			
NLR + V_e + delay	0.048	0.030	0.017	0.062	0.74	0.014	0	0	0.002		
Simpl. NLR	0	0	0	0	0	0	0	0.002	0	0	
Simpl. NLR + delay	0	0	0	0	0	0	0	0	0	0	0.67

Because the steady state time for Patlak analysis was defined as the TTP plus 3.5× the standard deviation of the first pass bolus, on average 9 acquisitions were included for Patlak analysis.

Fig. 3.10, and Table 3.2 together with Table 3.3 show that the K^{trans} values that are estimated using the NLR methods with irreversible leakage ($V_e = \infty$) were significantly more reliable than the Patlak methods. The introduction of reversible leakage, as in the AATH method and NLR+V_e, more than doubled the width of the CI of the estimation. The difference in reliability between the full and simplified NLR methods was found to be very small.

Fig. 3.10: Confidence intervals. The mean 95% confidence interval of K^{trans} of each method; more reliable estimates have narrower confidence intervals.
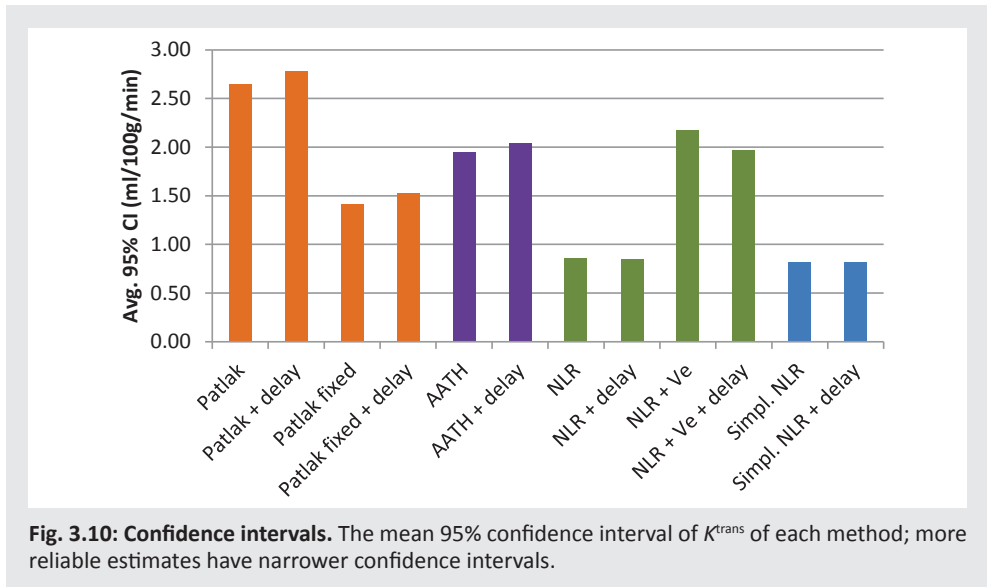
Fig. 3.10 also shows that fixating the CBV significantly improved the reliability of the Patlak estimates.

The delay correction had a minor effect on the CIs. With p-values higher than 0.001, the CIs of the standard Patlak, AATH, NLR, NLR+V_e, and simplified NLR methods were not significantly different from the delay corrected versions. The delay corrected CBV-fixed Patlak method performed slightly but significantly worse than its delay-sensitive version ($p < 0.001$).

Also the MTT distribution parameter a had a minor effect. The CI of the NLR+V_e method ($a = 0.632$) was not significantly different from the interval of the AATH method ($a = 1$). The CIs of the simplified NLR and simplified NLR+delay methods ($a = 1$) were slightly but significantly smaller than respectively the NLR and NLR+delay methods ($a = 0.632$).

Fig. 3.11: Computation times. The mean computation per slice (512 × 512 pixels) for each of the methods on a low-end desktop computer. Note that the *y*-axis is logarithmic. The Patlak methods that are extended with delay and/or fixed CBV require input from the gamma variate fit-based method.

Fig. 3.11 gives an overview of the average computation time for each method. It is not surprising that the simplest method, standard Patlak, was the faste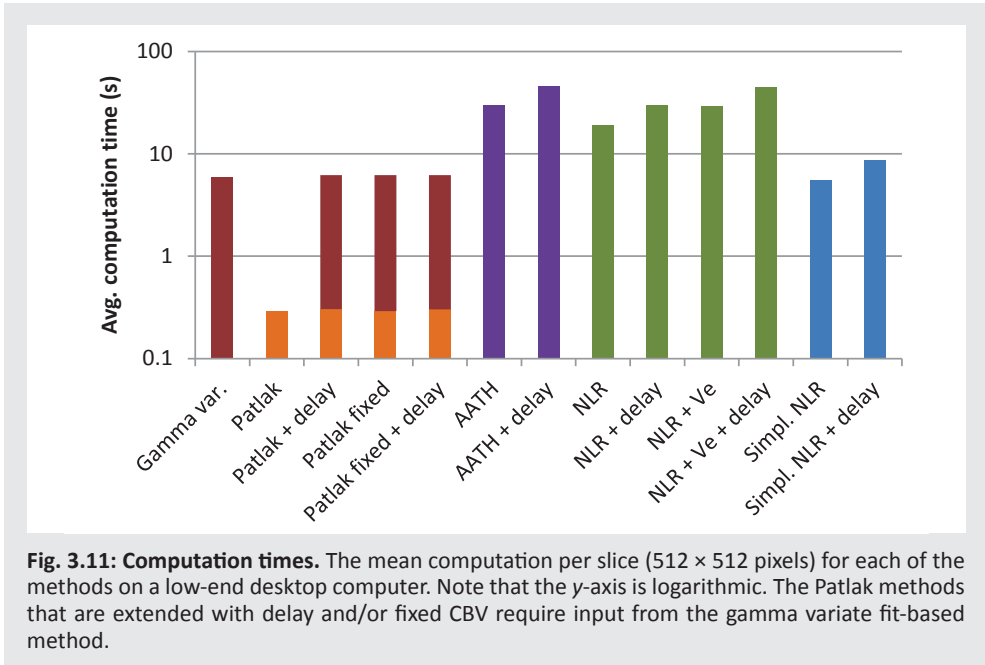st with 0.3 s per slice (512 × 512 pixels and 31 acquisitions). The other Patlak methods require additional input provided by a gamma variate fit, extending the computation time to 5.9 s per slice. The simplified NLR methods had computation times of respectively 5 and 9 s per slice, where the other NLR methods required between 19 and 45 s.

3.4 DISCUSSION

This study uses confidence intervals (CIs) to compare the reliability between different methods for estimating K^{trans} values. The 'reliability' can be thought of as a quantity that is inversely proportional to the width of these CIs. The experiments showed that the simplified NLR method has a CI that is a bit smaller than the full NLR methods, and significantly smaller than the Patlak methods in both the simulations and clinical measurements.

 'Reliability' is a non-scientific term that should be used with care. Some 'reliability metrics', like the Akaike information criterion, quantify the goodness of fit of a model.[3] For two reasons, however, this type of metric is not applicable to this study. First, the Patlak fits are applied to different (linearized) data than the non-linear fits, and therefore the goodness of fit between these methods may not be compared. Second, the reliability of

a single parameter, K^{trans}, is of importance, rather than the goodness of fit of the complete model. Not all time samples have an equal contribution to the estimated K^{trans}, and therefore the CI, which is specific to this parameter, is more appropriate.

A wider CI means a larger standard deviation in repeated measurements. For K^{trans} values close to zero, the probability distribution is skewed because the estimates are constrained to positive values, and therefore the mean will have a positive bias. This phenomenon is visible in Fig. 3.8a and c. The estimated CI, however, appears to be independent of the value for K^{trans}, which makes it a valid measure for evaluating the reliability of the methods, even if the true K^{trans} is close to zero. It has been demonstrated that the estimates from the clinical data are in line with the simulations, for which reason it can be concluded that the variation in average K^{trans} between the methods has to be addressed to a variation in the CIs rather than a bias in estimates.

The standard Patlak method was found to be two to three times less reliable than the NLR and simplified NLR method in both the simulated and clinical cases. However, fixating the CBV to a value estimated with a more sophisticated method, which is usually available anyway, roughly doubles its reliability. This means that fixating the CBV in the Patlak plot is a simple but very effective way to enhance reliability of the permeability estimates in general.

The standard Patlak method showed a decrease in reliability for long transit times. The performance of this method could in those cases probably be increased by determining the steady state of the tissue TAC instead of the AIF, as was done in this study. A longer MTT means that it takes more time for the capillary concentration to reach a steady state and therefore fewer samples should be included in the Patlak plot.

The addition of a delay time t_d as an extra parameter had a minor effect on the reliability of the K^{trans}. It has although been proven that delay-insensitive methods, i.e. methods that incorporate t_d, give better estimates for the CBV, CBF, and MTT.[78] Therefore, and because the CIs for the NLR methods did not increase despite the introduction of an extra free parameter, it can be concluded that t_d is an appropriate additional parameter for the NLR methods.

The shape of the MTT distribution, controlled by the parameter a in Eq. 3.10, is another feature that could improve the credibility of the IRF and therefore enhance the reliability of the K^{trans} estimates. The methods that use $a = 0.632$ instead of $a = 1$ have impulse response functions that are thought to be more realistic, but none of those methods showed a significant narrower CI on the clinical data, nor did the simulations show significant differences between these methods.[23] Although this parameter might increase the accuracy of other perfusion parameters, such as the CBF and MTT, it did not affect the estimation of K^{trans}.

The simulations showed that the AATH and NLR+V_e methods, both assuming reversible leakage, overestimate K^{trans} in case the leakage is virtually irreversible (Fig. 3.8c). This is most likely caused by the error in the estimated extravascular distribution volume, V_e (Eq.

3.7 and Eq. 3.10). In case V_e is underestimated, i.e. the model overestimated the washout from the extravascular space, then K^{trans} needs to be larger to compensate for the measured concentration levels. In theory, a V_e of nearly zero allows high K^{trans} values without noticeable leakage, because any leaked contrast is washed out instantly. The reliability of the AATH and NLR+V_e methods increases with larger K^{trans} values, in the order of 2 to 10 ml/100g/min, which can be explained by the fact that a higher permeability results in better V_e estimates. Therefore it cannot be concluded from our study that AATH and NLR+V_e perform worse than the other NLR methods in general. Models that account of reversible leakage are more applicable in pathologies with high vascular permeability, such as tumors, and in those particular cases they will likely give more reliable estimates.

On many points the NLR method provides a more sound theoretical basis than Patlak analysis for permeability analysis, and gamma variate fits or deconvolution for perfusion analysis.[78,152] First, the NLR method does not make any assumptions of the shape of the TACs themselves, but rather on the process that transforms the AIF into a tissue curve. The curves do not necessarily need to have a gamma variate-like profile, nor do they have to reach a steady state. A potential second pass bolus due to recirculation does not hamper the analysis. Second, at approximately the length of the MTT after the BAT, the permeability will start to affect the shape of the TAC measured in the tissue, including part of the first pass bolus. As opposed to the Patlak method, which uses only steady-state samples, the NLR methods include all acquired data. This means that no potentially useful information is wasted, and the results do not depend on the definition of the steady state. Third, because the NLR methods do not transform the TACs, the (approximate) normal distribution of the measurement errors is preserved, which fulfills the requirements for proper least squares fitting. In linearized regression using a Patlak plot this is no longer the case. Values are divided by $C_c(t)$, which is a non-linear operation that distorts the measurement errors. Fourth, all perfusion parameters, including permeability, are measured using a single method in which a change in one parameter affects all others. This reduces the bias in estimates that are influenced by other relevant factors that a method does not account of. For example, if the permeability is significant, then the intra-vascular blood volume can be biased if this is estimated by a method does not take leakage into the extra-vascular volume into account.

A disadvantage of NLR is that it is an iterative method, and so a straightforward implementation is time-consuming. This is most likely the reason why currently this technique is not much used in CTP analysis yet. The simplified NLR method, however, tackles two bottlenecks by omitting the need for convolutions and the calculation of exponentials, and is thereby at least four times faster than the full NLR methods. By further increasing the performance using e.g. parallel computing or GPU acceleration the analysis of high-resolution volumes in a clinical setting might be feasible.

3.5 CONCLUSIONS

The CI, and thereby the reliability, of the simplified NLR method is similar to the full NLR methods, and better than the Patlak methods in both the simulations and clinical measurements. The simplified NLR analysis just takes 5 s per 512 × 512 slice, making it suitable for time-critical clinical use. The simplified NLR method therefore seems to be a superior alternative to Patlak analysis. The next chapter evaluates the predictive value of the simplified NLR method for hemorrhagic transformation in acute ischemic stroke.

The techniques described in this study are applicable to other purposes as well, like tumor assessment using CTP or possibly using DCE-MR or PET, even though the SNR and kinetics might differ. For example, in a study performed by Oosterbroek et al. (2015) we found that model-based NLR analysis with a fixed transit time was preferable for delineation and characterization of laryngeal carcinoma imaged with CTP.[107]
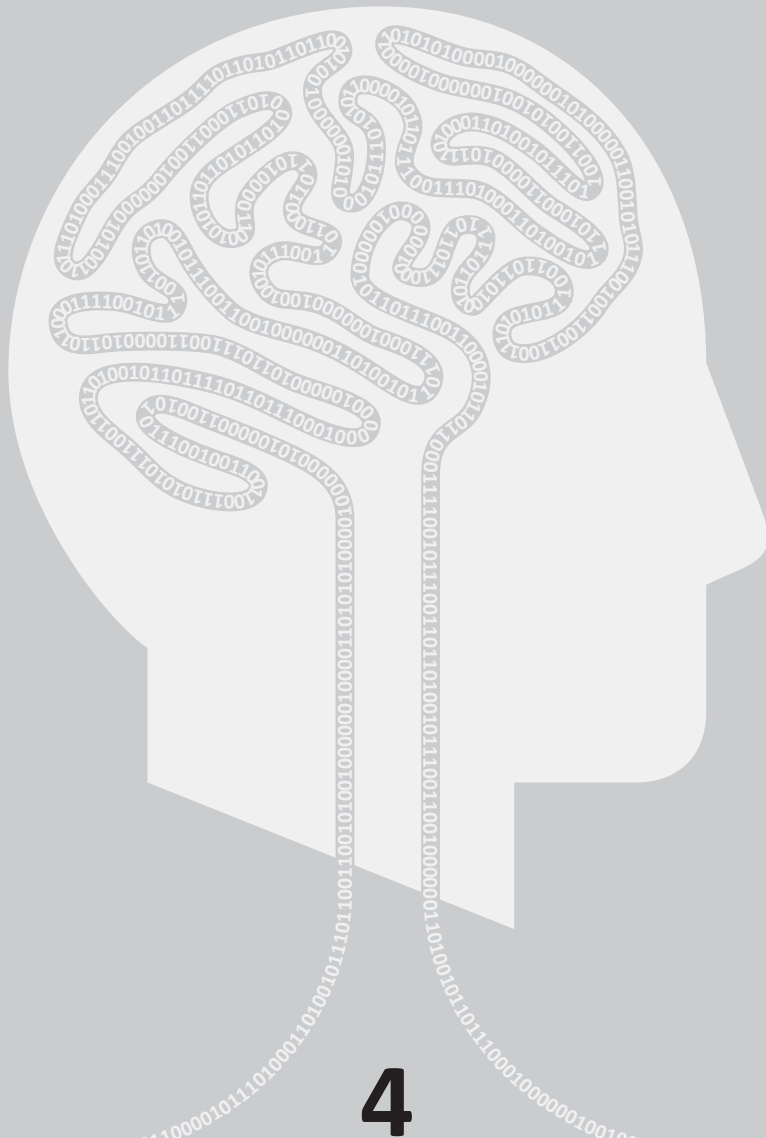
4

Prediction of Hemorrhagic Transformation

ABSTRACT

Intravenous thrombolysis can improve clinical outcome in acute ischemic stroke patients, but increases the risk of hemorrhagic transformation (HT). Blood-brain barrier damage, which can be quantified by the vascular permeability, is a potential predictor for HT. This study aimed to assess whether this prediction can be improved by measuring permeability using the novel fast model-based method as described in the previous chapter, instead of using Patlak analysis.

20 patients with HT on follow-up imaging and 40 patients without HT were selected. The permeability transfer constant K^{trans} was measured in three ways; using standard Patlak analysis, Patlak analysis with a fixed offset, and the simplified model-based non-linear regression (NLR) method. In addition, the permeability-surface area product (PS), cerebral blood volume, cerebral blood flow, and mean transit time were measured. Mann-Whitney U tests and receiver operating characteristic (ROC) analyses were performed to assess the discriminative power of each of the relative (ipsilateral versus contralateral) parameters.

The relative K^{trans} (rK^{trans}) values, measured with the model-based method, were significantly higher in the patients who developed HT as compared with those who did not. The rK^{trans} measured with standard Patlak analysis was not significantly different. The relative PS (rPS), measured with NLR, had the highest discriminative power ($p = 0.002$). ROC analysis of rPS showed an area under the curve (AUC) of 0.75 and a sensitivity of 0.75 at a specificity of 0.75. The AUCs of the Patlak rK^{trans}, the Patlak rK^{trans} with fixed offset and the NLR rK^{trans} were 0.58, 0.66, and 0.67, respectively.

CT perfusion analysis may aid in predicting HT, but standard Patlak analysis did not provide estimates for rK^{trans} that were significantly higher in the HT group. rPS, measured in the infarct core with NLR, had superior discriminative power compared with K^{trans} measured with either Patlak analysis with a fixed offset or NLR, and conventional perfusion parameters.

4.1 INTRODUCTION

Intravenous thrombolysis (IVT) can improve clinical outcome in acute ischemic stroke patients, but may increase the risk of developing symptomatic hemorrhagic transformation (HT) 2 to 5 times.[4,15,48,89,138] Blood-brain barrier (BBB) damage, which can be quantified by measuring vascular permeability, may be a predictor for HT in stroke.[18,33,88] CT perfusion (CTP) imaging could therefore potentially provide the means to predict the risk of developing HT with IVT treatment.

The previous chapter explained and compared methods for estimation of vascular permeability using CTP imaging. The Patlak analysis method is straightforward and fast, but its linearized regression has some inherent weaknesses compared to non-linear regression (NLR). Most important, only the steady-state samples (after the first-pass bolus) can be taken into account. In contrast, model-based analysis using NLR allows the analysis of entire enhancement curves, providing an integral method for measuring permeability along with the cerebral blood volume (CBV), flow (CBF), and mean transit time (MTT).

In the study described in the previous chapter it was found that the 95% confidence interval (CI) for the permeability transfer constant K^{trans} as estimated with standard Patlak analysis was three times larger compared to NLR analysis. Fixing the CBV in Patlak analysis to a value estimated with a gamma variate fit showed an improved 95% CI, but still inferior to NLR. Because NLR allows estimating the permeability transfer constant K^{trans} with a theoretically higher reliability, it is hypothesized that this method will also give estimates with a higher discriminative power than Patlak analysis.

The purpose of this study was to determine if the predictive value of permeability and perfusion parameters for HT development, measured using extended CTP imaging, can be improved by using the NLR method instead of Patlak analysis.

4.2 METHODS

4.2.1 Study Design

We selected the first 20 consecutive cases with HT on follow-up NCCT and 40 controls without HT on follow-up NCCT from the DUST study, of which the inclusion criteria and CTP acquisition protocol are described in Section 1.4. The consecutive series of patients was selected matching the following additional inclusion criteria: 0.625 to 1.25 mm thin slice reconstructed, extended (meaning 210 s duration) CTP acquisition on admission, and follow-up non-contrast CT imaging at three days or in case of clinical deterioration. HT was defined as the presence of any ECASS HT subtype.[15] All patients in the control group received IVT within a 4.5 hour window from time to onset. Inasmuch as infarct location was not a selection criterion, these locations were randomly distributed to their natural prevalence.

4.2.2 Preprocessing

Because moderate and severe head movement is common in CTP imaging of acute ischemic stroke patients, the time series of 0.625 to 1.25 mm thick slices were registered in 3D using a rigid registration algorithm (Elastix).[39,67] After registration adjacent axial slices were averaged to obtain 8 to 13 contiguous slabs of 5 mm per volume, which is common practice for clinical evaluation, mainly to limit the noise and processing time.

The registered 3D volumes were visually inspected for artifacts; these are mostly streak artifacts caused by motion during acquisition. Poor acquisitions were removed from the data.

Next, a temporal Gaussian filter with a SD of 4 s, followed by a 3D bilateral filter (TIPS) with a spatial SD (σ_d) of 4 mm and a profile-similarity SD (σ_ξ) of 50 HU^2 were applied to further reduce the noise.[91] These settings correspond to what was used in the study described in the previous chapter, and result in perfusion maps with a visually well-balanced resolution and noise level.

A gamma variate curve was fitted to the arterial input function (AIF) to estimate its area under the curve (AUC), time-to-peak (TTP), the arterial bolus arrival time (BAT), and the onset of the steady state (See Fig. 3.6b in the previous chapter). The average arterial BAT, i.e. the time between the start of the scan and the first appearance of contrast enhancement in the cerebral arteries, of the 60 scans was 6.9 s.

4.2.3 Estimating Permeability and Perfusion Parameters

Ischemia due to stroke may alter BBB integrity, allowing the diffusion of blood and contrast molecules into the extravascular space. This is explained in more detail in Section 1.3.2. Unknown at the time of measurement, this leakage may either be in the permeability-limited domain or in the flow-limited domain. In the first case the outflow to the extravascular space as measured by K^{trans} will not increase when the flow increases, whereas in the latter case it will increase linearly with the flow. In either case, a patient with BBB damage is likely to show increased K^{trans} values.

K^{trans} was measured in three ways. First, using standard linear Patlak analysis,[109,110] second, using Patlak analysis with an offset that is fixed to a blood volume that was estimated by an independent method as described by Schneider et al. (2011),[128] and third, using the simplified NLR method as described in Chapter 3.[14] Only the NLR method is capable of estimating CBF, and therefore of calculating the permeability-surface area (PS) by inverting the Renkin-Crone equation:[31,117]

$$K^{trans} = \text{CBF}\left(1 - e^{-\text{PS/CBF}}\right), \text{ thus}$$
$$\text{PS} = -\text{CBF}\left(\log\left(1 - K^{trans}/\text{CBF}\right)\right)$$

Eq. 4.1

If the leakage is in the permeability-limited regime, i.e. K^{trans} << CBF, then the leakage does not increase with increasing CBF, and K^{trans} is equal to PS:

$$\lim_{K^{trans}/CBF \to 0} PS = K^{trans}$$

Eq. 4.2

The study described in Chapter 3 showed that model-based NLR analysis resulted in unbiased estimates of K^{trans} under low-noise conditions. Under realistic noise conditions, both the NLR and Patlak methods showed a small positive bias for small K^{trans} values (see Fig. 3.8a). It was furthermore found that the K^{trans} values measured by the simplified method were not affected by MTT, and that more complex models did not provide more reliable estimations of K^{trans} in stroke patients. NLR confidence intervals were 3× smaller than standard Patlak analysis and more than 1.5× smaller than Patlak analysis with fixed offset.

4.2.4 Postprocessing

The contrast-free acquisitions (before the bolus arrival time) were averaged to obtain a NCCT image. Only the voxels that had a CT value >17 HU or <55 HU on this NCCT were classified as brain tissue and included in the analysis. Voxels with a blood volume >9 ml/100g were classified as vessels and excluded from the analysis. A correction factor $(1 - Ht_{large})/(1 - Ht_{small})$ was applied to correct the tracer concentration for the difference between in hematocrit (see Eq. 1.1 in Section 1.3.1).[71] The values used for Ht_{large} and Ht_{small} are respectively 0.45 and 0.25.[116]

4.2.5 Statistical Analysis

All parameters were estimated in each of the voxels that were classified as brain tissue on the NCCT. Infarct cores were defined as all brain tissue voxels on the ipsi-lateral side having a CBV less than 2 ml/100g, as suggested by Wintermark et al. (2006).[147] The measured parameters were averaged in the infarct core as well as in the brain tissue in both entire hemispheres. Next, relative values averages were obtained in two ways. First, by dividing the average in the infarct core by the average in the entire contra-lateral hemisphere. Second, by dividing the average in the entire ipsi-lateral hemisphere by the average in the entire contra-lateral hemisphere. A symmetry plane was manually aligned to the midsagittal plane in order to separate the hemispheres.

Pearson correlation coefficients and linear fits were calculated to quantify the relation between the three different measurements for K^{trans}. Wilcoxon signed rank tests were applied to check if the relative parameters (rK^{trans}, rPS, rCBV, rCBF, and rMTT) were significantly different between the hemispheres. To identify the parameters that were significantly different between the HT- and control group, a Mann-Whitney U test was applied. Results were considered significant for $p < 0.05$. Receiver operating characteristic (ROC) curves

were used to assess the discriminating power of those parameters that were found to be significantly different.

4.3 RESULTS

Demographic and clinical data of the selected patients are summarized in Table 4.1. There was no significant differences in age, sex, prior stroke, baseline NIHSS score, time to arrival, or time to imaging between the HT and control group. The medians of the infarct core and penumbra sizes (total area of the cross-sections at both ASPECTS levels)[112] were higher in the HT group, but not significantly different.

Table 4.1. Baseline clinical and imaging characteristics. HT, hemorrhagic transformation; IAT, intra-arterial thrombolysis; IVT, intravenous thrombolysis; MT, mechanical thrombectomy.

	All patients *N* = 60	Control group *N* = 40 (67 %)	HT group *N* = 20 (33 %)	*p*-value
Clinical parameters				
Age, mean (SD)	69 (13)	67 (13)	73 (12)	0.07
Female sex, *N* (%)	24 (40)	18 (45)	6 (30)	0.27
Prior stroke, *N* (%)	10 (17)	6 (15)	4 (20)	0.63
Baseline NIHSS, mean (SD)	11 (6)	11 (5)	12 (7)	0.40
Time to arrival, minutes, median (IQR)	65 (47, 121)	73 (37, 120)	62 (50, 133)	0.94
CT perfusion imaging				
Size infarct core*, mm², median (IQR)	458 (75, 1695)	290 (58, 1204)	1161 (179, 3002)	0.12
Size penumbra area*, mm², median (IQR)	1938 (627, 3819)	1938 (713, 2895)	2835 (316, 5119)	0.38
Time to imaging, minutes, median (IQR)	98 (69, 145)	98 (66-145)	96 (72, 153)	0.65
Treatment				
IVT, *N* (%)	55 (92)	40 (100)	15 (75)	0.001
IAT or MT, *N* (%)	4 (7)	3 (8)	1 (5)	0.73
Time to treatment†, minutes, median (IQR)	113 (80, 165)	115 (78, 165)	110 (87, 167)	0.94

* Total area of the infarct core and penumbra cross-sections at both ASPECTS levels.[112]
† For 54 patients (5 did not receive IVT, and missing value in 1 HT patient).

Visual inspection revealed that some of the patients (20%) showed ring-shaped scanner artifacts in their permeability maps (K^{trans} and PS), with the worst case shown in the bottom row in Fig. 4.1. These distortions were just slightly visible on the filtered CTP data and on the other perfusion maps (CBV, CBF, and MTT) generated by the NLR method.

Fig. 4.1: Permeability maps. A filtered CT perfusion slice (acquisitions at the time-to-peak of the arterial input function), the NLR blood volume (CBV) map, the three K^{trans} maps, and the NLR permeability-surface area (PS) map of two patients in the HT group. The CBV maps both show a clearly visible infarct core in the middle cerebral artery territory in the left hemisphere. The standard Patlak maps (third column) appear noisier than the CBV fixed and NLR K^{trans} maps. The K^{trans} and PS maps in the top row show elevated permeability in the entire ipsi-lateral hemisphere and a permeability 'hot spot' medial to the infarct core (indicated by the arrows). The maps in the bottom row are affected by ring-shaped scanner artifacts (worst case shown).
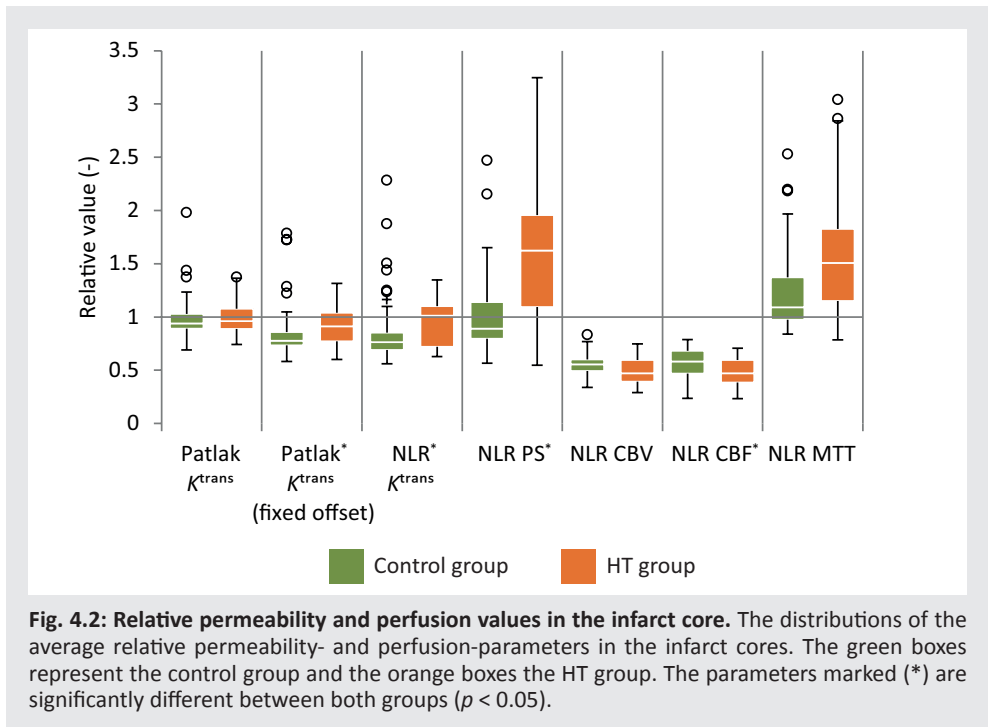
The hemisphere-averages of all estimated parameters, except for the CBV, were found to be significantly different between the ipsi-lateral and contra-lateral sides ($p < 0.05$) in both the HT group and the control group.

Table 4.2, Fig. 4.2, and Fig. 4.3 show the relative parameters and their *p*-values. All three methods addressed in this study, i.e. Patlak, Patlak with fixed offset, and NLR, provide estimates for the permeability transfer constant K^{trans}. However, only the Patlak method with fixed offset and the NLR method gave estimates for relative K^{trans} (rK^{trans}) that were significantly higher in the patients who developed HT ($p = 0.04$ and $p = 0.03$ for the infarct cores). The values for Patlak K^{trans} with fixed offset showed a strong correlation with the NLR K^{trans} values, which is emphasized by the K^{trans} maps in Fig. 4.1. The Pearson coefficient between the average K^{trans} values observed in the infarct core between these methods was 0.99, and the slope of a linear fit through the origin was 1.02. The standard Patlak K^{trans} showed a weaker correlation with NLR K^{trans}, with a Pearson coefficient of 0.83 and a slope of 2.05.

Table 4.2: Relative permeability and perfusion parameters. The median (interquartile range) and *p*-value (Mann-Whitney *U* test) of each relative perfusion parameter (*p* < 0.05) in the infarct cores (CBV < 2 ml/100g) and in the whole ipsi-lateral hemispheres.

Parameter	Infarct core relative to whole contralateral hemisphere			Whole ipsilateral hemisphere relative to whole contralateral hemisphere		
	HT (N=20)	Control (N=40)	*p*-value	HT (N=20)	Control (N=40)	*p*-value
Patlak rK^{trans}	0.95 (0.19)	0.93 (0.12)	0.30	1.03 (0.25)	1.04 (0.14)	0.83
Patlak rK^{trans} (fixed offset)	0.91 (0.30)	0.78 (0.13)	0.04*	1.22 (0.33)	1.03 (0.12)	0.11
NLR rK^{trans}	1.02 (0.42)	0.76 (0.17)	0.03*	1.28 (0.46)	1.07 (0.18)	0.04*
NLR rPS	1.70 (1.06)	0.89 (0.35)	0.002*	1.66 (0.86)	1.11 (0.77)	0.005*
NLR rCBV	0.45 (0.20)	0.55 (0.11)	0.10	0.99 (0.13)	1.00 (0.07)	0.26
NLR rCBF	0.47 (0.23)	0.58 (0.21)	0.04*	0.78 (0.25)	0.90 (0.14)	0.05*
NLR rMTT	1.51 (0.69)	1.09 (0.42)	0.09	1.72 (0.90)	1.25 (0.37)	0.03*

* Significant, i.e. *p* < 0.05.

Fig. 4.2: Relative permeability and perfusion values in the infarct core. The distributions of the average relative permeability- and perfusion-parameters in the infarct cores. The green boxes represent the control group and the orange boxes the HT group. The parameters marked (*) are significantly different between both groups (*p* < 0.05).

Fig. 4.3: Relative permeability and perfusion values in the whole hemisphere. The distributions of the average relative permeability- and perfusion-parameters in the whole ipsi-lateral hemispheres. The green boxes represent the control group and the orange boxes the HT group. The parameters marked (*) are significantly different between both groups ($p < 0.05$).

The relative permeability-surface area product (rPS) had the highest discriminative power. This parameter had both the lowest *p*-value in the Mann-Whitney *U* test ($p = 0.002$ for the infarct cores) and the highest area under its ROC curve (0.75, 95% CI: 0.62 to 0.89, Table 4.3 and Fig. 4.4). The rPS had a sensitivity of 0.75 at a specificity of 0.75 (threshold at rPS = 1.12), and a sensitivity of 0.50 at a specificity of 0.88 (threshold at rPS = 1.70).

The parameters, except for rMTT, had slightly better discriminative power when measured in the infarct core than when measured in the whole ipsi-lateral hemisphere.

Table 4.3: Discriminative power of the permeability- and perfusion-parameters. The area under the curve (AUC) with 95% CI and *p*-value (asymptotic significance; *p* < 0.05) of the receiver operating characteristic (ROC) curves of all parameters. The curves for the parameters with significant discriminating value are shown in Fig. 4.4.

| Parameter	Infarct core vs whole contralateral hemisphere		Whole ipsilateral hemisphere vs whole contralateral hemisphere	
	AUC (95% CI)	*p*-value	AUC (95% CI)	*p*-value
Patlak rK^{trans}	0.58 (0.43, 0.74)	0.29	0.52 (0.35, 0.69)	0.83
Patlak rK^{trans} (fixed offset)	0.66 (0.51, 0.81)	0.04*	0.63 (0.46, 0.80)	0.11
NLR rK^{trans}	0.67 (0.52, 0.82)	0.03*	0.67 (0.51, 0.82)	0.04*
NLR rPS	0.75 (0.62, 0.89)	0.001*	0.73 (0.58, 0.88)	0.005*
NLR CBV	0.63 (0.47, 0.80)	0.10	0.59 (0.43, 0.75)	0.26
NLR rCBF	0.67 (0.52, 0.81)	0.04*	0.66 (0.50, 0.82)	0.05*
NLR rMTT	0.64 (0.48, 0.80)	0.09	0.68 (0.52, 0.83)	0.03*

* Significant, i.e. *p* < 0.05.
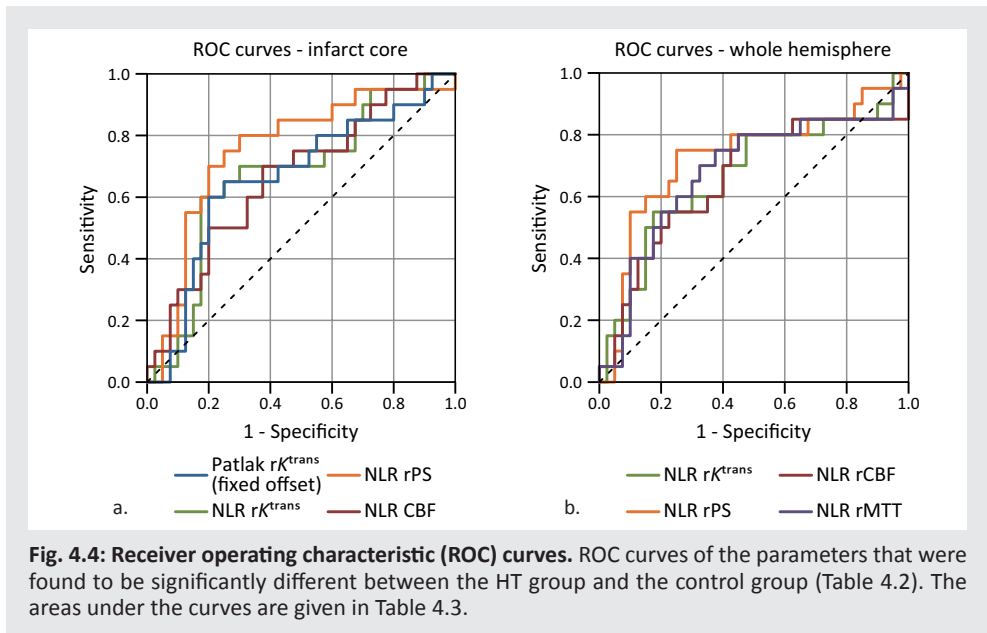
Fig. 4.4: Receiver operating characteristic (ROC) curves. ROC curves of the parameters that were found to be significantly different between the HT group and the control group (Table 4.2). The areas under the curves are given in Table 4.3.

In addition, the relative CBF (rCBF) was significantly lower in the HT group (*p* = 0.04 for the infarct cores). The relative MTT (rMTT) was significantly higher in the HT group, but only when measured in the entire hemisphere (*p* = 0.03). No significant differences in relative CBV (rCBV) between the groups were observed.

For none of the observed parameters significant differences were found between the subgroup of patients that developed HT and received IVT and the subgroup that developed HT but did not receive IVT. The rK^{trans} and rPS parameters were on average lower in the subgroup that did not receive IVT treatment.

4.4 DISCUSSION

Non-linear regression enables simultaneous measurement of permeability along with CBV, CBF, and MTT. Whereas the frequently used Patlak method only takes the steady-state samples (after the first-pass bolus) into account, NLR allows the analysis of the entire TACs. In Chapter 3 it was shown that this feature resulted in smaller 95% CIs for the permeability estimates. This study emphasizes the use of NLR over Patlak analysis, because it also provides better predictors for developing HT.

The parameter rK^{trans} estimated with fixed-offset Patlak analysis showed improved discriminating power compared with standard Patlak analysis. This corresponds to the finding in Chapter 3 that fixing the CBV halved the width of the 95% CI. This improvement can be explained by the fact that when the CBV is fixed to a value estimated by gamma-variate curve fitting, the information in the entire TAC is used instead of the steady state only. The finding that the average absolute Patlak K^{trans} estimates were twice as high as the values measured with NLR and Patlak with fixed offset was also in line with the previous study, and can be explained by the fact that noise gives a positive bias to K^{trans} estimates.

The discriminating power of the best predictor, rPS measured using NLR, although significant, is still on the low side with an area under the ROC curve of 0.75 (95% CI: 0.62 to 0.89) when measured in the infarct core. Furthermore, the 95% CIs on the AUCs are rather large due to the small population size. However, since multiple parameters showed significant discriminating power, multivariate analysis may result in a larger AUC. The additional value in predicting HT, compared to all perfusion parameters as well as clinical and demographic data, needs to be assessed by multivariate analysis in a larger stroke cohort.

The average infarct core size, as measured on admission CTP, was larger in the HT group, although not significantly. One may expect that the chance of developing HT increases with infarct size. However, this study showed that the average permeability values, measured in the infarct core, are better predictors for HT than the infarct core size.

A limitation of the study is that not all patients that developed HT received IVT treatment. We did not require IVT treatment for the patients in the HT group because those patients who showed HT on the follow-up scan without receiving treatment, would most probably also have developed HT if they did receive IVT treatment. In case IVT would be required for both groups, this would reduce the number of patients in the HT group. Since IVT is thought

to increase the probability of developing HT, the five patients that did not receive IVT treatment in the HT group might have had higher permeability values and therefore might have increased the discrimination between the HT group and the non-HT group. However, this did not occur because for none of the observed parameters a significant difference between these subgroups was found, and the permeability values were on average even lower in the subgroup that did not receive IVT treatment.

Another limitation is that around 20% of the permeability maps showed ring-shaped scanner artifacts. These artifacts are positioned in the isocenter of the gantry and are the result of sub-optimal detector calibration.[11] Due to small differences in calibration, the CT-values in the images may have a variable offset and gain depending on the distance to the isocenter. This effect is especially dominant at low tube currents as used in CTP. When the acquired volumes in a CTP scan are each rotated or translated to correct for patient motion, the displacement of these rings will introduce noise in the CT-values in the temporal dimension, to which the permeability maps are sensitive.

Furthermore, the data could be improved by enhancing the detector calibration and the use of a more sophisticated, iterative reconstruction technique. These improvements could increase the signal to noise ratio and reduce artifacts without increasing the radiation dose or reducing the resolution.

In contrast to many other studies that investigated BBB permeability in stroke,[5,9,51,65,66,82] the baseline NIHSS scores in between the HT- and control group were not significantly different in this population. This could be explained by the shorter median time from stroke onset to treatment (111 min versus 120 to 311 min for other studies).[5,33,34,54,55,128] The fact that the clinical parameters between the groups in this study were similar endorses the presented results.

4.5 CONCLUSIONS

Concluding, the NLR method provides estimates for permeability parameters that are promising for predicting HT. The predictor rPS, measured in the infarct core, showed the highest discriminative power, while rK^{trans}, rCBF, and rMTT measured with NLR were also significantly stronger in the HT group than in the control group. This finding confirms the hypothesis that including the information in all data points of the TACs is an important advantage of NLR over linearized regression. HT prediction using NLR might become a valuable addition to the existing CT stroke protocol in patients with acute ischemic stroke.

5

Influence of Thin Slice CTP Reconstruction

ABSTRACT

Although CT scanners generally allow dynamic acquisition of thin slices (1 mm), thick slice (≥5 mm) reconstruction is commonly used for stroke imaging to reduce data, processing time, and noise level. Thin slice CT perfusion (CTP) reconstruction may suffer less from partial volume effects, and thus yield more accurate quantitative results with increased resolution. Therefore it may be more sensitive in the detection of small lesions. Before thin slice protocols are to be introduced clinically, it needs to be ensured that this does not affect overall CTP constancy. We studied the influence of thin slice reconstruction on average perfusion values by comparing it with standard thick slice reconstruction.

From 50 patient studies, absolute and relative hemisphere averaged estimates of cerebral blood volume (CBV), cerebral blood flow (CBF), mean transit time (MTT), and permeability-surface area product (PS) were analyzed using 0.8, 2.4, 4.8, and 9.6 mm slice reconstructions. Specifically, the influence of Gaussian and bilateral filtering, the arterial input function (AIF), and motion correction on the perfusion values was investigated.

Bilateral filtering gave noise levels comparable to isotropic Gaussian filtering, with less partial volume effects. Absolute CBF, CBV and PS were 22%, 14% and 46% lower with 0.8 mm than with 4.8 mm slices. If the AIF and motion correction were based on thin slices prior to reconstruction of thicker slices, these differences reduced to 3%, 4% and 3%. The effect of slice thickness on relative values was very small.

This study shows that thin slice reconstruction for CTP with unaltered acquisition protocol gives relative perfusion values without clinically relevant bias. It does however affect absolute perfusion values, of which CBF and CBV are most sensitive. Partial volume effects in large arteries and veins lead to overestimation of these values. The effects of reconstruction slice thickness should be taken into account when absolute perfusion values are used for clinical decision making.

5.1 INTRODUCTION

Modern multi-detector row CT scanners typically have a focal spot size of about 1 mm, an in-plane voxel size of about 0.5 mm × 0.5 mm, and a minimal slice thickness between 0.5 and 1 mm. In clinical practice, however, the CTP brain scans are acquired in thin slices but reconstructed into thicker slices of approximately 5 or 10 mm to suppress noise and to reduce the amount of data and processing time. For this reason thick slice data are generally used to classify infarct core and penumbra. To our knowledge, all studies that have presented absolute, relative, or multi-variate thresholds on the perfusion parameters for the classification of these areas used a slice thickness of 5 mm or more, resulting in anisotropic voxel dimensions.[20,21,28,63,64,68,99,100,127,147,150]

Because of ongoing developments in computer performance, it may now be feasible to exploit thin slice CTP brain data with smaller, less anisotropic voxels, which could have substantial benefits in clinical stroke assessment.

First, a slice thickness of 1.8 mm and smaller permits the selection of a partial volume free arterial input function (AIF) in the middle cerebral artery, thus avoiding the necessity for selecting a venous output function (VOF) to correct for partial volume effects (PVE).[118] It is hypothesized that a significant proportion of the variability found between observers and between analysis platforms in absolute quantification of perfusion values[40,42,64] may be due to the selection of partial volume affected arteries and veins.

Second, because the voxels in thin slice scans are near isotropic, it can be considered a true 3D volume instead of a series of 2D slices. This enables true 3D motion correction as well as sagittal, coronal, and oblique reformatting of perfusion maps.
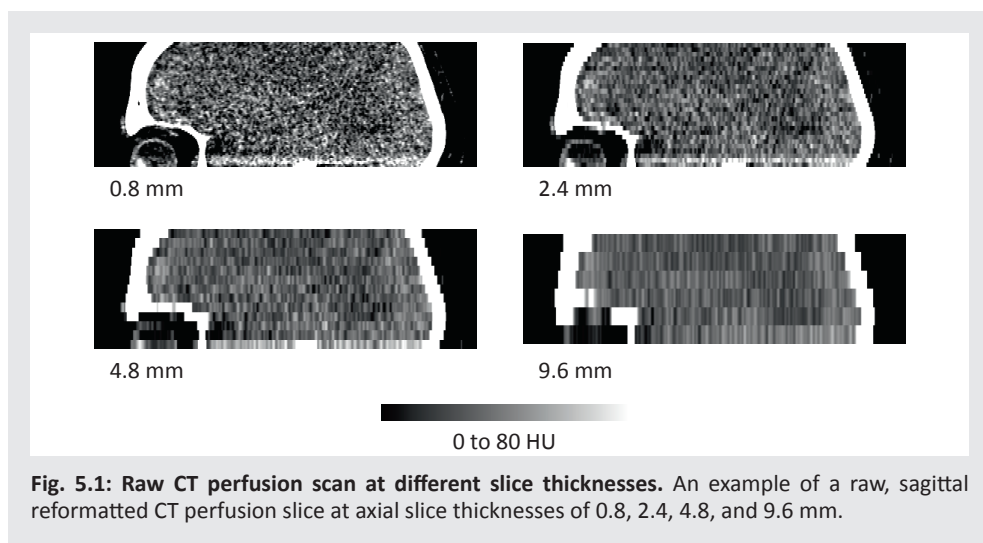
Third, it has been suggested that the detectability of lacunar strokes may improve with increased spatial resolution.[146] This type of infarct, generally considered smaller than 15 to 20 mm, accounts for 25% of all ischemic strokes.[121]

Since modern scanners, computers, and filtering techniques make CTP analysis with high axial resolution feasible, the clinical application of thin slice reconstruction is expected to increase in the near future. Whereas it is known that PVE due to thick slice reconstruction results in overestimation of CBV and CBF,[125] the extent of using full axial resolution on perfusion values and outcomes is as yet unclear.

Accordingly, the aim of this study was to assess the consequences of changing the slice thickness of CTP reconstruction on the perfusion parameters measured with CTP brain analysis.

5.2 METHODS

High-resolution CTP scans from 50 acute stroke patients, with an acquired axial resolution of 0.8 mm, were used to create data with slice thicknesses of 2.4, 4.8, and 9.6 mm. An example of a raw sagittal CTP slice at these four thicknesses is shown in Fig. 5.1. To test how the observed perfusion parameters relate to the slice thickness, and how AIF resolution and motion correction affect these measurements, four different processing schemes were applied (Table 5.1). This resulted in 16 sets of perfusion parameter maps of which 14 are unique; the 0.8 mm resolution variations on scheme 2, 3, and 4 are the same because all schemes have a 0.8 mm AIF and thin-slice motion correction at the highest resolution.

0.8 mm

2.4 mm

4.8 mm

9.6 mm

0 to 80 HU

Fig. 5.1: Raw CT perfusion scan at different slice thicknesses. An example of a raw, sagittal reformatted CT perfusion slice at axial slice thicknesses of 0.8, 2.4, 4.8, and 9.6 mm.

Because the thin slice reconstructions will only be clinically acceptable if radiation dose and image noise levels do not increase, the noise level was equalized over all reconstructions by using a bilateral filter with slice thickness specific parameters [137].

Table 5.1. Slice thicknesses and filter types. In scheme 1 to 3 motion correction is performed on thin slices, after which thick slices are generated. In scheme 4 motion correction is performed on thick slices.

Scheme no.	Motion correction thickness (mm)	Filtering and analysis slice thickness (mm)	Filter type	AIF and VOF slice thickness (mm)
1	0.8	0.8	Gaussian	0.8
	0.8	2.4	Gaussian	2.4
	0.8	4.8	Gaussian	4.8
	0.8	9.6	Gaussian	9.6
2	0.8	0.8	Bilateral	0.8
	0.8	2.4	Bilateral	2.4
	0.8	4.8	Bilateral	4.8
	0.8	9.6	Bilateral	9.6
3	0.8	0.8	Bilateral	0.8
	0.8	2.4	Bilateral	0.8
	0.8	4.8	Bilateral	0.8
	0.8	9.6	Bilateral	0.8
4	0.8	0.8	Bilateral	0.8
	2.4	2.4	Bilateral	2.4
	4.8	4.8	Bilateral	4.8
	9.6	9.6	Bilateral	9.6

5.2.1 Study Design

CTP scans of 50 consecutive acute ischemic stroke patients were included retrospectively from a single center (University Medical Center Utrecht) participating in the Dutch acute stroke study (DUST). The inclusion criteria and the CTP acquisition protocol are described in Section 1.4.

All included scans were acquired on a Philips Brilliance iCT scanner (Philips Healthcare, Best, the Netherlands) at 80 kVp and 150 mAs. These scans had an axial coverage of 65 mm at most and a field-of-view of approximately 200 mm × 200 mm. All scans had a total acquisition time of 210 s and were reconstructed into thin slices (0.8 mm), resulting in 65 to 81 reconstructed slices per 3D volume.

Since infarct size and location were not selection criteria, these were randomly distributed to their natural prevalence.

5.2.2 Preprocessing

Automated rigid 3D motion correction was done using the open source registration toolbox Elastix.[67] The skull served as a reference for registering all acquired volumes to the first. One major disadvantage of thin slice data is the increased noise level due to the increased number of voxels in the image volume. The variance of the noise will be roughly doubled when the slice thickness is halved, until it reaches the size of the point spread function of

the scanner. In order to reduce the noise to an acceptable level for analysis, a filter kernel with a large enough volume is required for averaging. Although a large standard isotropic Gaussian filter can perform this task, it would introduce PVE that would nullify the resolution gained by the thinner slices. An anisotropic bilateral filter, however, is able to adapt its shape to its neighborhood and therefore average the same number of voxels with reduced PVE, whenever the neighborhood allows it (see Section 2.2.5).[137] In order to compare the effects of bilateral filtering to isotropic Gaussian filtering, both filters were applied (Table 5.1).

The objective of this study was to compare perfusion parameters at different slice thicknesses but at equal noise level and dose. To this end, both the isotropic Gaussian and the anisotropic bilateral filter were adjusted for each thickness such that the SD of the noise in the filtered images, SD_{out}, was reduced to a constant level of approximately 0.75 Hounsfield units (HU). For the isotropic Gaussian kernel $g(\xi,\mathbf{x})$ (see Eq. 2.5 in Section 2.2.5) this was achieved by using a σ_d of 2.5 mm for all slice thicknesses. A fixed σ_d of 3.0 mm was used for the bilateral kernel $b(\xi,\mathbf{x})$ (see Eq. 2.5 in Section 2.2.5); keeping σ_d fixed means that σ_r had to be scaled along with the slice thickness. The scaling factor $\sigma_r = 3.34 SD_{in}$ resulted in SD_{out} values of approximately 0.75. SD_{in} and SD_{out} were estimated by taking the median SD on the values in the attenuation curves within the brain tissue before the arterial bolus arrival time. The mean bolus arrival time of the data was 10.7 s (SD = 3.0 s). The filter settings and measured SD_{in} and SD_{out} values are listed in Table 5.2.

Table 5.2. Filter settings. The standard deviations σ_d and σ_r of the filter kernels, and the median noise levels of the unfiltered and filtered data, SD_{in} and SD_{out}, at each slice thickness. The number between brackets is the width of the interquartile range (IQR).

Thickness (mm)	Unfiltered	Isotropic Gaussian filter		Anisotropic bilateral filter		
	SD_{in} (HU) median (IQR)	σ_d (mm)	SD_{out} (HU) median (IQR)	σ_d (mm)	σ_r (HU²)	SD_{out} (HU) median (IQR)
0.8	14.9 (2.95)	2.5	0.76 (0.16)	3.0	50.0	0.74 (0.16)
2.4	11.1 (1.94)	2.5	0.75 (0.15)	3.0	37.3	0.75 (0.17)
4.8	8.4 (1.37)	2.5	0.77 (0.15)	3.0	28.1	0.76 (0.18)
9.6	6.1 (0.99)	2.5	0.70 (0.15)	3.0	20.5	0.74 (0.18)

5.2.3 Perfusion Analysis

AIFs were selected semi-automatically by searching within a manually defined circular region of interest (ROI) with a 2 cm radius for the voxel with the highest area under the curve (AUC), in keeping with the clinical standard procedure. The ROI was drawn on a 9.6 mm slice of the bilaterally filtered data, and the same ROI was applied to the 0.8, 2.4, 4.8 mm slices. Whenever possible an internal carotid artery was chosen to provide the AIF. If this location happened to be outside the imaged volume, a middle cerebral artery was chosen.

Because the axial resolution can be rather coarse with respect to the diameter of the arteries providing the AIF, the AUC of the AIF might be underestimated owing to partial volume effects. Because this leads to an overestimation of CBV, CBF, and PS, correction for partial volume is often necessary, at least in thick slice reconstructions.[6,118] The correction was provided by always selecting a VOF in the superior sagittal sinus or transverse sinus near the torcular herophili, using the same method and at the same slice thickness as the AIF, as described above.

A fast model-based non-linear regression (NLR) method was used to calculate the perfusion maps. In Chapters 3 and 4 it was shown that this NLR method not only provides the standard perfusion parameters CBV, CBF, and MTT, but also an estimate for PS, while the method is in addition insensitive to tracer delay and can be computed fast enough for application in an acute clinical setting.

The acquisitions before bolus arrival were averaged to obtain a non-contrast CT image. This non-contrast image provides the offsets for the tissue attenuation curves and it is used to segment the brain tissue. Only the voxels that had a non-contrast CT value >17 HU and <55 HU were classified as brain tissue and included in the analysis. Voxels with a blood volume >9 ml/100g were classified as vessels and excluded from the analysis. A correction factor was applied to correct the tracer concentration for the difference between the hematocrit in large vessels (AIF) and small vessels (capillaries).[71,116]

Symmetry lines were drawn manually to separate the hemispheres. The mean values of the perfusion parameters (CBV, CBF, MTT, and PS) were calculated in each hemisphere. Relative values for CBV (rCBV), CBF (rCBF), and PS (rPS) were calculated by dividing the ipsilateral means by the contralateral means, because these values are affected by scaling of the AIF. The relative MTT was not calculated as ratio, but rather as the difference in MTT (dMTT) by subtracting the contralateral mean from the ipsilateral mean, because the MTT itself is derived from the difference in width between the AIF and the tissue curves. Unlike CBV, CBF, and PS, the MTT parameter is not affected by scaling of the attenuation curves.

5.2.4 Statistical Analysis

Although the noise levels of the perfusion maps were expected to be independent of the slice thickness because the noise in the filtered perfusion scans was equalized, an additional test was done to verify this hypothesis. The noise levels in the perfusion maps were estimated by dividing the 512 × 512 pixel slices into a 16 × 16 matrices of square ROIs wherein the SDs of the tissue voxels were calculated. ROIs containing less than 75% tissue voxels were excluded. The noise level was considered equal to the lowest SD found. Relative noise levels were calculated by dividing the SD by the mean perfusion value.

Statistics on the means of all absolute and relative perfusion parameters of the patient group, as well as on the AUCs of the AIF and VOF, were presented in box plots. Repeated

measures ANOVA tests were applied to the perfusion measurements to test whether the mean values were significantly different for the various slice thicknesses ($p < 0.05$), and to calculate the SD of the parameters due to the slice thicknesses, s_B. The parameter s_B^2 is the 'between-group variance' as measured in an ANOVA test. It is the variance on a parameter due to the difference between slice thicknesses, disregarding the variation due to the difference between patients.

5.3 RESULTS

5.3.1 AIF and VOF
An impression of the mean AIFs and VOFs is given in Fig. 5.2. The median AUC of the VOFs, the AIF/VOF AUC ratio, and the width of the AIF as measured by gamma-variate curve fitting of the first-pass bolus are listed in Table 5.3. Conservation of matter requires that the AUCs of the AIF and VOF are equal in absence of partial volume effects. At a slice thickness of 0.8 and 2.4 mm the bilaterally filtered scans showed an approximately 100% AIF/VOF ratio that decreased to 69% at a slice thickness of 9.6 mm. For the isotropic Gaussian filtered scans the ratios were much lower, but the differences were less conspicuous with a median ratio of 57% at 0.8 mm thickness and 47% at 9.6 mm. Thick slice motion correction also yielded smaller AUCs and lower AIF/VOF ratios.

The width of the AIF increased with slice thickness. The full width at half maximum (FWHM) was on average 0.5 s higher at a slice thickness of 9.6 mm as compared to 0.8 mm.
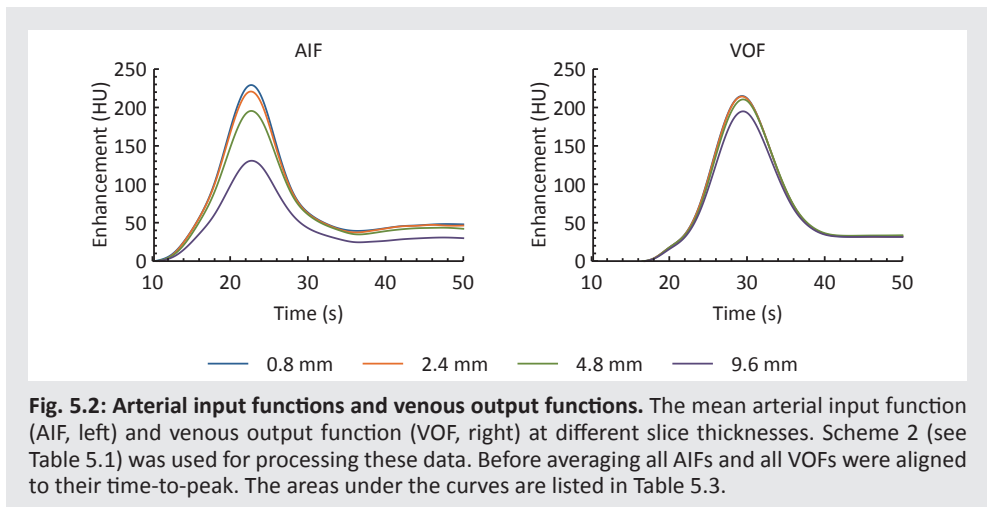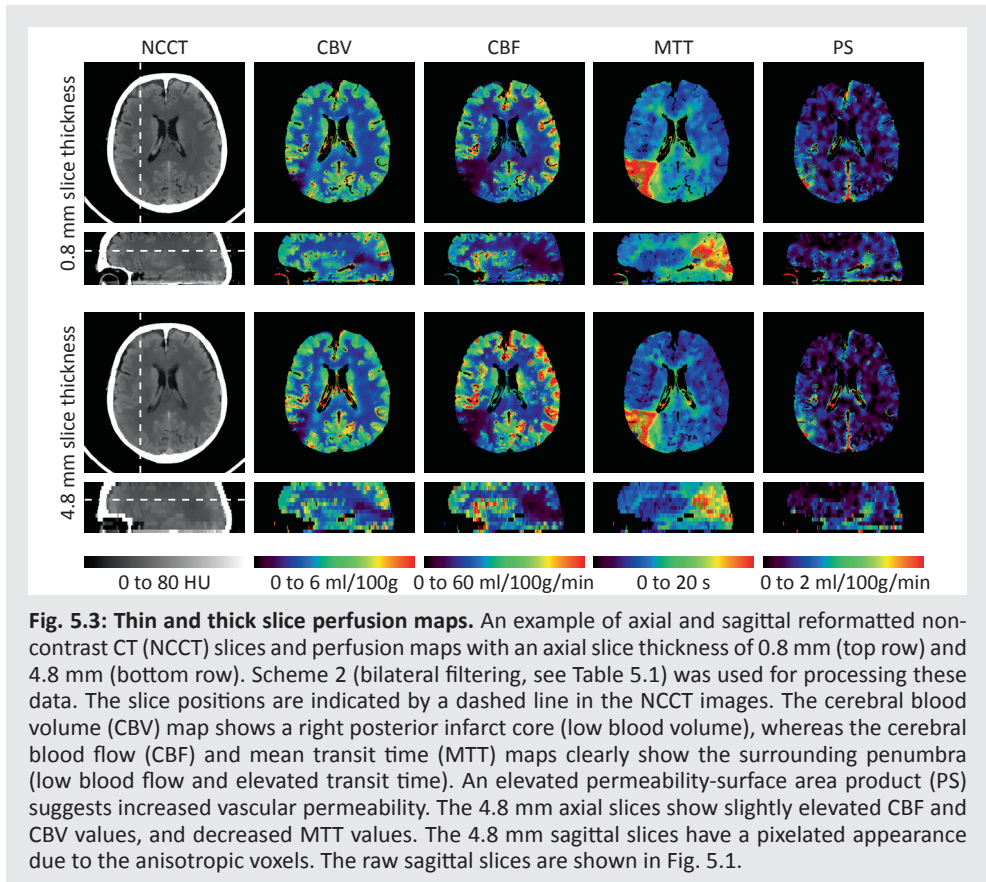

Fig. 5.2: Arterial input functions and venous output functions. The mean arterial input function (AIF, left) and venous output function (VOF, right) at different slice thicknesses. Scheme 2 (see Table 5.1) was used for processing these data. Before averaging all AIFs and all VOFs were aligned to their time-to-peak. The areas under the curves are listed in Table 5.3.

Table 5.3: Properties of the AIF and VOF curves. The median area under the curve of the venous output function (VOF), the ratio between the arterial input function (AIF) and VOF, and the full width at half maximum (FWHM) in case of isotropic Gaussian filtering (scheme 1), bilateral filtering (scheme 2), and bilateral filtering with thick slice motion correction (scheme 4). The number between brackets is the width of the interquartile range (IQR).

	Thickness (mm)	AUC of VOF (HU s)	AIF/VOF AUC ratio (%)	FWHM of AIF (s)
Isotropic Gaussian filter	0.8	1627 (888)	57 (44)	10.3 (2.3)
	2.4	1576 (788)	54 (27)	10.2 (2.2)
	4.8	1492 (768)	53 (37)	10.4 (2.5)
	9.6	1394 (772)	47 (32)	10.6 (2.5)
Bilateral filter	0.8	2200 (1059)	101 (23)	9.4 (2.1)
	2.4	2129 (1086)	100 (19)	9.7 (2.1)
	4.8	2102 (1031)	91 (21)	10.0 (2.2)
	9.6	1902 (730)	69 (22)	9.9 (2.2)
Thick slice motion correction	0.8	2200 (1059)	101 (23)	9.4 (2.1)
	2.4	2120 (996)	96 (21)	9.4 (2.0)
	4.8	2068 (845)	86 (24)	9.7 (1.8)
	9.6	1893 (900)	68 (19)	10.2 (2.0)

5.3.2 Perfusion Maps

Examples of the bilaterally filtered data and the resulting perfusion maps are shown in Fig. 5.3. Both the CBV and the CBF map showed consistently higher values on thicker slices (bottom versus thinner slices on top row). No visible differences in noise level were noticed in either the filtered CTP scans or the perfusion maps. CBV had a median relative noise SD of 7.8 % (IQR: 6.7 to 8.9 %) for all 700 analyzed scans (50 patients × 14 unique schemes), CBF of 12.0 % (IQR: 9.3 to 14.8%), MTT of 7.8 % (IQR: 5.6 to 10.7 %), and PS of 5.6 % (IQR: 2.8 to 10.0 %).

5

Fig. 5.3: Thin and thick slice perfusion maps. An example of axial and sagittal reformatted non-contrast CT (NCCT) slices and perfusion maps with an axial slice thickness of 0.8 mm (top row) and 4.8 mm (bottom row). Scheme 2 (bilateral filtering, see Table 5.1) was used for processing these data. The slice positions are indicated by a dashed line in the NCCT images. The cerebral blood volume (CBV) map shows a right posterior infarct core (low blood volume), whereas the cerebral blood flow (CBF) and mean transit time (MTT) maps clearly show the surrounding penumbra (low blood flow and elevated transit time). An elevated permeability-surface area product (PS) suggests increased vascular permeability. The 4.8 mm axial slices show slightly elevated CBF and CBV values, and decreased MTT values. The 4.8 mm sagittal slices have a pixelated appearance due to the anisotropic voxels. The raw sagittal slices are shown in Fig. 5.1.

5.3.3   Absolute Measurements

The distributions of the perfusion values (mean of the tissue voxels in both hemispheres) are shown in the box plots in Fig. 5.4 to Fig. 5.7. Table 5.4 lists the mean values of the absolute perfusion parameters, the standard deviations due to slice thickness, and *p*-values of the effect of slice thickness on the parameters.
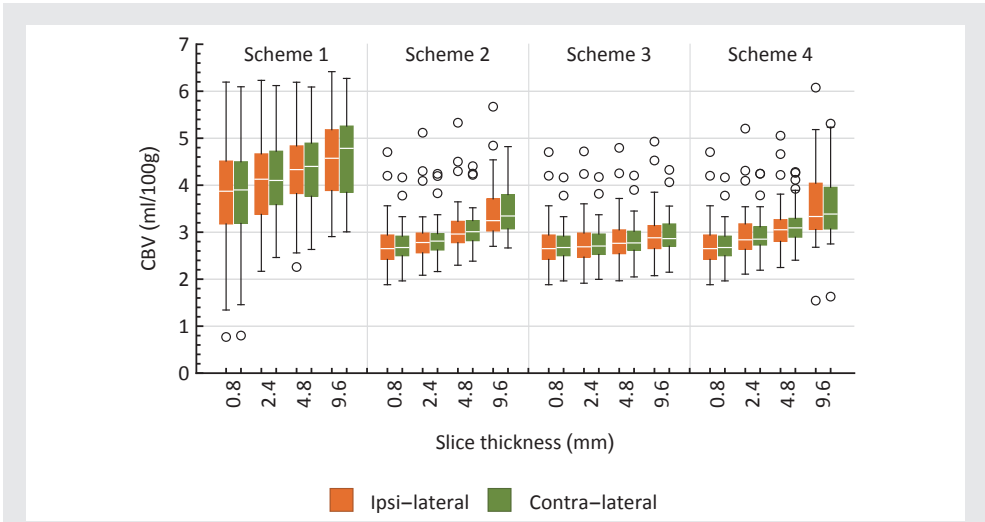
Fig. 5.4: Absolute CBV values. The box plots represent the median and quartiles that were observed in the tissue within each hemisphere (orange is ipsi-lateral, green is contra-lateral). Outliers, marked by circles, are defined as points that are more than 1.5× the interquartile range above the 75% quartile or below the 25% quartile.
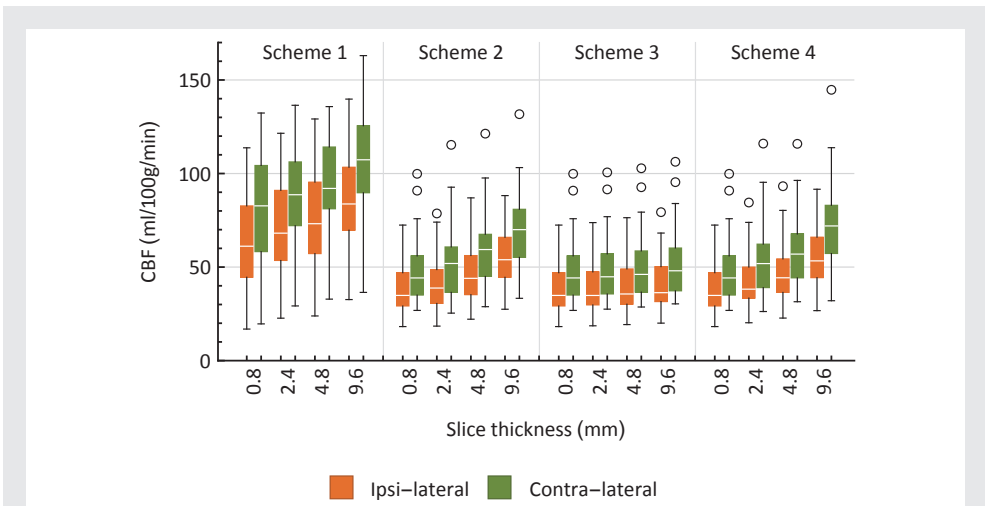

Fig. 5.5: Absolute CBF values. The box plots represent the median and quartiles that were observed in the tissue within each hemisphere (orange is ipsi-lateral, green is contra-lateral). Outliers, marked by circles, are defined as points that are more than 1.5× the interquartile range above the 75% quartile or below the 25% quartile.
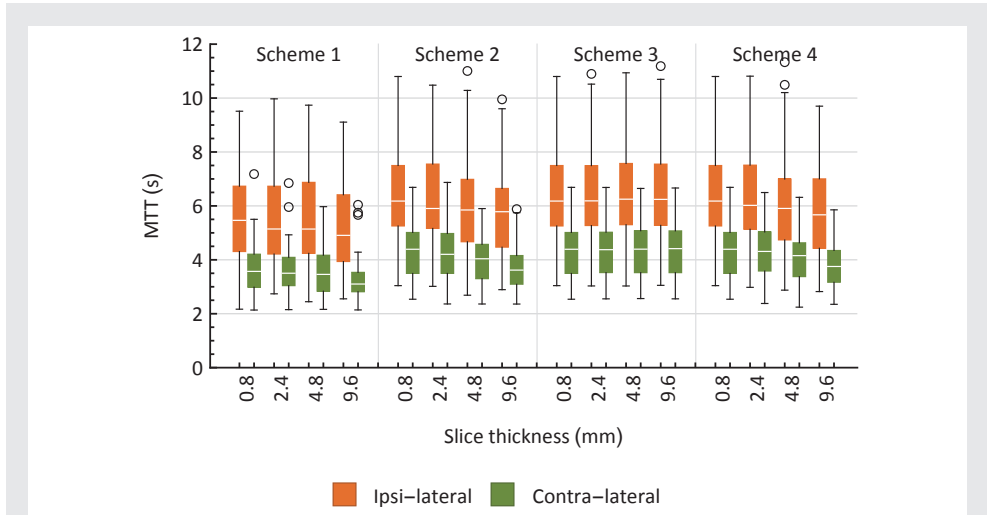
Fig. 5.6: Absolute MTT values. The box plots represent the median and quartiles that were observed in the tissue within each hemisphere (orange is ipsi-lateral, green is contra-lateral). Outliers, marked by circles, are defined as points that are more than 1.5× the interquartile range above the 75% quartile or below the 25% quartile.

Fig. 5.7: Absolute PS values. The box plots represent the median and quartiles that were observed in the tissue within each hemisphere (orange is ipsi-lateral, green is contra-lateral). Outliers, marked by circles, are defined as points that are more than 1.5× the interquartile range above the 75% quartile or below the 25% quartile.
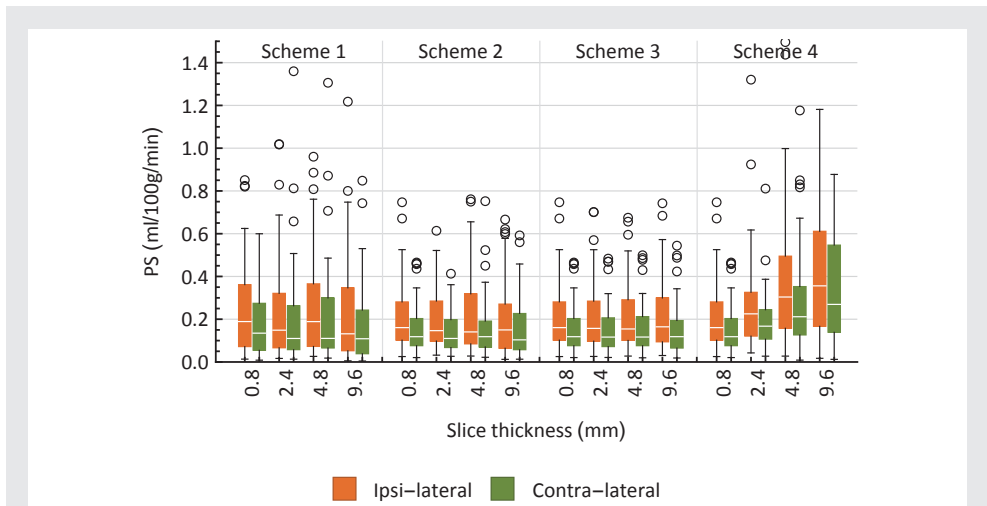
Table 5.4. Mean and variation in absolute perfusion parameters. The means, standard deviations (s_B), and *p*-values of the parameters, compared between slice thicknesses (repeated measures ANOVA). The parameters are subsequently cerebral blood volume (CBV, in ml/100g), cerebral blood flow (CBF, in ml/100g/min), mean transit time (MTT, in s), and permeability-surface area (PS, in ml/100g/min). The s_B is the standard deviation on a parameter due to the difference between slice thicknesses, disregarding the variation due to the difference between patients. A parameter with a *p*-value <0.05 was considered significantly affected by the slice thicknesses. *p*-values <0.01 are shown as 0.

		Scheme 1			Scheme 2			Scheme 3			Scheme 4		
	Side	μ	s_B	p	μ	s_B	p	μ	s_B	p	μ	s_B	p
CBV	Ipsilateral	4.2	2.3	0	3.0	2.3	0	2.8	0.72	0	3.1	2.5	0
	Contralateral	4.2	2.4	0	3.0	2.2	0	2.8	0.66	0	3.1	2.5	0
CBF	Ipsilateral	74	62	0	45	53	0	39	7.9	0	46	56	0
	Contralateral	92	75	0	57	68	0	49	11	0	58	73	0
MTT	Ipsilateral	5.4	1.1	0	6.2	2.0	0	6.4	0.17	0	6.2	1.9	0
	Contralateral	3.5	1.2	0	4.1	1.9	0	4.3	0.11	0	4.1	1.8	0
PS	Ipsilateral	0.28	0.23	0.37	0.24	0.34	0.21	0.32	0.05	0.12	0.36	0.49	0.09
	Contralateral	0.21	0.23	0.32	0.18	0.31	0.11	0.25	0.04	0.19	0.27	0.39	0.07

Absolute CBV and CBF values were higher with isotropic Gaussian filtering than with bilateral filtering (Fig. 5.4 and Fig. 5.5), whereas MTT values were a little lower (Fig. 5.6).

In all schemes, the absolute values of CBV, CBF, and MTT differed significantly between slice thicknesses ($p \ll 0.05$). Fig. 5.4 and Fig. 5.5 show positive trends for CBV and CBF with increasing slice thickness, and a slight negative trend in MTT. The variances due to slice thickness were much smaller in scheme 3 than in the other schemes. Absolute CBF and CBV were 22% and 14% lower on 0.8 mm as compared to 4.8 mm slices in scheme 4, but these differences were reduced to just 3% and 4% in scheme 3.

Although the box plot for absolute PS seems to show a trend in scheme 4 (Fig. 5.7), the absolute PS values did not significantly differ as a function of slice thickness in any case. Absolute PS values were 46% lower on 0.8 mm than on 4.8 mm slices in scheme 4, but these differences were reduced to just 3% in scheme 3.

5.3.4 Relative Measurements

Table 5.5 lists the mean values of the relative perfusion parameters, the standard deviations due to slice thickness, and *p*-values of the effect of slice thickness on the parameters. Differences between schemes, but also differences within schemes due to slice thickness were much smaller than for the absolute values.

Although s_B values were small, rCBV was significantly affected by the slice thickness in scheme 3 ($p < 0.05$). dMTT was also significantly different in scheme 1, 2, and 4, just as rPS in scheme 1, 2, and 3. In all these cases increasing slice thickness gave a small but significant positive bias to rCBV, dMTT, as well as to rPS. Because the interpatient variability is much larger than these biases, they cannot be observed in the box plots.

Stroke patients with an early infarct usually have a small infarct core, thus a small CBV defect on CTP imaging. For this reason the mean rCBV values were close to 100%. The volume of the surrounding penumbra, showing reduced CBF without reduced CBV, is usually much larger; mean CBF values were 20% lower, mean MTT values were 1.5 s higher, and mean PS values were 46% higher in the ipsi-lateral hemisphere.

Table 5.5. Mean and variation in relative perfusion parameters. The means (μ), standard deviations (s_B), and *p*-values of the parameters, compared between slice thicknesses (repeated measures ANOVA). The parameters are subsequently relative cerebral blood volume (rCBV, in %), relative cerebral blood flow (rCBF, in %), difference in mean transit time (dMTT, in s), and relative permeability-surface area (rPS, in %). The s_B is the standard deviation on a parameter due to the difference between slice thicknesses, disregarding the variation due to the difference between patients. A parameter with a *p*-value <0.05 was considered significantly affected by the slice thicknesses. *p*-values <0.01 are shown as 0.

	Scheme 1			Scheme 2			Scheme 3			Scheme 4		
	μ	s_B	p	μ	s_B	p	μ	s_B	p	μ	s_B	p
rCBV	99	2.1	0.15	100	1.3	0.21	100	2.3	0	100	0.59	0.90
rCBF	81	2.3	0.33	80	1.1	0.70	80	1.0	0.17	80	0.84	0.89
dMTT	1.6	0.22	0	1.5	0.20	0	1.5	0.005	0.98	1.5	0.20	0
rPS	149	72	0	144	42	0.01	143	28	0.02	146	79	0.06

5.4 DISCUSSION

The results of this study show how the use of thin slice CTP data for stroke diagnosis at equal noise level and radiation dose may be feasible without affecting relative perfusion values. It might however require revision of current clinical thresholds on absolute perfusion values. Partial volume effects (PVE) in the AIF plays a key role. Because even large veins are affected by PVE, scaling of the AIF to match the AUC of the VOF does not fully solve this issue. If the same PVE-free (thin slice) AIF is used for analysis of all slice thicknesses, slice thickness is of minor influence on the absolute perfusion values.

It was found that the PVE in the AIF and VOF may explain most, if not all findings in this study. PVE not only decreases the AUC of the AIF and VOF, but also increases the width of the AIF. For this reason PVE influences all perfusion parameters, including the MTT. PVE in tissue TACs only marginally influences the perfusion values, since the effect of partial volume on relatively large, homogeneous tissue regions is smaller than the PVE in vessels.

Both slice thickness and filtering methods influence the amount of PVE. Axel already described that CTP analysis would require venous attenuation curves to correct for partial volume in the AIF.[6] As expected, this study also showed that the AUC of the AIF reduces with increasing slice thickness. In line with a previous study by our group,[118] it can be concluded that a slice thickness of approximately 2 mm is required to measure a PVE free AIF in the

internal carotid artery (roughly 3.5 to 5 mm in diameter)[75,98] or in the middle cerebral artery (2.5 to 4 mm in diameter). Even the VOF, which is measured in much larger veins and used to rescale the AIF, is affected. Although bilateral filtering greatly reduces PVE as compared to isotropic Gaussian filtering (Table 5.3), the AUC of the VOF is on average as much as 13.5% lower at a slice thickness of 9.6 mm than at 0.8 mm.

Absolute CBV and CBF values were found to be higher with isotropic Gaussian filtering than with bilateral filtering. Because each AIF was scaled to match the AUC of the VOF, this is most likely caused by the difference in AUCs of the VOFs between both filters. The MTT values were also found to be a little lower with Gaussian filtering, which is probably caused by widening of the AIF due to PVE.

The effect of slice thickness on the PVE in the VOF and therefore on the perfusion values is most pronounced when the CBV and CBF values in scheme 3 are compared with the values in other schemes. Because of the use of the PVE-free (thin slice) AIFs and VOFs on all slice thicknesses, the values in scheme 3 are similar between slice thicknesses, whereas the other schemes clearly showed a positive trend for these parameters. This trend is in line with what was found by Van der Schaaf et al. (2006).[125]

A small negative trend was observed for the absolute MTT. Just like the use of the isotropic Gaussian filter resulted in lower MTT values, an increase in slice thickness also decreased MTT. Since the MTT values in scheme 3 did not show this trend, the trend is most likely caused by widening of the AIF due to PVE, as shown in Table 5.3.

Although the median PS was not found to be affected by slice thickness, a positive trend was observed in scheme 4 (Fig. 5.7). It is very likely that this trend is not caused by PVE, but rather by the noise introduced by motion artifacts. Noise gives a positive bias to permeability values (K^{trans} and PS), resulting in an apparent positive trend (see Fig. 3.8a in Chapter 3). PS values are probably more sensitive to motion artifacts than other perfusion parameters because they are influenced by the volumes acquired in the delayed phase (after the first pass bolus). In a longer time frame the chance of motion induced errors increases. When motion correction was performed on thin slices, as in schemes 1, 2, and 3, the trend disappeared.

In contrast to the finding that absolute quantification is mostly hindered by PVE in large arteries and veins, it was found that relative perfusion values were nearly unbiased. Scaling errors of CBV and CBF due to PVE in the AIF and VOF had no clinically relevant effect on their ipsi-lateral versus contra-lateral ratios, i.e. rCBV and rCBF. Similarly, MTT values in both hemispheres were equally biased due to widening of the AIF, causing the dMTT to be nearly unbiased. The cause of these small, but statistically significant biases is unknown. It should however be noted that the observation of a statistically significant bias does not necessarily imply a relevant effect, but it may merely indicate a precise measurement with some small systematic drift.

5

The data showed that the spread in absolute values between patients is quite large, especially for the CBF, MTT, and PS parameters. Although there might be significant interpatient variability, these parameters are also fundamentally more difficult to estimate than CBV. Whereas CBV is estimated by comparing AUCs, estimating CBF and MTT requires high-frequency information which is to a very limited extent available in the relatively smooth and wide AIF. The PS parameter is a very weak component of the tissue curves, requiring high quality curves, free of motion, over a long scan duration. When it is not possible to use a high-resolution, PVE-free AIF, then the use of relative perfusion values is advisable.

Chapter 6 investigates the effect of using thin slice CTP reconstruction on the detection of small volume strokes. Further study is required to find how other assumed advantages of using thin slice data, for example improved inter-observer and intra-observer variability, work out in clinical practice.

5.5 CONCLUSIONS

Performing thin slice CTP analysis at equal noise level and radiation dose might be feasible without affecting relative perfusion values. Due to PVE in large arteries and veins, it does however affect absolute perfusion values, of which CBF and CBV are most sensitive. Bilateral filtering enables the analysis of thin slice data, which may be used to more accurately locate and delineate the infarct core and penumbra and estimate blood-brain barrier permeability in CT perfusion imaging of acute ischemic stroke. Using thin slice data enables a PVE-free AIF selection for perfusion analysis, which gave the least variance in both absolute and relative perfusion values between slice thicknesses. In addition, motion artifacts can be reduced most effectively by 3D motion correction on thin slice data. Since the current thresholds on absolute values are generally established using AIFs and VOFs measured in scans with a slice thickness of 5 to 10 mm, they cannot be applied to thin slice data and may therefore need to be revised.

6
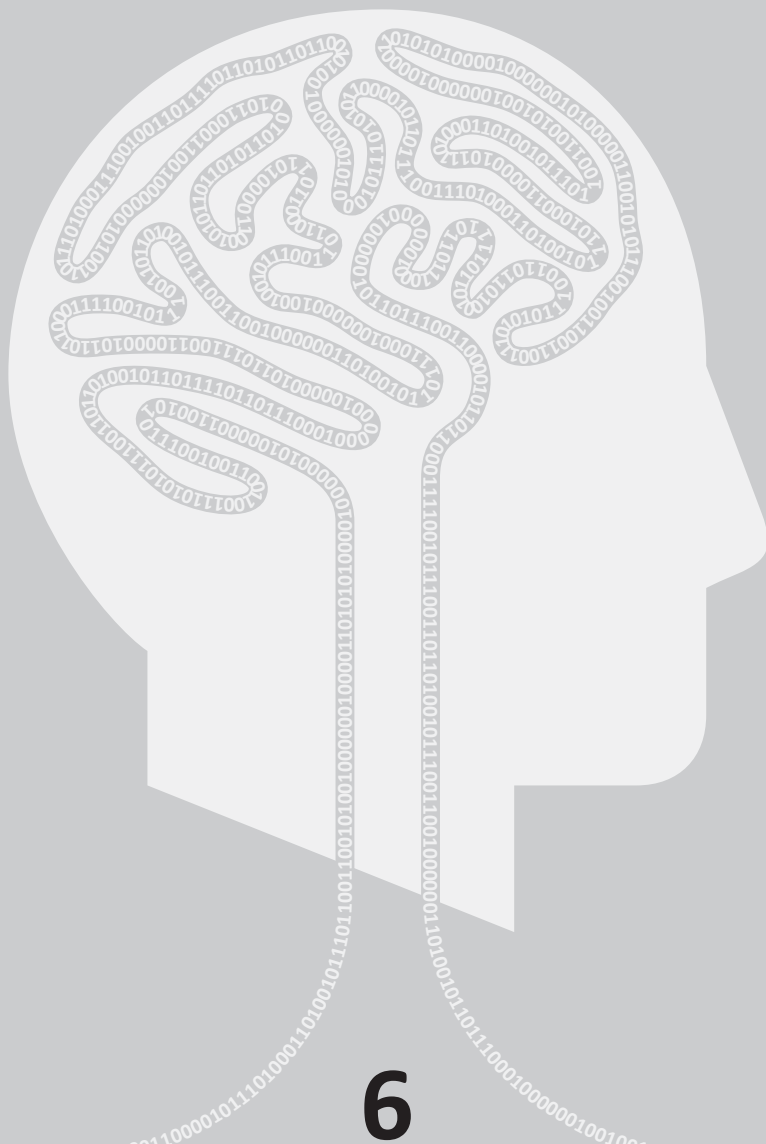
Thin Slice CTP Reconstruction for

Small Lesion Detection

ABSTRACT

CT perfusion (CTP) imaging helps to detect ischemia in patients with suspected ischemic stroke, but the detection of small lesions is challenging. We compared the performance of thin slice (0.8 mm) and thick slice (5 mm) CTP parameter maps for the detection of small ischemic lesions.

Data was extracted from a prospectively collected database (Dutch Acute Stroke Study). Additional inclusion criteria were: an infarct <20 mm on follow-up non-contrast CT within the CTP imaged volume, no occlusion on admission CTA, and available thick and thin slice admission CTP. For each case two controls were selected without an infarct on follow-up. Parameter maps of time to peak, mean transit time, blood flow and blood volume were calculated for both thick slice and thin slice CTP using a model-based analysis method. The parameter maps were randomized and evaluated for the presence of a focal perfusion deficit, blinded for follow-up non-contrast CT which served as reference standard. The performance was compared using McNemar's test.

41 cases and 82 controls were identified. There was no difference in median age (65 versus 67 years), median time to imaging (103 versus 107 minutes), or number of rt-PA treated patients (56% versus 54%). The median admission NIHSS was significantly lower in the control group (5 versus 3; p = 0.024). The sensitivity of thin slice CTP was significantly higher than thick slice (0.66 versus 0.44; p = 0.01). There was no difference in specificity (0.88 versus 0.90; p = 0.69).

Thin slice CTP improves the detection of small ischemic lesions in patients with suspected acute ischemic stroke without a visible occlusion on CTA.

6.1 INTRODUCTION

Lacunar or small volume strokes contribute up to 15 to 25% of all strokes.[8,70] The radiological definition for these infarctions varies widely among researchers, but is mostly defined as a lesion of up to 15 to 20 mm in diameter. Small volume infarctions are usually situated in the deep gray matter (basal ganglia and thalamus), deep white matter (internal capsule, corona radiate or brainstem), or subcortical white matter.[113,141] Single penetrating artery occlusion based on small vessel disease is considered the main cause.[104] Thrombolytic therapy has been found to improve functional outcome across all stroke subtypes.[89,108] However, since thrombolytic therapy can cause serious side-effects such as intracranial hemorrhage, it is important that acute ischemic stroke can be accurately diagnosed. Using non-contrast CT (NCCT) only, approximately 50% of the lacunar infarcts will be missed within 48 hours after onset.[92,133] Adding CT-perfusion (CTP) to clinical and NCCT findings has been found to improve diagnostic accuracy for detection of stroke overall.[29,56,87] CTP is found to be twice as sensitive for stroke detection in the first hours after symptom onset compared to NCCT.[21,87,105] In a multimodal CT imaging, especially the specificity for stroke detection increases because of CTP.[120] Moreover, CTP has been found to improve detection of posterior circulation infarctions.[53,84] However, the sensitivity of CTP for small volume infarctions remains limited.[37,50,52,87,90] A recent meta-analysis shows that about two-thirds of false negative CTP results are caused by small volume infarctions.[17] The remaining false negatives are mostly due to limited CT coverage (Fig. 1.8). In addition a recent study showed that a combined NCCT, CT-angiography (CTA), and CTP protocol has a sensitivity of only 42% for lacunar strokes.[35] This confined sensitivity for small volume infarctions may be caused by limited spatial resolution.[17,50] High resolution, thin slice CTP with advanced filtering, as studied in the previous chapter, may therefore lead to an increased sensitivity of CTP for small volume infarctions.

The purpose of this study was to investigate the diagnostic value of 0.8 mm thin slice CTP reconstructions compared to 5 mm thick slice reconstructions in the detection of small volume ischemic lesions in adults suspected for ischemic stroke.

6.2 METHODS

6.2.1 Patient Selection
All patients were selected from the Dutch acute stroke study (DUST) database. The inclusion criteria and the CTP acquisition protocol are described in Section 1.4. Additional inclusion criteria for the current study were; available follow-up NCCT with an infarct <20 mm in diameter within the CTP imaged volume, no occlusion on admission CTA, and available thick

and thin slice admission CTP data. For each case two controls were selected matching the same inclusion criteria but without an infarct on follow-up NCCT.

6.2.2 Imaging Protocol

On admission NCCT, CTP, and CTA of the vessels of the head and neck were performed. A follow-up NCCT was performed if possible at day 3 after symptom onset and earlier in case of clinical deterioration. Admission and follow-up NCCT were performed at 120 kVp, 300 to 375 mAs, and the scans were reconstructed to a slice thickness of 5 mm. The CTP acquisition protocol is described in Section 1.4.2 in the Introduction; the 6 extended acquisitions were not used in this study. The CTA was acquired from aortic arch to the cranial vertex with 50 to 70 ml contrast followed by 40 ml of saline, both with a flow of 6 ml/s. The scan delay after intravenous injection was calculated from time to peak arterial enhancement on CTP, or by trigger-based Hounsfield threshold measurement of contrast enhancement in the aortic arch.

6.2.3 Preprocessing

Automated rigid 3D motion correction was done using the open source registration toolbox Elastix.[67] The skull served as a reference for registering all acquired volumes to the first.

A standard 3D bilateral filter with spatial standard deviation of 3 mm and a similarity standard deviation of 20 HU^2 for thick slice scans and 50 HU^2 for thin slice scans was used to reduce the noise with minimal loss of resolution (see Section 2.2.5).[137] Similarity was defined as the squared difference between the mean of two time-attenuation curves.

6.2.4 Perfusion Analysis

Presence of occlusion on admission CTA and presence of a new infarct on follow-up NCCT imaging was evaluated by one of three observers (BKV, ICvdS, JWD). All observers had more than 4 years of experience in stroke imaging evaluation.

The filtered CTP scans were analyzed using the model-based NLR method as described in Section 2.2.2 of Chapter 2.[14] Next to the cerebral blood volume (CBV), cerebral blood flow (CBF), and mean transit time (MTT) maps, a time-to-peak (TTP) map was calculated. The TTP is the time difference between the first pass bolus peaks of the artery and tissue (Fig. 1.9). In this study it is estimated as TTP $\approx t_d$ + MTT/2, where t_d is the delay in contrast arrival as measured with NLR. The TTP is of importance in visual assessment of CTP maps, since it merges the information in MTT and t_d into a more robust parameter. The relatively low signal-to-noise ratio and, notably, the large width of the AIF are limiting factors to the availability of high-frequency information in the attenuation curves. As a result, these factors limit the precision of MTT and delay measurements. An underestimated MTT results in an overestimated delay and vice versa.

Thick slice and thin slice CTP data were evaluated separately. Patients were randomized for both evaluations. Presence of ischemia was evaluated by one observer (JWD), blinded for the reference standard and patient details. Presence of a perfusion deficit on admission was defined as a focal defect on any of the 4 perfusion maps. For each perfusion deficit the anatomic location was noted.

6.2.5 Statistical Analysis

The presence of a new infarct on follow-up NCCT was used as the reference standard. Sensitivity and specificity and corresponding 95% confidence interval (CI) for the detection of small infarcts were calculated separately for thick slice and thin slice CTP. Subsequently, sensitivity and specificity were compared using McNemar's χ^2 test for paired nominal data. Significance was predefined at $p < 0.05$.

6.3 RESULTS

Of the 1223 patients in the DUST database with diagnosed ischemic stroke, 41 patients matched the inclusion criteria (Fig. 6.1). For every case, two controls were selected resulting in a total of 123 patients. Patient characteristics are summarized in Table 6.1.
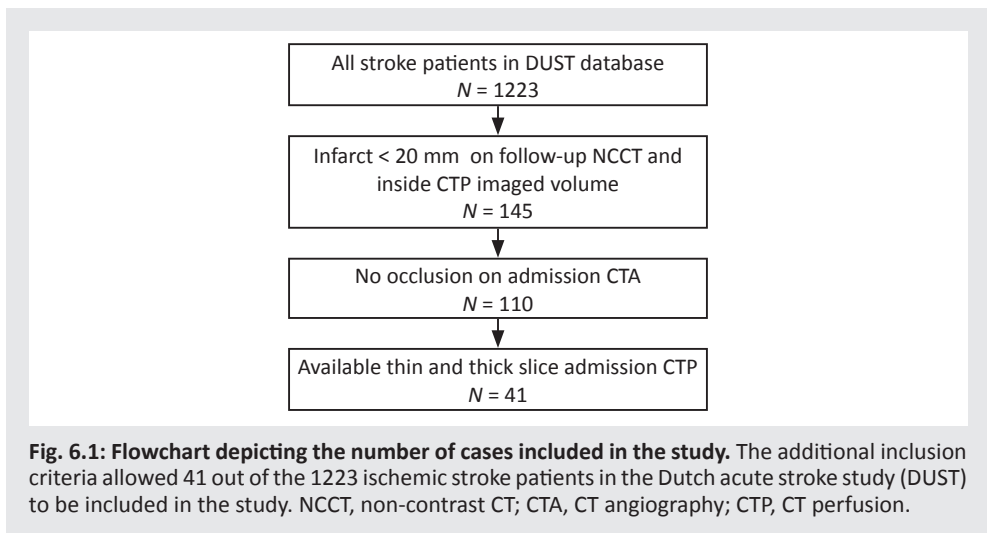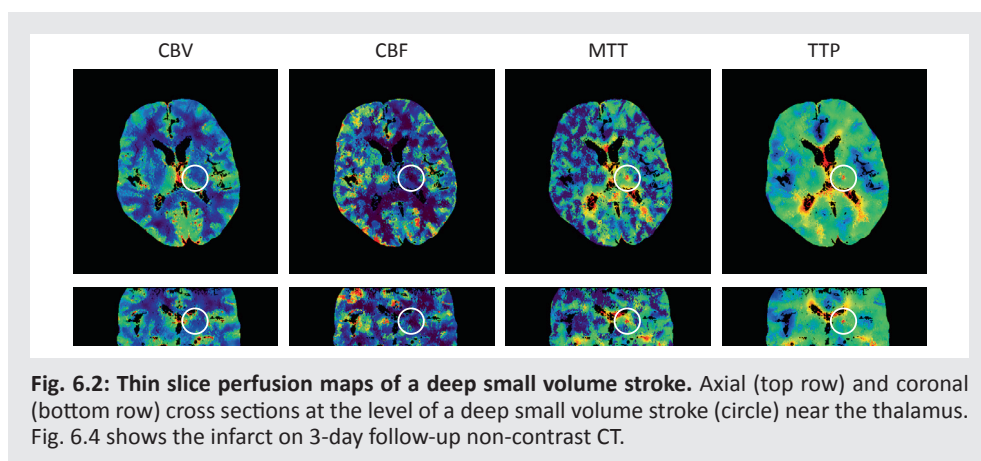
6

All stroke patients in DUST database
$N = 1223$

Infarct < 20 mm on follow-up NCCT and inside CTP imaged volume
$N = 145$

No occlusion on admission CTA
$N = 110$

Available thin and thick slice admission CTP
$N = 41$

Fig. 6.1: Flowchart depicting the number of cases included in the study. The additional inclusion criteria allowed 41 out of the 1223 ischemic stroke patients in the Dutch acute stroke study (DUST) to be included in the study. NCCT, non-contrast CT; CTA, CT angiography; CTP, CT perfusion.

Table 6.1: Patient characteristics.

	All patients N = 123	New stroke N = 41	No new stroke N = 82	*p*-value
Clinical parameters				
Age (years), median (IQR)	66 (54, 76)	65 (50, 74)	67 (56, 77)	0.17
Female sex, *n* (%)	49 (40)	16 (39)	33 (40)	1.00
Admission NIHSS, median (IQR)	4 (2, 7)	5 (3, 8)	3 (2, 5)	0.024*
Time to imaging (min), median (IQR)	106 (78, 197)	103 (79, 213)	107 (77, 181)	0.35
Treatment				
IVT, IAT or MT, *n* (%)	67 (54)	23 (56)	44 (54)	0.85
Follow-up				
mRs > 2 after three months, *n* (%)	25 (20)	8 (20)	17 (21)	1.00

Pearson's χ^2 test was used to compare categorical variables and Mann-Whitney *U* test for continuous variables. *p < 0.05. CTA, CT angiography; CTP, CT perfusion; IAT, intra-arterial thrombolysis; IQR, interquartile range; IVT, intravenous thrombolysis; mRs, modified Rankin scale; MT, mechanical thrombectomy; NCCT, non-contrast CT; NIHSS, National Institutes of Health Stroke Scale.

Fig. 6.2 and Fig. 6.3 show examples of thin slice and thick slice perfusion maps. Fig. 6.4 shows the admission and 3-day follow-up NCCT from the same patient. The outcomes of infarct detection on thick slice and thin slice CTP are given in Table 6.2. All 18 thick slice true positives and 27 thin slice true positives were scored on the correct location. Sensitivities and specificities with corresponding confidence intervals for the detection of new infarctions are listed in Table 6.3. The sensitivity was significantly higher with thin slice assessment compared to thick slice assessment, 0.66 versus 0.44 respectively. Specificity was slightly higher but not statistically different with thick slice assessment compared to thin slice assessment, 0.90 versus 0.88 respectively.
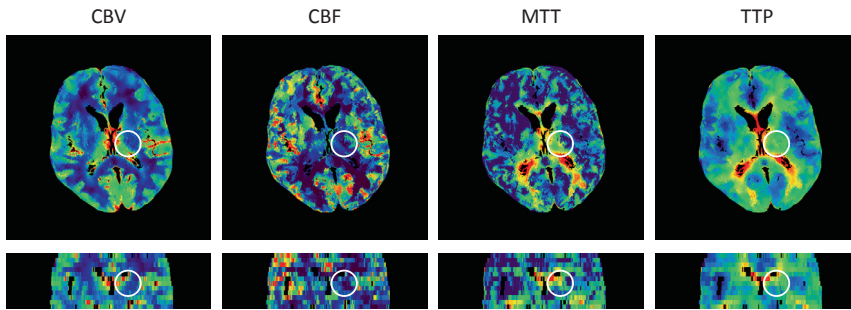

Fig. 6.2: Thin slice perfusion maps of a deep small volume stroke. Axial (top row) and coronal (bottom row) cross sections at the level of a deep small volume stroke (circle) near the thalamus. Fig. 6.4 shows the infarct on 3-day follow-up non-contrast CT.

Fig. 6.3: Thick slice perfusion maps of a deep small volume stroke. Axial (top row) and coronal (bottom row) cross sections at the level of a deep small volume stroke (circle) near the thalamus. Although the slice positions and window/level settings are equal to those of Fig. 6.2, the contrast between the lesion and background is much lower. Fig. 6.4 shows the infarct on 3-day follow-up non-contrast CT.
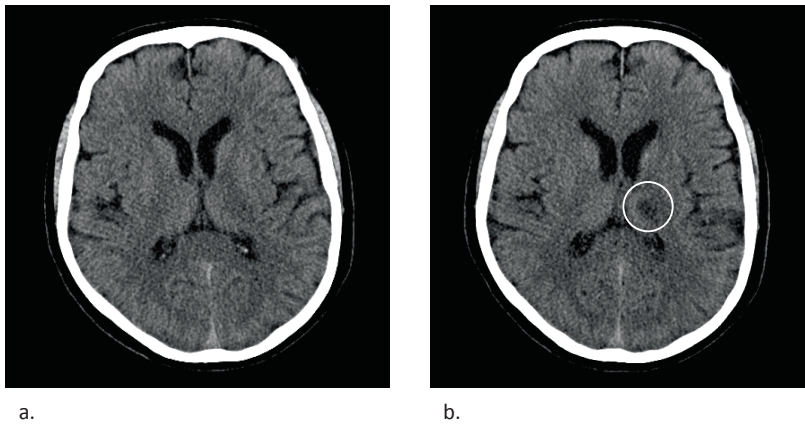

a.　　　　　　　　　　　　　　　b.

Fig. 6.4: Admission (a) and 3-day follow-up (b) non-contrast CT of a deep small volume stroke. Axial cross section (5 mm slice thickness) at the level of a deep small volume stroke (hypodense area in circle) near the thalamus. These images show the same patient as in Fig. 6.2 and Fig. 6.3.

Table 6.2: Performance of infarct detection.

		New stroke	No new stroke	Total
Deficit detected	Thick slice CTP	18 (44%)	8 (10%)	26 (21%)
	Thin slice CTP	27 (66%)	10 (12%)	37 (30%)
No deficit detected	Thick slice CTP	23 (56%)	74 (90%)	97 (79%)
	Thin slice CTP	14 (34%)	72 (88%)	86 (70%)
Total		41 (100%)	82 (100%)	123 (100%)

Table 6.3: Association measurements.

	Sensitivity (95% CI)	Specificity (95% CI)
Thick slice CTP	0.44 (0.29, 0.59)	0.90 (0.83, 0.96)
Thin slice CTP	0.66 (0.51, 0.78)	0.88 (0.78, 0.94)
***p*-value**	0.01*	0.69

McNemar's χ^2 test for paired nominal data was used to compare sensitivity and specificity. *$p < 0.05$.

6.4 DISCUSSION

Reliable and early detection of small volume infarctions is important to improve treatment decision making.[131] The aim of this study was therefore to investigate the diagnostic value of thin slice CTP assessment compared to thick slice CTP evaluation in de detection of small volume infarctions. To our knowledge, this is the first study to investigate the additional diagnostic value of thin slice CTP assessment. This study found a 1.5× higher sensitivity for the detection of small volume strokes with the use of thin slice CTP, as compared to thick slice CTP. The specificity was not significantly different. Relatively low diagnostic detection rates were found for both thick slice and thin slice assessment. This is in accordance with other articles that studied the diagnostic properties of CTP in the detection of lacunar strokes and other types of small volume strokes.[37,50]

Although 15 to 25% of all strokes should be small volume strokes, just 12% of the stroke patients in the DUST study had an infarct size <20 mm (Fig. 6.1). One possible explanation is that some minor strokes were not included in DUST because of the stroke severity inclusion criterion; a National Institutes of Health Stroke Scale (NIHSS) score ≥2, or 1 if an indication for rt-PA therapy is present. Other possible explanations of this bias are that patients with minor stroke symptoms and/or quick recovery did not always undergo follow-up NCCT and some infarcts on follow-up NCCT may not have been detected, which are likely to be small volume strokes.

In this study patients were excluded if the ischemic area was outside the volume imaged in the admission CTP scan. This way we investigated the sole diagnostic properties on the detection of small volume infarction, without these false negatives influencing our results. This means the false negative results in our study were either caused by limited spatial resolution, as in the example in Fig. 6.3, or by the presence of image noise obscuring the perfusion deficit. In thick slice assessment limited spatial resolution can cause difficulties in infarct detection, because small volume infarcts can be missed due to partial volume effects. The problem of noise obscuring small volume strokes is most prominent in the cortical regions, where perfusion is rather heterogeneous. More noise reduction can be achieved by increasing filter strength, but then small volume infarctions could be filtered out as well.

False positives were either caused by image noise (in both thick slice and thin slice data), or caused by transient ischemia. In transient ischemia, reperfusion may occur spontaneously or as a result of thrombolytic treatment. The number of false positives was slightly higher when using thin slice CTP data, causing a lower specificity. Just as small infarcts can be missed due to partial volume effects on thick slice CTP, small false positive defects on thin-slice CTP could also become less visible on thick slice CTP. Transient ischemia will cause false positives in both thick slice and thin slice CTP data and is therefore less likely to explain the difference in false positives.

Despite the previously mentioned difficulties in CTP assessment, a strength of this study is the randomization and blinding for both clinical and imaging parameters. In a case-control study of a condition with low incidence (12%), this is the best way to assess the acquired data. A limitation of this study is the relatively small number of cases, which is caused by the lack of thin slice CTP data in the majority of patients with small volume infarction. Standardization of thin slice CTP acquisition in stroke patients could enable the acquisition of more dependable results.

Diffusion-weighted MR imaging (DWI) is still considered the gold standard for detection of small vessel infarctions.[60,115] Several studies showed that CTP cannot yet predict small ischemic lesions as well as MRI.[52,57] However, MRI has certain disadvantages as well, as MRI is not always available in emergency situations and contraindications for MRI are substantial drawbacks in acute care.[30]

6

6.5 CONCLUSIONS

Thin slice CTP improves the detection of small ischemic lesions in patients with suspected acute ischemic stroke without a visible occlusion on CTA. Although DWI still performs better in detecting small lesions, improvements in CTP reconstruction and filtering might enhance the performance of CTP.
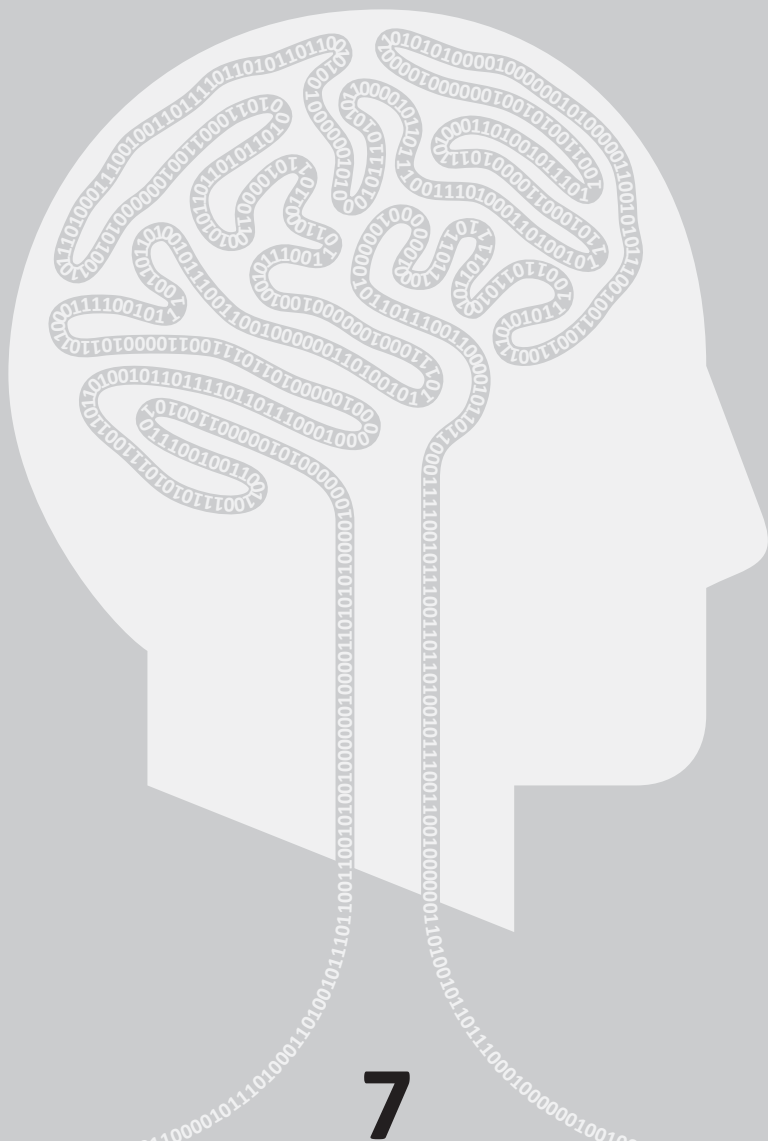
7

Summary and Discussion

7.1 SUMMARY

Timely thrombolytic therapy can improve clinical outcome in acute ischemic stroke patients. However, the risk/benefit ratio of the therapy not only depends on time, but also on the size and location of the infarcted and salvageable tissue regions, and on the risk of developing hemorrhagic transformation (HT). Although CT perfusion (CTP) imaging enables rapid diagnosis and prognosis of ischemic stroke, current CTP analysis methods have several shortcomings. The research presented in this thesis aims to develop quantitative analysis methods that could increase the effectiveness of CTP imaging in selecting patients for thrombolytic therapy.

In CTP imaging, a series of scans is acquired that tracks a contrast bolus passage through the tissue over time. By means of tracer kinetic analysis, a number of informative perfusion maps can be extracted. These maps generally include cerebral blood volume (CBV), cerebral blood flow (CBF), mean transit time (MTT), and time-to-peak (TTP). Extending the duration of CTP imaging may allow measuring vascular permeability. Since permeability due to blood-brain-barrier damage is a potential predictor for HT, CTP imaging may not only be used for quantifying perfusion, but also for estimating the risk on developing HT.

This thesis presents a fast model-based analysis method that has important advantages over the current state-of-the-art method, block-circulant singular value decomposition (bSVD), notably improved robustness to local tracer delay, fewer tuning parameters, and extensibility to permeability estimation. In **Chapter 2** this method is compared with bSVD and with a commercial SVD-based method for CT perfusion analysis. The three methods were evaluated by means of a digital perfusion phantom and with the aid of 50 clinical CT perfusion scans. All methods showed high correlation with the ground truth in the phantom. In the clinical scans, the perfusion maps of the model-based method showed higher correlation with bSVD than the maps from the commercial method. Furthermore, it was shown that the model-based estimates are more robust to noise and truncation than both the bSVD and commercial method. These findings suggest that the model-based method could be a viable alternative to current methods.

Permeability is commonly estimated by means of Patlak analysis, which applies linearized regression to CT perfusion data. Applying more elaborate kinetic models by means of non-linear regression (NLR) may improve precision, but this is more time-consuming and therefore less appropriate in an acute stroke setting. The study described in **Chapter 3** compared our fast, simplified model-based method to variations on Patlak analysis and other NLR methods. Confidence intervals for the permeability estimates were evaluated using simulated CT time-attenuation curves and clinical data from 20 patients. The NLR methods yielded significantly more reliable estimates than Patlak analysis, but took up to 12× longer to calculate. The simplified model-based method was approximately 4× faster

than other NLR methods, while maintaining the same confidence intervals. It was concluded that the simplified model-based method is a new, reliable way to estimate permeability in stroke, fast enough for clinical application in an acute setting.

Chapter 4 aimed to assess whether the prediction of HT can be improved by measuring vascular permeability using the novel fast model-based method instead of using Patlak analysis. 20 patients with HT on follow-up imaging and 40 patients without HT were selected. By means of Mann-Whitney U tests and receiver operating characteristic (ROC) analyses, the discriminative power of different perfusion and permeability parameters was assessed. Permeability values measured with the model-based method were found significantly higher in the patients who developed HT as compared with those who did not, whereas the values measured with standard Patlak analysis were not. The relative permeability-surface area product (rPS), measured with the model-based method, had the highest discriminative power. ROC analysis of rPS showed an area under the curve (AUC) of 0.75.

In **Chapter 5** the influence of slice thickness on CT perfusion analysis is investigated. Although CT scanners generally allow dynamic acquisition of thin slices (1 mm), thick slice (≥5 mm) reconstruction is commonly used for stroke imaging to reduce data, processing time, and noise level. Thin slice reconstruction may suffer less from partial volume effects, and thus yield more accurate quantitative results with increased resolution. In addition they may allow for detection of smaller lesions. Before clinical application, the impact of thin slices on CTP analysis should be investigated. Average estimates of CBV, CBF, MTT, and permeability-surface area product (PS) were compared between 4 slice thicknesses (0.8 to 9.6 mm) in 50 patient studies. Absolute CBF, CBV and PS were 22%, 14% and 46% lower with 0.8 mm than with 4.8 mm slices. It was found that partial volume effects in large vessels lead to these biases; if the AIF and motion correction were based on thin slices prior to reconstruction of thicker slices, these differences reduced to 3%, 4% and 3%. However, current thresholds, which are mostly based on absolute values on 5 to 10 mm slices, need to be revised for thin slice use before clinical application is possible. The effect of slice thickness on relative values (i.e. ipsi-lateral versus contra-lateral) was very small. The findings suggest that thin slice reconstruction for CTP is feasible, but the effects of reconstruction slice thickness should be taken into account when absolute perfusion values are used for clinical decision making.

Thin slice reconstruction may aid in the detection of small lesions in CTP imaging. **Chapter 6** compared the performance of thin slice (0.8 mm) and thick slice (5 mm) parameter maps for the detection of small ischemic lesions. The maps from 41 cases and 82 controls without an infarct on follow-up non-contrast CT were randomized and evaluated for the presence of a focal perfusion deficit. The sensitivity of thin slice CTP was found significantly higher than thick slice (0.66 versus 0.44; p = 0.01), while there was no difference in specificity (0.88 versus 0.90; p = 0.69). Although diffusion-weighted MR imaging is still considered the gold standard for the detection of small ischemic lesions in acute ischemic stroke, it can be concluded that thin slice reconstruction improves the detection with CTP.

7.2 GENERAL DISCUSSION

CT brain perfusion analysis has been found to improve diagnosis and treatment planning in acute ischemic stroke.[19,26,47] Its current diagnostic value above non-contrast CT and CTA is, however, not overwhelming. And the most significant advantages of CT over MR imaging in acute stroke are the availability of CT scanners in emergency departments, contraindications for MR and costs, rather than diagnostic image quality. This is, however, not the end of the matter. CTP analysis has the potential to be more quantitative and therefore more reliable, but this is troubled by several factors, which are mostly due to a low signal-to-noise ratio (SNR). The challenge is to achieve good quality results at an acceptable radiation dose. The research presented in this thesis shows that, besides the developments in CT acquisition and reconstruction, considerable benefits can achieved in the analysis of CT brain perfusion scans. Because of the ever ongoing increase in computer performance, more advanced analysis methods can now be used to exploit this imaging technique to its full potential, even in a time-critical clinical setting. At the same time other studies showed that dynamic CT acquisition might have more applications in stroke, such as timing-invariant 4D-CTA, measurement of vascular hemodynamics, or contrast enhanced thrombus characterization.[74,106]
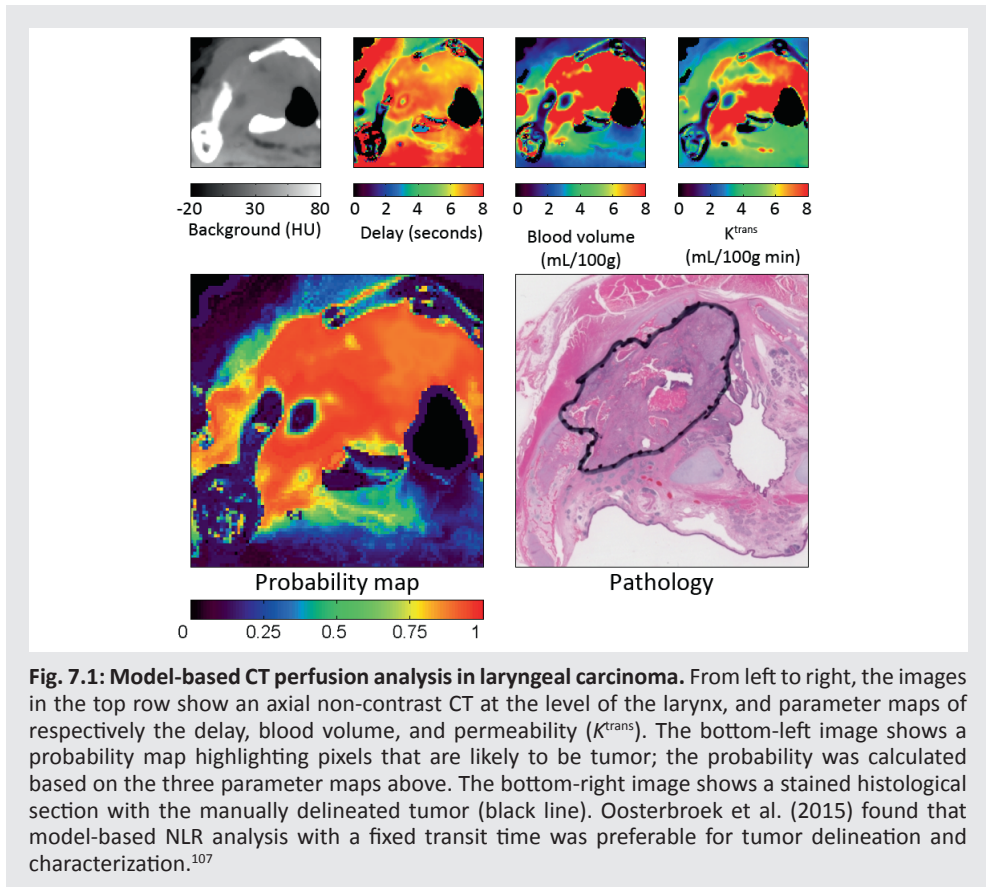
The studies presented found that the theoretical advantages of using a model-based method for CT brain perfusion analysis pay off in practice. Least-squares fitting of a perfusion model does not require regularization, which keeps it simple in use but robust to noise and quantitative in nature. It allows of extrapolation, and is therefore robust to truncation of attenuation curves (as shown in Section 2.3.3). It was found that model-based analysis performs equally to state-of-the art delay-insensitive SVD-based methods in terms of Pearson correlation to a digital phantom (Section 2.3.1), but provides better matching physiological values in clinical data (Section 2.4.4). Further clinical study is required to investigate its effectiveness in selecting patients for rt-PA treatment.

The flexible perfusion model can also be extended to allow measuring permeability, as shown in Chapter 3. It was found that the use of this unified model, describing both perfusion and permeability, is more reliable than measuring permeability through linearized regression by means of a standard Patlak plot. A unified model allows including all samples of the attenuation curve for estimating permeability, whereas the currently used Patlak analysis excludes the first pass bolus since it requires steady arterial tracer concentration. As a result, standard Patlak analysis was not able to predict hemorrhagic transformation (HT) in stroke, whereas model-based analysis was able to discriminate between HT and non-HT groups, as shown in Chapter 4. The relative permeability-surface area product was found to have the highest predictive value of all permeability and perfusion parameters (Section 4.3). Although this is a significant improvement over Patlak analysis, the diagnostic value

of HT prediction is still quite low. A larger number of acquisitions and longer duration of the extended scan could simply improve this diagnostic value, but the improvement would probably not counterbalance the additional patient burden due to increased duration and radiation exposure. Model-based analysis, however, allows of using more complex, non-uniform acquisition protocols that could more efficiently distribute the radiation exposure and information density throughout the acquired frames. This concept, which deserves further investigation, is discussed in Section 7.2.2. The inclusion of multiple perfusion parameters as well as clinical and demographic data in a multivariate analysis might also improve HT prediction, but investigating this requires a larger stroke cohort.

It was found that the perfusion model does not need to be complex in order to provide good results. A physiologically accurate shape might give perfusion values with a higher accuracy, but it will probably only have a minor effect on the precision. A simple box-shaped impulse response function (IRF) allows omitting convolution, significantly increasing the computational performance (Sections 3.2.3 and 3.2.7). A fast method gives the opportunity to assess thin-slice CTP scans in an acute clinical setting, utilizing the CT hardware to its full extent. Though thin slices show far higher noise levels than thick slices, bilateral filtering enables reducing the noise to equal levels while maintaining the advantage of thin slices, providing more detail and less partial volume effects (Section 2.2.5). If the arterial input function (AIF) is not affected by partial volume, then slice thickness is of minor influence on absolute perfusion values (Chapter 5). However, since current thresholds on absolute values were established using thick-slice AIFs and VOFs, these might need revision before application to thin-slice scans. Thin slice CTP analysis was shown to be feasible, and it was found that the sensitivity for detecting small volume strokes (<20 mm) was 1.5× higher when using 0.8 mm slice thickness instead of 5 mm, the current clinical standard (Chapter 6).

It is also noteworthy that the techniques described in this thesis are potentially applicable to other functional imaging techniques, pathologies, and organs as well. One could think of tumor assessment using DCE-MR or PET, even though the SNR and perfusion kinetics might differ. The model-based NLR methods for permeability analysis have been successfully applied to CT perfusion imaging of laryngeal carcinoma (Fig. 7.1).[107] Since cancerous tissue can be highly permeable, the perfusion models allowing reversible leakage (Eq. 3.7 and Eq. 3.10) were found to be preferable for tumor delineation and characterization.

Fig. 7.1: Model-based CT perfusion analysis in laryngeal carcinoma. From left to right, the images in the top row show an axial non-contrast CT at the level of the larynx, and parameter maps of respectively the delay, blood volume, and permeability (K^{trans}). The bottom-left image shows a probability map highlighting pixels that are likely to be tumor; the probability was calculated based on the three parameter maps above. The bottom-right image shows a stained histological section with the manually delineated tumor (black line). Oosterbroek et al. (2015) found that model-based NLR analysis with a fixed transit time was preferable for tumor delineation and characterization.[107]

7.2.1 Limitations

A prominent limitation of this research is the lack of verifiable ground truth of the clinical perfusion maps. A digital perfusion phantom does provide a ground truth, but the true shape of a physiological impulse response function (IRF) is unknown. It is unlikely, however, that there will be a wide variety in shape in physiological IRFs, apart from scaling of height and width due to blood volume and velocity. Since the presented model-based NLR method was robust to noise and truncation, and showed superior R^2 values and correlation coefficients for each IRF shape in the digital phantom (Table 2.1), a yet unknown scaling factor would be sufficient to provide true quantitative perfusion values.

Despite the fact that the NLR method improves upon Patlak analysis, the power for predicting hemorrhagic transformation from CT perfusion imaging is still very small. There is however room for improvement. Permeability estimates could be improved by increasing the SNR and extending scan duration, but also by improving the detector calibration. It

was found that the permeability maps of approximately 20% of the clinical CTP scans were affected by ring-shaped artifacts caused by poor detector calibration in combination with head movement. Enhanced or more frequent calibration could have prevented this issue. A fourth generation scanner design, having a fixed 360° detector ring instead of a rotating 60° detector array, might also reduce this issue.[27]

Although iterative tomographic reconstruction methods have been available for some years, most of the CTP scans in the DUST study were reconstructed using filtered backprojection. This can be considered a limitation of the study. Currently available model-based iterative reconstruction methods significantly increase SNR as compared to filtered backprojection, allowing up to 80% dose reduction with similar or even superior image qualtiy.[144,145] Since low SNR is a major issue in CTP analysis, it is to expect that iterative reconstruction would have improved the quality of the perfusion maps significantly.

7.2.2 Future Perspectives in Functional CT Imaging

Mainly because of the superior cost-effectiveness of CT versus MR scanning in acute stroke, there is no movement towards replacing functional CT by functional MR imaging.[139] Even if MR imaging would become cheaper and more widely accessible in emergency departments, contraindications will prohibit MR imaging in acute cases. These contraindications are frequently unknown in an acute setting, but present in 10% of stroke patients.[7] CT imaging will therefore most probably remain the method of choice in acute stroke imaging in the near future.

Main trends in CT hardware development are increase in acquisition speed and axial coverage. Full brain coverage (≥12 cm) prevents missing infarcts that lie outside the imaged field-of-view (Fig. 1.8). Full brain coverage also enables extraction of clinically relevant NCCT and 4D-CTA from CTP. An even larger coverage (≥30 cm) would allow simultaneous 4D-CTA imaging of both head and neck.[74] This could reduce acquisition time, as well as radiation and contrast agent dose, as compared to separate acquisition of NCCT, CTA, and CTP.

Advances in computational speed as well as in CTP filtering and analysis allow analysis of large-coverage, thin slice perfusion scans in the acute stroke setting. The 5 to 10-fold increase in data may however require the radiologists to be assisted by advanced computer-aided diagnosis (CAD). Like in other (imaging) fields, CAD techniques that integrate and simplify data from multiple sources and along multiple dimensions, go along with the increase in data. The output of CAD in stroke could look like the summary maps as shown in Fig. 1.7d.
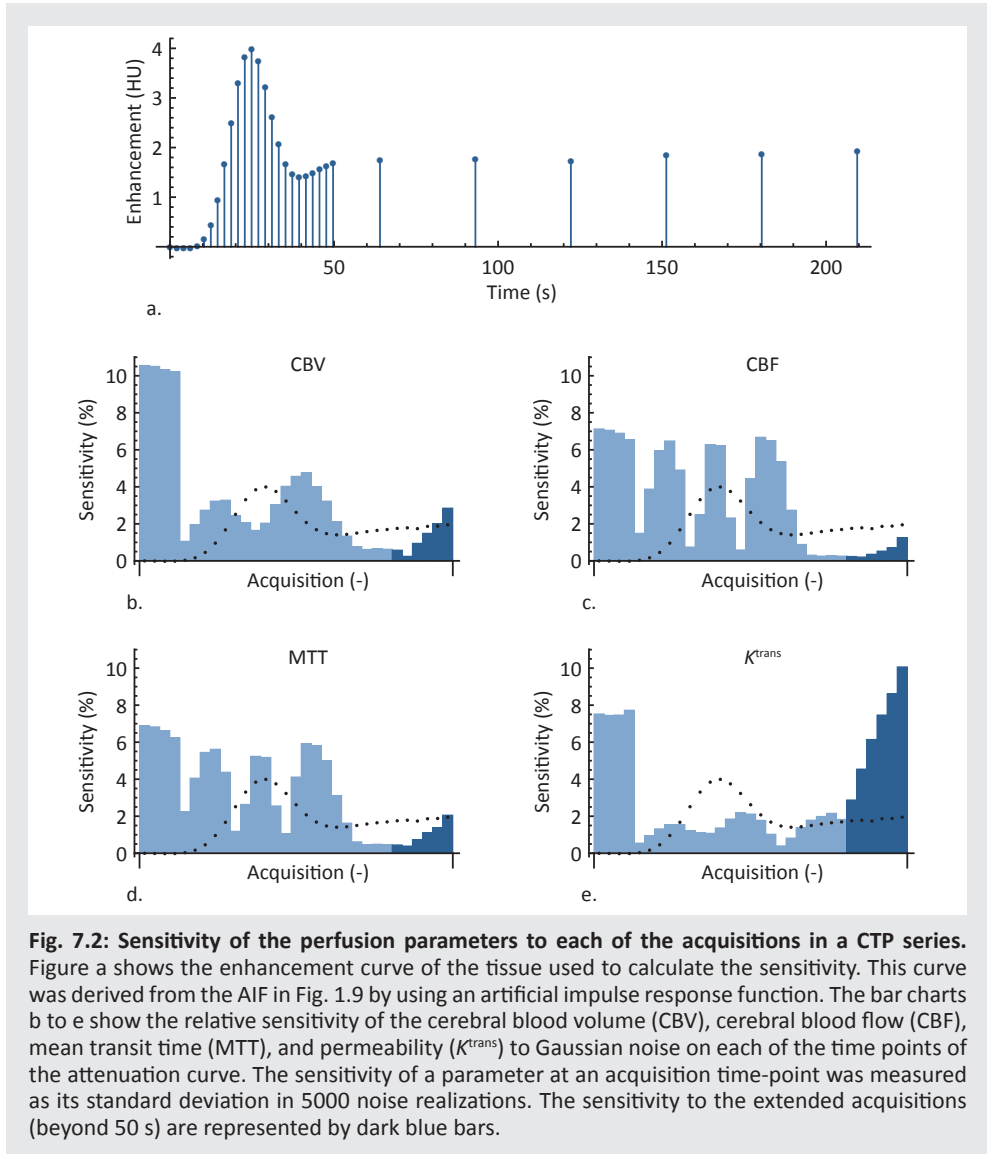
The bilateral filters used in this research share information between acquisitions, which greatly improves upon separate filtering of the acquisitions. Similarly, information between acquisitions could in theory be shared in earlier step in the chain of CTP analysis; i.e. in an iterative reconstruction algorithm tailored to CTP reconstruction. Such an approach would essentially treat the CTP data as a whole, instead of a collection of separately acquired

volumes. Sharing this information could be done without prior knowledge of a perfusion model, as in the bilateral filters, but also by incorporating the model. Analogous to the system-, noise-, and prior-models used in model based iterative reconstruction (MBIR), incorporating prior knowledge about tissue perfusion could further enhance the SNR and reduce artifacts.

Because of performance improvements in CT hardware, spectral CT also regained focus recently. Dual energy imaging was already under investigation in the late 1970s and 1980s, but development stalled due to hardware limitations. This CT imaging technique allows decomposition of a mixture into two materials, and may therefore be used to estimate e.g. the iodine concentration in a voxel.[62] It reduces beam hardening artefacts, and it enhances the contrast between gray and white matter, which in its turn might improve bilateral filtering and reduce radiation dose. It may further reduce radiation dose in CTP as it theoretically allows extraction of enhancement curves without the need for estimating a baseline CT value.

A more recent improvement upon dual-energy CT is single-photon counting CT. Whereas current energy integrating detectors (EIDs) measure the sum of signals from X-ray photons, but photon counting detectors (PCDs) are able to distinguish individual photons. Recent PCDs with energy discrimination capabilities are able to count the number of X-ray photons falling in two to eight energy windows.[135] Novel CT hardware like this could further improve SNR and spatial resolution, reduce artifacts, and give better discrimination between tissue types.

Radiation dose can be reduced by using novel hardware and software as discussed above. But, at an even more fundamental level, the X-ray radiation could be distributed more efficiently in time and in space; i.e. dosage could be increased at certain locations and at certain time points that contribute the most to the result, and lowered in other cases. Recent CT scanners allow dose reduction through automatic tube current modulation. This technique equalizes quantum noise between projections by increasing tube current at radiodense projections and decreasing current at radiolucent projections. Similarly, acquisition frequency and/or tube current could be increased in acquisitions where the information density in the TACs is the highest; i.e. during onset, peak, and decline of the bolus passage, but also during the frames before bolus arrival that are essential for estimating the offset (Fig. 7.2). Some of the latest CT scanners allow programming such a non-uniform acquisition protocol (Fig. 7.3), which is also advised by the AAPM.[1] The proposed model-based methods are suited for such protocols, because they intrinsically enable efficient analysis of irregular sampled TACs as well as alternating tube current by weighing the regression.
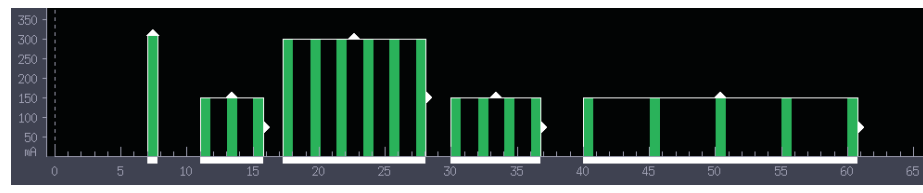
Fig. 7.2: Sensitivity of the perfusion parameters to each of the acquisitions in a CTP series. Figure a shows the enhancement curve of the tissue used to calculate the sensitivity. This curve was derived from the AIF in Fig. 1.9 by using an artificial impulse response function. The bar charts b to e show the relative sensitivity of the cerebral blood volume (CBV), cerebral blood flow (CBF), mean transit time (MTT), and permeability (K^{trans}) to Gaussian noise on each of the time points of the attenuation curve. The sensitivity of a parameter at an acquisition time-point was measured as its standard deviation in 5000 noise realizations. The sensitivity to the extended acquisitions (beyond 50 s) are represented by dark blue bars.

Fig. 7.3: CTP scan protocol with varying tube current and acquisition interval. This is the scan protocol for the Aquilion ONE (Toshiba Medical Systems, Otawara, Japan) as advised by the AAPM. Each green bar represents a volume scan. The tube current is increased for the arterial portion of the scan to provide improved image quality for the perfusion maps. Reprint from AAPM CTP protocol guide.[1]

The technological improvements in CTP software and imaging technology can be exploited in different ways to be in benefit of the patients. On the one hand, improved, but more expensive technology can be used to achieve better image quality, larger coverage, and higher resolution in centers that can afford such equipment. On the other hand, the improvements may lead to the development of more flexible, low cost CTP solutions that are capable of delivering acceptable image quality at a fraction of the price. Such solutions, inspired on e.g. the CereTom small bore CT scanner (Samsung NeuroLogica Corporation, Boston, USA; Fig. 7.1) or the Verity flat-panel cone beam CT (Planmed Oy, Helsinki, Finland), could aid in making acute stroke imaging available in much more emergency departments, raising the level of acute stroke care for a much wider public.

7

Fig. 7.4: A small-bore CT scanner inside a mobile stroke unit. The University of Texas Health Science Center takes the CT scanner to the patient by equipping an ambulance with a CereTom (Samsung NeuroLogica Corporation, Boston, USA).

7.3 CONCLUSION

The proposed model-based method for CT brain perfusion analysis improves on the current commercial and academic state-of-the-art methods. By its simplicity and flexibility, it provides CBF, CBV, and MTT estimates superior to bSVD, and permeability estimates superior to Patlak analysis. Analysis by NLR using a simple, box-shaped IRF was found to be fast enough for use in a time-critical clinical setting. Even model-based quantitative analysis of thin slice CTP scans is feasible, improving the sensitivity in detection of small volume strokes, although this requires revision of currently used thresholds on absolute CBV, CBV, or MTT values for infarct and penumbra delineation. The advances in CTP analysis will in time provide more accurate and more in-depth clinical assessment possibilities for patients with acute ischemic stroke.
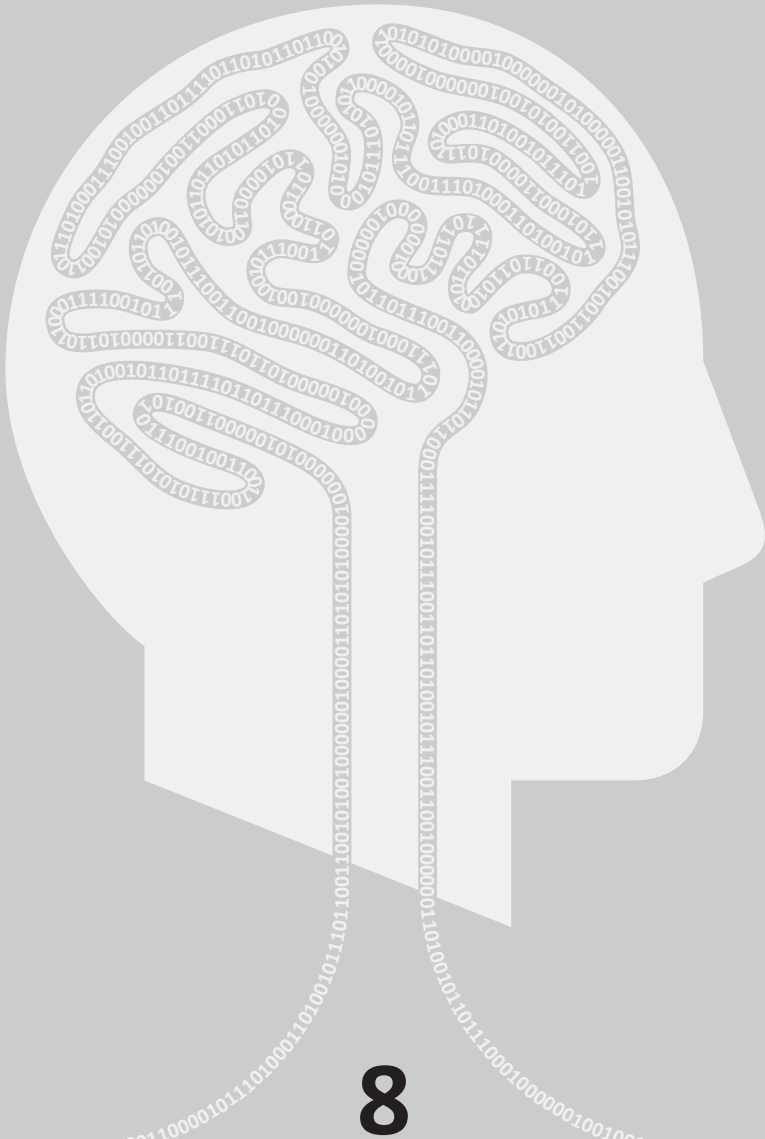
8

References

1. AAPM. Adult Brain Perfusion CT Protocols v1.1. 2012.

2. AAPM. Adult Routine Head CT Protocols v1.1. 2012.

3. Akaike H. A new look at the statistical model identification. *IEEE Trans Autom Control*. 1974;19(6):716-723.

4. Álvarez-Sabín J, Maisterra O, Santamarina E, Kase CS. Factors influencing haemorrhagic transformation in ischaemic stroke. *Lancet Neurol*. 2013;12:689-705.

5. Aviv RI, d Esterre CD, Murphy BD, Hopyan JJ, Buck B, Mallia G, Li V, Zhang L, Symons SP, Lee TY. Hemorrhagic transformation of ischemic stroke: prediction with CT perfusion. *Radiology*. 2009;250(3):867-877.

6. Axel L. A method of calculating brain blood flow with a CT dynamic scanner. *Adv Neurol*. 1981;30:67-71.

7. Ay H, Arsava EM, Johnston SC, Vangel M, Schwamm LH, Furie KL, Koroshetz WJ, Sorensen AG. Clinical-and imaging-based prediction of stroke risk after transient ischemic attack: The CIP model. *Stroke*. 2009;40(1):181-186.

8. Bamford J, Sandercock PAG, Jones L, Warlow C. The natural history of lacunar infarction: the Oxfordshire Community Stroke Project. *Stroke*. 1987;18(3):545-551.

9. Bang OY, Buck BH, Saver JL, Alger JR, Yoon SR, Starkman S, Ovbiagele B, Kim D, Ali LK, Sanossian N, Jahan R, Duckwiler GR, Salamon N, Villablanca JP, Liebeskind DS. Prediction of hemorrhagic transformation after recanalization therapy using T2*-permeability magnetic resonance imaging. *Ann Neurol*. 2007;62(2):170-176.

10. Barber PA, Demchuk AM, Zhang J, Buchan AM. Validity and reliability of a quantitative computed tomography score in predicting outcome of hyperacute stroke before thrombolytic therapy. *Lancet*. 2000;355(9216):1670-1674.

11. Barrett JF, Keat N. Artifacts in CT: recognition and avoidance. *Radiographics*. 2004;24(6):1679-1691.

12. Bauer A, Limburg M, Visser MC. Variation in clinical practice of intravenous thrombolysis in stroke in the Netherlands. *Cerebrovasc Dis Extra*. 2013;3(1):74-77.

13. Bauer AT, Bürgers HF, Rabie T, Marti HH. Matrix metalloproteinase-9 mediates hypoxia-induced vascular leakage in the brain via tight junction rearrangement. *J Cereb Blood Flow Metab*. 2010;30(4):837-848.

14. Bennink E, Riordan AJ, Horsch AD, Dankbaar JW, Velthuis BK, Jong HWAM de. A fast nonlinear regression method for estimating permeability in CT perfusion imaging. *J Cereb Blood Flow Metab*. 2013;33:1743-1751.

15. Berger C, Fiorelli M, Steiner T, Schäbitz W-R, Bozzao L, Bluhmki E, Hacke W, Kummer R von. Hemorrhagic transformation of ischemic brain tissue asymptomatic or symptomatic? *Stroke*. 2001;32(6):1330-1335.

16. Berkhemer OA, Fransen PSS, Beumer D, Berg LA van den, Lingsma HF, Yoo AJ, Schonewille WJ, Vos JA, Nederkoorn PJ, Wermer MJH, Walderveen MAA van, Staals J, Hofmeijer J, Oostayen JA van, Nijeholt GJ Lycklama à, Boiten J, Brouwer PA, Emmer BJ, Bruijn SF de, Dijk LC van, Kappelle LJ, Lo RH, Dijk EJ van, Vries J de, Kort PLM de, Rooij WJJ van, Berg JSP van den, Hasselt BAAM van, Aerden LAM, Dallinga RJ, Visser MC, Bot JCJ, Vroomen PC, Eshghi O, Schreuder THCML, Heijboer RJJ, Keizer K, Tielbeek AV, Hertog HM den, Gerrits DG, Berg-Vos RM van den, Karas GB, Steyerberg EW, Flach HZ, Marquering HA, Sprengers MES, Jenniskens SFM, Beenen LFM, Berg R van den, Koudstaal PJ, Zwam WH van, Roos YBWEM, Lugt A van der, Oostenbrugge RJ van, Majoie CBLM, Dippel DWJ. A randomized trial of intraarterial treatment for acute ischemic stroke. *N Engl J Med*. 2015;372(1):11-20.

17. Biesbroek JM, Niesten JM, Dankbaar JW, Biessels GJ, Velthuis BK, Reitsma JB, Schaaf IC van der. Diagnostic accuracy of CT perfusion imaging for detecting acute ischemic stroke: a systematic review and meta-analysis. *Cerebrovasc Dis*. 2013;35(6):493-501.

8

18. Bisdas S, Hartel M, Cheong LH, Koh TS, Vogl TJ. Prediction of subsequent hemorrhage in acute ischemic stroke using permeability CT imaging and a distributed parameter tracer kinetic model. *J Neuroradiol*. 2007;34(2):101-108.

19. Bivard A, Levi C, Krishnamurthy V, McElduff P, Miteff F, Spratt NJ, Bateman G, Donnan G, Davis S, Parsons M. Perfusion computed tomography to assist decision making for stroke thrombolysis. *Brain*. 2015:awv071.

20. Bivard A, Levi C, Spratt N, Parsons M. Perfusion CT in acute stroke: a comprehensive analysis of infarct and penumbra. *Radiology*. 2013;2:543-550.

21. Bivard A, Spratt N, Levi C, Parsons M. Perfusion computer tomography: imaging and clinical validation in acute ischaemic stroke. *Brain*. 2011;134(11):3408-3416.

22. Borst J, Marquering HA, Beenen LF, Berkhemer OA, Dankbaar JW, Riordan AJ, Majoie CB. Effect of extended CT perfusion acquisition time on ischemic core and penumbra volume estimation in patients with acute ischemic stroke due to a large vessel occlusion. *PLoS ONE*. 2015;10(3):e0119409.

23. Bredno J, Hom J, Schneider T, Wintermark M. Simulation-based validation and arrival-time correction for patlak analyses of perfusion-CT scans. In: *Proc SPIE*. Vol 7262.; 2009:72620G.

24. Bredno J, Olszewski ME, Wintermark M. Simulation model for contrast agent dynamics in brain perfusion scans. *Magn Reson Med*. 2010;64(1):280-290.

25. Brott T, Adams HP, Olinger CP, Marler JR, Barsan WG, Biller J, Spilker J, Holleran R, Eberle R, Hertzberg V. Measurements of acute cerebral infarction: a clinical examination scale. *Stroke*. 1989;20(7):864-870.

26. Burton KR, Dhanoa D, Aviv RI, Moody AR, Kapral MK, Laupacis A. Perfusion CT for selecting patients with acute ischemic stroke for intravenous thrombolytic therapy. *Radiology*. 2015;274(1):103-114.

27. Bushberg JT, Seibert JA, Leidholdt EM, Boone JM. *The Essential Physics of Medical Imaging*. 3rd ed. Lippincott Williams & Wilkins; 2011.

28. Campbell BCV, Christensen S, Levi CR, Desmond PM, Donnan GA, Davis SM, Parsons MW. Cerebral blood flow is the optimal CT perfusion parameter for assessing infarct core. *Stroke*. 2011;42(12):3435-3440.

29. Campbell BCV, Weir L, Desmond PM, Tu HTH, Hand PJ, Yan B, Donnan GA, Parsons MW, Davis SM. CT perfusion improves diagnostic accuracy and confidence in acute ischaemic stroke. *J Neurol Neurosurg Psychiatry*. 2013;84(6):613-618.

30. Costelloe CM, Murphy Jr WA, Gladish GW, Rozner MA. Radiography of pacemakers and implantable cardioverter defibrillators. *Am J Roentgenol*. 2012;199(6):1252-1258.

31. Crone C. Facilitated transfer of glucose from blood into brain tissue. *J Physiol*. 1965;181(1):103-113.

32. Dani KA, Thomas RGR, Chappell FM, Shuler K, MacLeod MJ, Muir KW, Wardlaw JM. Computed tomography and magnetic resonance perfusion imaging in ischemic stroke: definitions and thresholds. *Ann Neurol*. 2011;70(3):384-401.

33. Dankbaar JW, Hom J, Schneider T, Cheng SC, Lau BC, Van Der Schaaf I, Virmani S, Pohlman S, Dillon WP, Wintermark M. Dynamic perfusion CT assessment of the blood-brain barrier permeability: first pass versus delayed acquisition. *Am J Neuroradiol*. 2008;29(9):1671-1676.

34. Dankbaar JW, Hom J, Schneider T, Cheng S-C, Lau BC, Schaaf I van der, Virmani S, Pohlman S, Dillon WP, Wintermark M. Accuracy and anatomical coverage of perfusion CT assessment of the blood-brain barrier permeability: one bolus versus two boluses. *Cerebrovasc Dis*. 2008;26(6):600-605.

35. Das T, Settecase F, Boulos M, Huynh T, d Esterre CD, Symons SP, Zhang L, Aviv RI. Multimodal CT Provides Improved Performance for Lacunar Infarct Detection. *Am J Neuroradiol*. 2015:A4255.

36. Dirks M, Niessen LW, Wijngaarden JDH van, Koudstaal PJ, Franke CL, Oostenbrugge RJ van, Huijsman R, Lingsma MMN Hester F.and Minkman, Dippel DWJ. Promoting thrombolysis in acute ischemic stroke. *Stroke*. 2011;42(5):1325-1330.

37. Eckert B, Küsel T, Leppien A, Michels P, Müller-Jensen A, Fiehler J. Clinical outcome and imaging follow-up in acute stroke patients with normal perfusion CT and normal CT angiography. *Neuroradiology*. 2011;53(2):79-88.

38. Emberson J, Lees KR, Lyden P, Blackwell L, Albers G, Bluhmki E, Brott T, Cohen G, Davis S, Donnan G, Grotta J, Howard G, Kaste M, Koga M, Kummer R von, Lansberg M, Lindley RI, Murray G, Olivot JM, Parsons M, Tilley B, Toni D, Toyoda K, Wahlgren N, Wardlaw J, Whiteley W, Zoppo GJ del, Baigent C, Sandercock P, Hacke W. Effect of treatment delay, age, and stroke severity on the effects of intravenous thrombolysis with alteplase for acute ischaemic stroke: a meta-analysis of individual patient data from randomised trials. *Lancet*. 2014;384(9958):1929-1935.

39. Fahmi F, Beenen LFM, Streekstra GJ, Janssen NY, Jong HW de, Riordan A, Roos YB, Majoie CB, Vanbavel E, Marquering HA. Head movement during CT brain perfusion acquisition of patients with suspected acute ischemic stroke. *Eur J Radiol*. 2013;82(12):2334-2341.

40. Fahmi F, Marquering HA, Streekstra GJ, Beenen LFM, Velthuis BK, VanBavel E, Majoie CB. Differences in CT perfusion summary maps for patients with acute ischemic stroke generated by 2 software packages. *Am J Neuroradiol*. 2012;33(11):2074-2080.

41. Fåhræus R, Lindqvist T. The viscosity of the blood in narrow capillary tubes. *Am J Physiol–Legacy Content*. 1931;96(3):562-568.

42. Fiorella D, Heiserman J, Prenger E, Partovi S. Assessment of the reproducibility of postprocessing dynamic CT perfusion data. *Am J Neuroradiol*. 2004;25(1):97-107.

43. Fischer MA, Donati OF, Reiner CS, Hunziker R, Nanz D, Boss A. Feasibility of semiquantitative liver perfusion assessment by ferucarbotran bolus injection in double-contrast hepatic MRI. *J Magn Reson Imaging*. 2012;36(1):168-176.

44. Furlan AJ. Editorial: Endovascular Therapy for Stroke - It's about Time. *N Engl J Med*. 2015;372(24):2347-2349.

45. Gobbel GT, Fike JR. A deconvolution method for evaluating indicator-dilution curves. *Phys Med Biol*. 1994;39(11):1833.

46. Gomez C. Editorial: Time is brain! *J Stroke Cerebrovasc Dis*. 1993;3:1-2.

47. Hacke W, Furlan AJ, Al-Rawi Y, Davalos A, Fiebach JB, Gruber F, Kaste M, Lipka LJ, Pedraza S, Ringleb PA, Rowley HA, Schneider D, Schwamm LH, Leal JS, Söhngen M, Teal PA, Wilhelm-Ogunbiyi K, Wintermark M, Warach S. Intravenous desmoteplase in patients with acute ischaemic stroke selected by MRI perfusion-diffusion weighted imaging or perfusion CT (DIAS-2): a prospective, randomised, double-blind, placebo-controlled study. *Lancet Neurol*. 2009;8(2):141-150.

48. Hacke W, Kaste M, Bluhmki E, Brozman M, Dávalos A, Guidetti D, Larrue V, Lees KR, Medeghri Z, Machnig T, Schneider D, Kummer R von, Wahlgren N, Toni D. Thrombolysis with alteplase 3 to 4.5 hours after acute ischemic stroke. *N Engl J Med*. 2008;359(13):1317-1329.

49. Hamann GF, Okada Y, Fitridge R, Zoppo GJ del. Microvascular basal lamina antigens disappear during cerebral ischemia and reperfusion. *Stroke*. 1995;26(11):2120-2126.

50. Hana T, Iwama J, Yokosako S, Yoshimura C, Arai N, Kuroi Y, Koseki H, Akiyama M, Hirota K, Ohbuchi H, others. Sensitivity of CT perfusion for the diagnosis of cerebral infarction. *J Med Investig*. 2014;61(1.2):41-45.

51. Hjort N, Wu O, Ashkanian M, Sølling C, Mouridsen K, Christensen S, Gyldensted C, Andersen G, Østergaard L. MRI detection of early blood-brain barrier disruption parenchymal enhancement predicts focal hemorrhagic transformation after thrombolysis. *Stroke*. 2008;39(3):1025-1028.

52. Ho CY, Hussain S, Alam T, Ahmad I, Wu IC, O'Neill DP. Accuracy of CT cerebral perfusion in predicting infarct in the emergency department: lesion characterization on CT perfusion based on commercially available software. *Emerg Radiol*. 2013;20(3):203-212.

53. Hoeven EJRJ van der, Dankbaar JW, Algra A, Vos JA, Niesten JM, Seeters T van, Schaaf IC van der, Schonewille WJ, Kappelle LJ, Velthuis BK. Additional Diagnostic Value of Computed Tomography Perfusion for Detection of Acute Ischemic Stroke in the Posterior Circulation. *Stroke*. 2015;46(4):1113-1115.

8

54. Hom J, Dankbaar J, Schneider T, Cheng SC, Bredno J, Wintermark M. Optimal duration of acquisition for dynamic perfusion CT assessment of blood-brain barrier permeability using the Patlak model. *Am J Neuroradiol*. 2009;30(7):1366-1370.

55. Hom J, Dankbaar JW, Soares BP, Schneider T, Cheng S-C, Bredno J, Lau BC, Smith W, Dillon WP, Wintermark M. Blood-brain barrier permeability assessed by perfusion CT predicts symptomatic hemorrhagic transformation and malignant edema in acute ischemic stroke. *Am J Neuroradiol*. 2011;32(1):41-48.

56. Hopyan J, Ciarallo A, Dowlatshahi D, Howard P, John V, Yeung R, Zhang L, Kim J, MacFarlane G, Lee T-Y, Aviv RI. Certainty of Stroke Diagnosis: Incremental Benefit with CT Perfusion over Noncontrast CT and CT Angiography. *Radiology*. 2010;255(1):142-153.

57. Huisa BN, Neil WP, Schrader R, Maya M, Pereira B, Bruce NT, Lyden PD. Clinical use of computed tomographic perfusion for the diagnosis and prediction of lesion growth in acute ischemic stroke. *J Stroke Cerebrovasc Dis*. 2014;23(1):114-122.

58. Ibaraki M, Ito H, Shimosegawa E, Toyoshima H, Ishigame K, Takahashi K, Kanno I, Miura S. Cerebral vascular mean transit time in healthy humans: a comparative study with PET and dynamic susceptibility contrast-enhanced MRI. *J Cereb Blood Flow Metab*. 2007;27(2):404-413.

59. Ito H, Kanno I, Kato C, Sasaki T, Ishii K, Ouchi Y, Iida A, Okazawa H, Hayashida K, Tsuyuguchi N, Ishii K, Kuwabara Y, Senda M. Database of normal human cerebral blood flow, cerebral blood volume, cerebral oxygen extraction fraction and cerebral metabolic rate of oxygen measured by positron emission tomography with ^{15}O-labelled carbon dioxide or water, carbon monoxide and oxygen: a multicentre study in Japan. *Eur J Nucl Med Mol Imaging*. 2004;31(5):635-643.

60. Jauch EC, Saver JL, Adams HP, Bruno A, Demaerschalk BM, Khatri P, McMullan PW, Qureshi AI, Rosenfield K, Scott PA, Summers DR, Wang DZ, Wintermark M, Yonas H. Guidelines for the early management of patients with acute ischemic stroke a guideline for healthcare professionals from the American Heart Association/American Stroke Association. *Stroke*. 2013;44(3):870-947.

61. Johnson JA, Wilson TA. A model for capillary exchange. *Am J Physiol–Legacy Content*. 1966;210(6):1299-1303.

62. Johnson TRC, Schönberg SO, Fink C, Reiser MF. *Dual Energy CT in Clinical Practice*. 1st ed. Springer Berlin Heidelberg; 2011.

63. Kamalian S, Kamalian S, Konstas AA, Maas MB, Payabvash S, Pomerantz SR, Schaefer PW, Furie KL, González RG, Lev MH. CT perfusion mean transit time maps optimally distinguish benign oligemia from true "at-risk" ischemic penumbra, but thresholds vary by postprocessing technique. *Am J Neuroradiol*. 2012;33(3):545-549.

64. Kamalian S, Kamalian S, Maas MB, Goldmacher GV, Payabvash S, Akbar A, Schaefer PW, Furie KL, Gonzalez RG, Lev MH. CT cerebral blood flow maps optimally correlate with admission diffusion-weighted imaging in acute stroke but thresholds vary by postprocessing platform. *Stroke*. 2011;42(7):1923-1928.

65. Kassner A, Roberts TPL, Moran B, Silver FL, Mikulis DJ. Recombinant tissue plasminogen activator increases blood-brain barrier disruption in acute ischemic stroke: an MR imaging permeability study. *Am J Neuroradiol*. 2009;30(10):1864-1869.

66. Kim EY, Na DG, Kim SS, Lee KH, Ryoo JW, Kim HK. Prediction of hemorrhagic transformation in acute ischemic stroke: role of diffusion-weighted imaging and early parenchymal enhancement. *Am J Neuroradiol*. 2005;26(5):1050-1055.

67. Klein S, Staring M, Murphy K, Viergever MA, Pluim J. Elastix: a toolbox for intensity-based medical image registration. *IEEE T Med Imaging*. 2010;29(1):196-205.

68. Koenig M, Kraus M, Theek C, Klotz E, Gehlen W, Heuser L. Quantitative assessment of the ischemic brain by means of perfusion-related parameters derived from perfusion CT. *Stroke*. 2001;32(2):431-437.

69. Koh TS, Cheong LH, Hou Z, Soh YC. A physiologic model of capillary-tissue exchange for dynamic contrast-enhanced imaging of tumor microcirculation. *IEEE T Bio-Med Eng*. 2003;50(2):159-167.

70. Kolominsky-Rabas PL, Weber M, Gefeller O, Neundoerfer B, Heuschmann PU. Epidemiology of ischemic stroke subtypes according to TOAST criteria incidence, recurrence, and long-term survival in ischemic stroke subtypes: a population-based study. *Stroke*. 2001;32(12):2735-2740.

71. Konstas AA, Goldmakher GV, Lee TY, Lev MH. Theoretic basis and technical implementations of CT perfusion in acute ischemic stroke, part 1: theoretic basis. *Am J Neuroradiol*. 2009;30(4):662-668.

72. Konstas AA, Goldmakher GV, Lee TY, Lev MH. Theoretic basis and technical implementations of CT perfusion in acute ischemic stroke, part 2: technical implementations. *Am J Neuroradiol*. 2009;30(5):885-892.

73. Konstas AA, Lev MH. CT perfusion imaging of acute stroke: the need for arrival time, delay insensitive, and standardized postprocessing algorithms? *Radiology*. 2010;254(1):22-25.

74. Kortman HGJ, Smit EJ, Oei MTH, Manniesing R, Prokop M, Meijer FJA. 4D-CTA in neurovascular disease: a review. *Am J Neuroradiol*. 2014;36(6):1026-1033.

75. Krejza J, Arkuszewski M, Kasner SE, Weigele J, Ustymowicz A, Hurst RW, Cucchiara BL, Messe SR. Carotid artery diameter in men and women and the relation to body and neck size. *Stroke*. 2006;37(4):1103-1105.

76. Kudo K, Christensen S, Sasaki M, Østergaard L, Shirato H, Ogasawara K, Wintermark M, Warach S. Accuracy and reliability assessment of CT and MR perfusion analysis software using a digital phantom. *Radiology*. 2013;267(1):201-211.

77. Kudo K, Sasaki M, Ogasawara K, Terae S, Ehara S, Shirato H. Difference in tracer delay-induced effect among deconvolution algorithms in CT perfusion analysis: quantitative evaluation with digital phantoms. *Radiology*. 2009;251(1):241-249.

78. Kudo K, Sasaki M, Yamada K, Momoshima S, Utsunomiya H, Shirato H, Ogasawara K. Differences in CT perfusion maps generated by different commercial software: quantitative analysis by using identical source data of acute stroke patients. *Radiology*. 2010;254(1):200-209.

79. Lansberg MG, Straka M, Kemp S, Mlynash M, Wechsler LR, Jovin TG, Wilder MJ, Lutsep HL, Czartoski TJ, Bernstein RA, Chang CWJ, Warach S, Fazekas F, Inoue M, Tipirneni A, Hamilton SA, Zaharchuk G, Marks MP, Bammer R, Albers GW. MRI profile and response to endovascular reperfusion after stroke (DEFUSE 2): a prospective cohort study. *Lancet Neurol*. 2012;11(10):860-867.

80. Larson KB, Markham J, Raichle ME. Tracer-kinetic models for measuring cerebral blood flow using externally detected radiotracers. *J Cereb Blood Flow Metab*. 1987;7(4):443-463.

81. Larsson HBW, Courivaud F, Rostrup E, Hansen AE. Measurement of brain perfusion, blood volume, and blood-brain barrier permeability, using dynamic contrast-enhanced T1-weighted MRI at 3 tesla. *Magn Reson Med*. 2009;62(5):1270-1281.

82. Latour LL, Kang D-W, Ezzeddine MA, Chalela JA, Warach S. Early blood–brain barrier disruption in human focal brain ischemia. *Ann Neurol*. 2004;56(4):468-477.

83. Lawrence KSS, Lee TY. An adiabatic approximation to the tissue homogeneity model for water exchange in the brain: I. Theoretical derivation. *J Cereb Blood Flow Metab*. 1998;18(12):1365-1377.

84. Lee IH, You JH, Lee JY, Whang K, Kim MS, Kim YJ, Lee MS. Accuracy of the detection of infratentorial stroke lesions using perfusion CT: an experimenter-blinded study. *Neuroradiology*. 2010;52(12):1095-1100.

85. Lee TY, Purdie TG, Stewart E, others. CT imaging of angiogenesis. *Q J Nucl Med*. 2003;47(3):171-187.

8

86. Leenders KL, Perani D, Lammertsma AA, Heather JD, Buckingham P, Jones T, Healy MJR, Gibbs JM, Wise RJS, Hatazawa J, Herold S, Beaney RP, Brooks DJ, Spinks T, Rhodes C, Frackowiak RSJ. Cerebral blood flow, blood volume and oxygen utilization. *Brain*. 1990;113(1):27-47.

87. Lin K, Do KG, Ong P, Shapiro M, Babb JS, Siller KA, Pramanik BK. Perfusion CT improves diagnostic accuracy for hyperacute ischemic stroke in the 3-hour window: study of 100 patients with diffusion MRI confirmation. *Cerebrovasc Dis*. 2009;28(1):72-79.

88. Lin K, Kazmi KS, Law M, Babb J, Peccerelli N, Pramanik BK. Measuring elevated microvascular permeability and predicting hemorrhagic transformation in acute ischemic stroke using first-pass dynamic perfusion CT imaging. *Am J Neuroradiol*. 2007;28(7):1292-1298.

89. Marler JR, Brott T, Broderick J, Kothari R, Odonoghue M, Barsan W, Tomsick T, Spilker J, Miller R, Sauerbeck L, others. Tissue-plasminogen activator for acute ischemic stroke. *N Engl J Med*. 1995;333(24):1581-1587.

90. Maruya J, Yamamoto K, Ozawa T, Nakajima T, Sorimachi T, Kawasaki T, Tanaka R. Simultaneous multi-section perfusion CT and CT angiography for the assessment of acute ischemic stroke. *Acta Neurochir (Wien)*. 2005;147(4):383-392.

91. Mendrik AM, Vonken E, Ginneken B van, Jong HW de, Riordan A, Seeters T van, Smit EJ, Viergever MA, Prokop M. TIPS bilateral noise reduction in 4D CT perfusion scans produces high-quality cerebral blood flow maps. *Phys Med Biol*. 2011;56:3857-3872.

92. Merino JG, Warach S. Imaging of acute stroke. *Nat Rev Neurol*. 2010;6(10):560-571.

93. Miles KA, Hayball M, Dixon AK. Colour perfusion imaging: a new application of computed tomography. *Lancet*. 1991;337(8742):643-645.

94. Mishra NK, Albers GW, Davis SM, Donnan GA, Furlan AJ, Hacke W, Lees KR. Mismatch-based delayed thrombolysis a meta-analysis. *Stroke*. 2010;41(1):e25–e33.

95. Mlynash M, Eyngorn I, Bammer R, Moseley M, Tong DC. Automated method for generating the arterial input function on perfusion-weighted MR imaging: validation in patients with stroke. *Am J Neuroradiol*. 2005;26(6):1479-1486.

96. Mohr JP, Grotta JC, Wolf PA, Moskowitz MA, Mayberg MR, Kummer R von. *Stroke: Pathophysiology, Diagnosis, and Management*. 5th ed. Elsevier Health Sciences; 2011.

97. Motulsky HJ, Ransnas LA. Fitting curves to data using nonlinear regression: a practical and nonmathematical review. *FASEB J*. 1987;1(5):365-374.

98. Müller HR, Brunhölzl C, Radü EW, Buser M. Sex and side differences of cerebral arterial caliber. *Neuroradiology*. 1991;33(3):212-216.

99. Murphy BD, Fox AJ, Lee DH, Sahlas DJ, Black SE, Hogan MJ, Coutts SB, Demchuk AM, Goyal M, Aviv RI, Symons S, Gulka IB, Beletsky V, Pelz D, Chan RK, Lee T-Y. White matter thresholds for ischemic penumbra and infarct core in patients with acute stroke: CT perfusion study. *Radiology*. 2008;247(3):818-825.

100. Murphy BD, Fox AJ, Lee DH, Sahlas DJ, Black SE, Hogan MJ, Coutts SB, Demchuk AM, Goyal M, Aviv RI, Symons S, Gulka IB, Beletsky V, Pelz D, Hachinski V, Chan R, Lee T-Y. Identification of penumbra and infarct in acute ischemic stroke using computed tomography perfusion-derived blood flow and blood volume measurements. *Stroke*. 2006;37(7):1771-1777.

101. Nambu K, Takehara R, Terada T. A method of regional cerebral blood perfusion measurement using dynamic CT with an iodinated contrast medium. *Acta Neurol Scand*. 1996;93(s166):28-31.

102. Nelder JA, Mead R. A simplex method for function minimization. *The computer journal*. 1965;7(4):308-313.

103. Norman D, Axel L, Berninger WH, Edwards MS, Cann CE, Redington RW, Cox L. Dynamic computed tomography of the brain: techniques, data analysis, and applications. *Am J Neuroradiol*. 1981;2(1):1-12.

104. Norrving B. Long-term prognosis after lacunar infarction. *Lancet Neurol*. 2003;2(4):238-245.

105. Nowinski WL, Gupta V, Qian G, He J, Poh LE, Ambrosius W, Chrzan RM, Polonara G, Mazzoni C, Mol M, Salvolini L, Walecki J, Salvolini U, Urbanik A, Kazmierski R. Automatic detection, localization, and volume estimation of ischemic infarcts in noncontrast computed tomographic scans: method and preliminary results. *Invest Radiol*. 2013;48(9):661-670.

106. Oosterbroek J, Bennink E, Dankbaar JW, Horsch AD, Viergever MA, Velthuis BK, Jong HWAM de. Predicting stroke outcome using DCE-CT measured blood velocity. In: *SPIE Medical Imaging*. International Society for Optics and Photonics; 2015:94170I.

107. Oosterbroek J, Bennink E, Philippens MEP, Raaijmakers CPJ, Viergever MA, Jong HWAM de. Comparison of DCE-CT models for quantitative evaluation of Ktrans in larynx tumors. *Phys Med Biol*. 2015;60(9):3759-3773.

108. Pantoni L, Fierini F, Poggesi A. Thrombolysis in acute stroke patients with cerebral small vessel disease. *Cerebrovasc Dis*. 2014;37(1):5-13.

109. Patlak CS, Blasberg RG, Fenstermacher JD. Graphical evaluation of blood-to-brain transfer constants from multiple-time uptake data. *J Cereb Blood Flow Metab*. 1983;3(1):1-7.

110. Patlak CS, Blasberg RG. Graphical evaluation of blood-to-brain transfer constants from multiple-time uptake data. Generalizations. *J Cereb Blood Flow Metab*. 1985;5(4):584-590.

111. Pennica D, Holmes WE, Kohr WJ, Harkins RN, Vehar GA, Ward CA, Bennett WF, Yelverton E, Seeburg PH, Heyneker HL, Goeddel DV, Collen D. Cloning and expression of human tissue-type plasminogen activator cDNA in E. coli. *Nature*. 1983;301:214-221.

112. Pexman JHW, Barber PA, Hill MD, Sevick RJ, Demchuk AM, Hudon ME, Hu WY, Buchan AM. Use of the alberta stroke program early CT score (aspects) for assessing ct scans in patients with acute stroke. *Am J Neuroradiol*. 2001;22(8):1534-1542.

113. Potter GM, Marlborough FJ, Wardlaw JM. Wide variation in definition, detection, and description of lacunar lesions on imaging. *Stroke*. 2011;42(2):359-366.

114. Press WH, Teukolsky SA, Vetterling WT, Flannery BP. *Numerical Recipes: The Art of Scientific Computing*. 3rd ed. Cambridge University Press; 2007.

115. Rajajee V, Kidwell C, Starkman S, Ovbiagele B, Alger J, Villablanca P, Saver JL. Diagnosis of lacunar infarcts within 6 hours of onset by clinical and CT criteria versus MRI. *J Neuroimaging*. 2008;18(1):66-72.

116. Rempp KA, Brix G, Wenz F, Becker CR, Gückel F, Lorenz WJ. Quantification of regional cerebral blood flow and volume with dynamic susceptibility contrast-enhanced MR imaging. *Radiology*. 1994;193(3):637-641.

117. Renkin EM. Transport of potassium-42 from blood to tissue in isolated mammalian skeletal muscles. *Am J Physiol–Legacy Content*. 1959;197(6):1205-1210.

118. Riordan AJ, Bennink E, Viergever MA, Velthuis BK, Dankbaar JW, Jong HWAM de. CT brain perfusion protocol to eliminate the need for selecting a venous output function. *Am J Neuroradiol*. 2013;34(7):1353-1358.

119. Roberts HC, Roberts TPL, Brasch RC, Dillon WP. Quantitative measurement of microvascular permeability in human brain tumors achieved using dynamic contrast-enhanced MR imaging: correlation with histologic grade. *Am J Neuroradiol*. 2000;21(5):891-899.

120. Sabarudin A, Subramaniam C, Sun Z. Cerebral CT angiography and CT perfusion in acute stroke detection: a systematic review of diagnostic value. *Quant Imaging Med Surg*. 2014;4(4):282.

121. Sacco S, Marini C, Totaro R, Russo T, Cerone D, Carolei A. A population-based study of the incidence and prognosis of lacunar stroke. *Neurology*. 2006;66(9):1335-1338.

122. Santos EMM, Yoo AJ, Beenen LF, Berkhemer OA, Blanken MD den, Wismans C, Niessen WJ, Majoie CB, Marquering HA. Observer variability of absolute and relative thrombus density measurements in patients with acute ischemic stroke. *Neuroradiology*. 2015:1-7.

123. Sasaki M, Kudo K, Ogasawara K, Fujiwara S. Tracer delay-insensitive algorithm can improve reliability of CT perfusion imaging for cerebrovascular steno-occlusive disease: comparison with quantitative single-photon emission CT. *Am J Neuroradiol*. 2009;30(1):188-193.

8

124. Sawada Y, Patlak CS, Blasberg RG. Kinetic analysis of cerebrovascular transport based on indicator diffusion technique. *Am J Physiol–Heart C*. 1989;256(3):H794–H812.

125. Schaaf I van der, Vonken EJ, Waaijer A, Velthuis B, Quist M, Osch T van. Influence of partial volume on venous output and arterial input function. *Am J Neuroradiol*. 2006;27(1):46-50.

126. Schaefer PW, Barak ER, Kamalian S, Gharai LR, Schwamm L, Gonzalez RG, Lev MH. Quantitative assessment of core/penumbra mismatch in acute stroke CT and MR perfusion imaging are strongly correlated when sufficient brain volume is imaged. *Stroke*. 2008;39(11):2986-2992.

127. Schaefer PW, Roccatagliata L, Ledezma C, Hoh B, Schwamm LH, Koroshetz W, Gonzalez RG, Lev MH. First-pass quantitative CT perfusion identifies thresholds for salvageable penumbra in acute stroke patients treated with intra-arterial therapy. *Am J Neuroradiol*. 2006;27(1):20-25.

128. Schneider T, Hom J, Bredno J, Dankbaar JW, Cheng SC, Wintermark M. Delay correction for the assessment of blood-brain barrier permeability using first-pass dynamic perfusion CT. *Am J Neuroradiol*. 2011;32(7):E134–E138.

129. Seeters T van, Biessels GJ, Kappelle LJ, Schaaf IC van der, Dankbaar JW, Horsch AD, Niesten JM, Luitse MJ, Majoie CB, Vos JA, Schonewille WJ, Walderveen MA van, Wermer MJ, Duijm LE, Keizer K, Bot JC, Visser MC, Lugt A van der, Dippel DW, Kesselring FO, Hofmeijer J, Lycklama Nijeholt GJ, Boiten J, Rooij WJ van, Kort PL de, Roos YB, Dijk EJ van, Pleiter CC, Mali WP, Graaf Y van der, Velthuis BK. The Prognostic Value of CT Angiography and CT Perfusion in Acute Ischemic Stroke. *Cerebrovasc Dis*. 2015;40(5–6):258-269.

130. Seeters T van, Biessels GJ, Schaaf IC van der, Dankbaar JW, Horsch AD, Luitse MJA, Niesten JM, Mali WPTM, Kappelle LJ, Graaf Y van der, Velthuis BK. Prediction of outcome in patients with suspected acute ischaemic stroke with CT perfusion and CT angiography: the Dutch acute stroke trial (DUST) study protocol. *BMC Neurol*. 2014;14(1):37.

131. Shobha N, Fang J, Hill MD. Do lacunar strokes benefit from thrombolysis? Evidence from the Registry of the Canadian Stroke Network. *Int J Stroke*. 2013;8(A100):45-49.

132. Sourbron SP, Buckley DL. Tracer kinetic modelling in MRI: estimating perfusion and capillary permeability. *Phys Med Biol*. 2012;57:R1–R33.

133. Stapf C, Hofmeister C, Hartmann A, Marx P, Mast H. Predictive value of clinical lacunar syndromes for lacunar infarcts onmagnetic resonance brain imaging. *Acta Neurol Scand*. 2000;101(1):13-18.

134. Stewart GN. Researches on the circulation time in organs and on the influences which affect it. *J Physiol*. 1893;15(1-2):1-89.

135. Taguchi K, Iwanczyk JS. Vision 20/20: Single photon counting x-ray detectors in medical imaging. *Med Phys*. 2013;40(10):100901.

136. Tofts PS, Brix G, Buckley DL, Evelhoch JL, Henderson E, Knopp MV, Larsson HBW, Lee TY, Mayr NA, Parker GJM, Port RE, Taylor J, Weisskoff RM. Estimating kinetic parameters from dynamic contrast-enhanced T1-weighted MRI of a diffusable tracer: standardized quantities and symbols. *J Magn Reson Imaging*. 1999;10(3):223-232.

137. Tomasi C, Manduchi R. Bilateral filtering for gray and color images. In: *Proc. ICCV*. IEEE; 1998:839-846.

138. Wang X, Tsuji K, Lee S-R, Ning M, Furie KL, Buchan AM, Lo EH. Mechanisms of hemorrhagic transformation after tissue plasminogen activator reperfusion therapy for ischemic stroke. *Stroke*. 2004;35(suppl I):2726-2730.

139. Wardlaw J, Brazzelli M, Miranda H, Chappell F, McNamee P, Scotland G, Quayyum Z, Martin D, Shuler K, Sandercock P, Dennis M. An assessment of the cost-effectiveness of magnetic resonance, including diffusion-weighted imaging, in patients with transient ischaemic attack and minor stroke: a systematic review, meta-analysis and economic evaluation. *Health Technol Assess*. 2014;18(27).

140. Wardlaw JM, Murray V, Berge E, Zoppo GJ del. Thrombolysis for acute ischaemic stroke. *Cochrane Database Syst Rev*. 2014;7:CD000213.

141. Whisnant JP, Basford JR, Bernstein EF, Cooper ES, Dyken ML, Easton D, Little JR, Marler JR, Millikan CH, Petito CK, Price TR, Raichle ME, Robertson JT, Thiele B, Walker MD, Zimmerman RA. Classification of cerebrovascular diseases: III. Special report from the National Institute of Neurological Disorders and Stroke. *Stroke*. 1990;21(4):637-676.

142. Whiteley WN, Slot KB, Fernandes P, Sandercock P, Wardlaw J. Risk factors for intracranial hemorrhage in acute ischemic stroke patients treated with recombinant tissue plasminogen activator a systematic review and meta-analysis of 55 studies. *Stroke*. 2012;43(11):2904-2909.

143. Wiesmann M. CT perfusion of the brain: the basics of the method and interpreting images. *Visions Journal (Online)*. 2006;9:6-9.

144. Willemink MJ, Jong PA de, Leiner T, Heer LM de, Nievelstein RAJ, Budde RPJ, Schilham AMR. Iterative reconstruction techniques for computed tomography part 1: technical principles. *Eur Radiol*. 2013;23(6):1623-1631.

145. Willemink MJ, Takx RAP, Jong PA de, Budde RPJ, Bleys RLAW, Das M, Wildberger JE, Prokop M, Buls N, Mey J de, Leiner T, Schilham AMR. Computed tomography radiation dose reduction: effect of different iterative reconstruction algorithms on image quality. *J Comput Assist Tomogr*. 2014;38(6):815-823.

146. Wintermark M, Fischbein NJ, Smith WS, Ko NU, Quist M, Dillon WP. Accuracy of dynamic perfusion CT with deconvolution in detecting acute hemispheric stroke. *Am J Neuroradiol*. 2005;26(1):104-112.

147. Wintermark M, Flanders AE, Velthuis B, Meuli R, Leeuwen M van, Goldsher D, Pineda C, Serena J, Schaaf I van der, Waaijer A, Anderson J, Nesbit G, Gabriely I, Medina V, Quiles A, Pohlman S, Quist M, Schnyder P, Bogousslavsky J, Dillon WP, Pedraza S. Perfusion-CT assessment of infarct core and penumbra receiver operating characteristic curve analysis in 130 patients suspected of acute hemispheric stroke. *Stroke*. 2006;37(4):979-985.

148. Wintermark M, Maeder P, Verdun FR, Thiran J-P, Valley J-F, Schnyder P, Meuli R. Using 80 kVp versus 120 kVp in perfusion CT measurement of regional cerebral blood flow. *Am J Neuroradiol*. 2000;21(10):1881-1884.

149. Wintermark M, Reichhart M, Cuisenaire O, Maeder P, Thiran J-P, Schnyder P, Bogousslavsky J, Meuli R. Comparison of admission perfusion computed tomography and qualitative diffusion- and perfusion-weighted magnetic resonance imaging in acute stroke patients. *Stroke*. 2002;33(8):2025-2031.

150. Wintermark M, Reichhart M, Thiran J-P, Maeder P, Chalaron M, Schnyder P, Bogousslavsky J, Meuli R. Prognostic accuracy of cerebral blood flow measurement by perfusion computed tomography, at the time of emergency room admission, in acute stroke patients. *Ann Neurol*. 2002;51(4):417-432.

151. Wintermark M, Thiran J-P, Maeder P, Schnyder P, Meuli R. Simultaneous measurement of regional cerebral blood flow by perfusion CT and stable xenon CT: a validation study. *Am J Neuroradiol*. 2001;22(5):905-914.

152. Wu O, Østergaard L, Weisskoff RM, Benner T, Rosen BR, Sorensen AG. Tracer arrival timing-insensitive technique for estimating flow in MR perfusion-weighted imaging using singular value decomposition with a block-circulant deconvolution matrix. *Magn Reson Med*. 2003;50(1):164-174.

153. Yonas H, Darby WM, Marks EC, Durham SR, Maxwell C. CBF measured by Xe-CT: approach to analysis and normal values. *J Cereb Blood Flow Metab*. 1991;11(5):716-725.
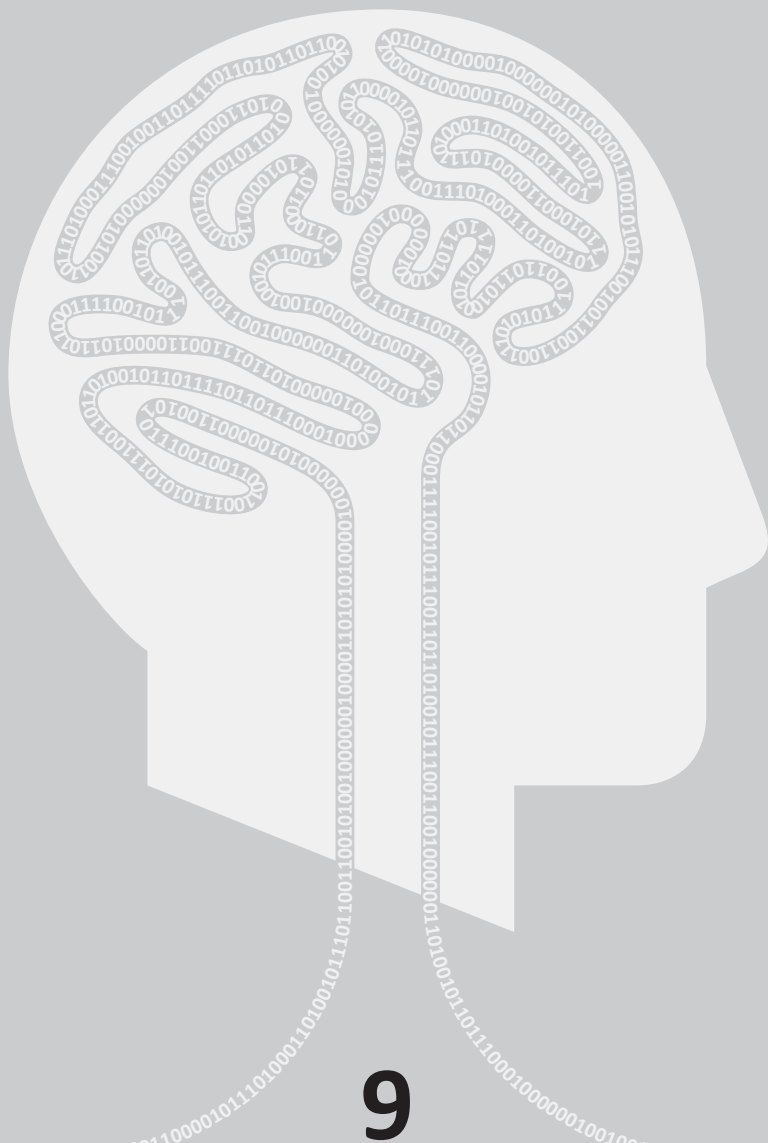
8

9

Samenvatting in het Nederlands

Patiënten met een acuut herseninfarct zijn gebaat bij een snelle behandeling. Hoe eerder stolsel-oplossende medicatie wordt toegediend, hoe groter de kans op goed herstel. In enkele gevallen kan deze behandeling echter als bijwerking een hersenbloeding veroorzaken. Als de behandeling te lang wordt uitgesteld, wordt de kans op goed herstel kleiner dan de kans op het veroorzaken van een bloeding. De verhouding tussen deze kansen hangt echter niet alleen af van de tijd, maar ook van de locatie en de omvang van de infarctkern en van het omringende aangedane weefsel. Bij het vaststellen hiervan speelt medische beeldvorming een belangrijke rol.

Bij het stellen van een diagnose bij patiënten met aanwijzingen voor een beroerte gaat de voorkeur voor de beeldvormende techniek meestal uit naar CT. Deze techniek is namelijk praktisch in gebruik en in de meeste ziekenhuizen is er een CT scanner beschikbaar voor acute situaties. Nadat een hersenbloeding is uitgesloten, die juist verergerd zal worden door het toedienen van stolsel-oplossende medicatie, kan met een aansluitende perfusie CT-scan (CTP) het infarct in beeld worden gebracht. CTP kan dus helpen bij het selecteren van patiënten voor behandeling. De huidige methoden voor het analyseren van deze perfusiescans hebben echter vele tekortkomingen en halen zeker niet het onderste uit de kan. Het onderzoek in dit proefschrift is gericht op het ontwikkelen van nieuwe kwantitatieve analysemethoden voor CTP. Deze methoden zouden de effectiviteit van CTP in het selecteren van patiënten kunnen verbeteren.

Tijdens een CTP-scan wordt er gedurende 50 seconden, met intervallen van 2 seconden, herhaaldelijk een 3D afbeelding van de hersenen gemaakt. Doordat er aan het begin een bolus met contrastmiddel wordt geïnjecteerd, lichten de bloedvaten en het hersenweefsel gedurende de scan als het ware op, om daarna weer uit te doven (Fig. 9.1). Door het 'oplichten en uitdoven' te analyseren is het mogelijk om van deze scan kwantitatieve afbeeldingen te maken van bijvoorbeeld het bloedvolume, het debiet en de doorstroomtijd in het hersenweefsel (Fig. 9.2). Door nog langer dan 50 seconden te scannen is het zelfs mogelijk om een meting te doen aan het 'lekken' van bloed uit de kleinste bloedvaatjes. Deze meting zou kunnen helpen om het risico op een bloeding, als bijwerking van de behandeling, beter in te schatten. Doordat de stralingsbelasting voor de patiënt niet te hoog mag zijn, hebben de scans relatief veel ruis, wat de analyse bemoeilijkt.
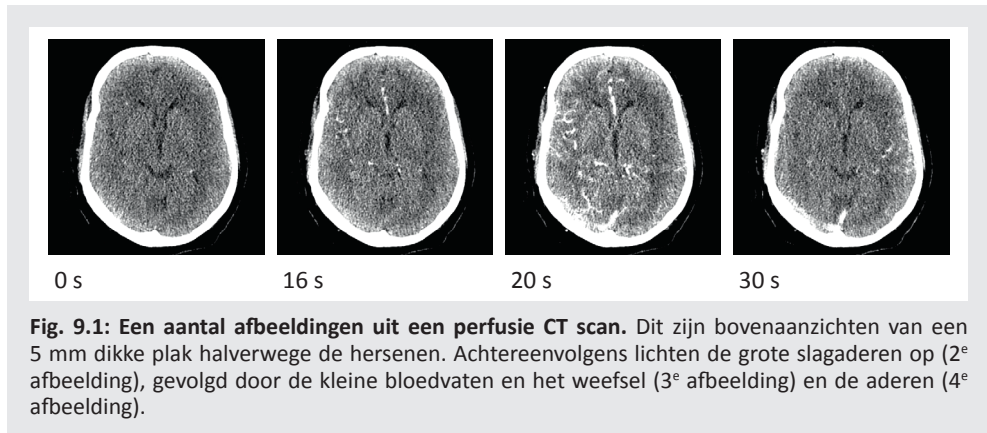
9

| 0 s | 16 s | 20 s | 30 s |

Fig. 9.1: Een aantal afbeeldingen uit een perfusie CT scan. Dit zijn bovenaanzichten van een 5 mm dikke plak halverwege de hersenen. Achtereenvolgens lichten de grote slagaderen op (2^e afbeelding), gevolgd door de kleine bloedvaten en het weefsel (3^e afbeelding) en de aderen (4^e afbeelding).
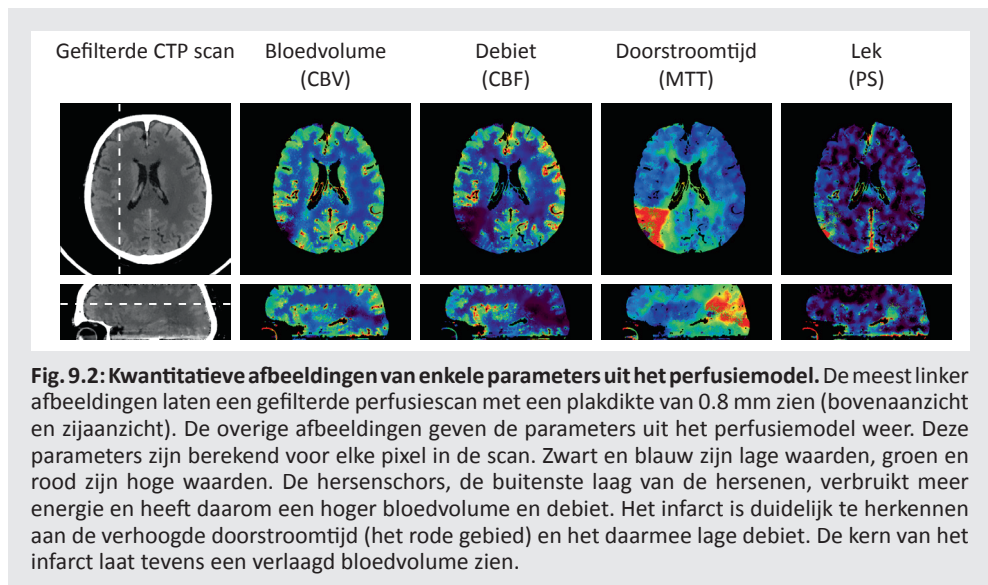
In dit proefschrift wordt een CTP-analyse methode gepresenteerd die de perfusie van het hersenweefsel (het 'oplichten en uitdoven' in de scan) beschrijft aan de hand van een simpel doch doeltreffend wiskundig model. De bovengenoemde perfusiewaarden, zoals het bloedvolume, zijn parameters in dit model. In **hoofdstuk 2** werd met behulp van een computersimulatie en klinische scans gedemonstreerd dat het gebruik van deze methode betere resultaten oplevert dan de huidige academische en commerciële methoden. Deze academische en commerciële methoden maken geen gebruik van een perfusiemodel.

De 'lek' uit de kleine bloedvaatjes wordt doorgaans gemeten met een simpele methode die geen rekening houdt met het debiet en de doorstroomtijd in het hersenweefsel. Het gebruik van een complex wiskundig perfusiemodel, dat al deze parameters wél beschrijft, zou de nauwkeurigheid van de meting kunnen verbeteren. Een dergelijke methode is echter nogal tijdrovend en daarom niet geschikt voor gebruik in acute situaties. In **hoofdstuk 3** werd een versimpeld model geïntroduceerd dat op een makkelijkere en dus snellere manier toegepast kan worden. Aan de hand van computersimulaties en klinische scans werd bewezen dat het gebruik van dit model inderdaad nauwkeuriger is en bovendien snel genoeg voor klinische toepassing.

In **hoofdstuk 4** is het versimpelde model uit hoofdstuk 3 gebruikt om, aan de hand van de 'lek', een uitspraak te doen over de kans op het krijgen van een bloeding na behandeling. Hiervoor zijn de metingen aan 20 CTP scans van patiënten die na de behandeling een bloeding kregen, vergeleken met 40 CTP scans van patiënten die geen bloeding kregen. Het bleek dat een lek-parameter uit het nieuwe, versimpelde model het grootste verschil liet zien tussen beide groepen. Desondanks is de voorspellende waarde van deze parameter helaas nog aan de lage kant.

3D CTP scans bestaan uit stapeling van 2D plakken. In **hoofdstuk 5** is er gekeken naar de invloed van de plakdikte en daarmee ook het aantal plakken. Ondanks dat moderne CT scanners plakken kunnen maken van minder dan 1 mm dikte, wordt er in de huidige klinische

werkwijze een plakdikte van 5 of zelfs 10 mm gebruikt. Dikkere plakken zorgen namelijk voor minder data en tevens een lager ruisniveau. Door gebruik te maken van slimme filters en betere perfusie-analyse methoden, kan echter hetzelfde ruisniveau worden bereikt op dunnere plakken (Fig. 9.2). Dit geeft scherpere afbeeldingen en betere resultaten. Hierdoor is het wellicht mogelijk om kleinere infarcten waar te nemen. De studie in hoofdstuk 5 liet zien dat deze werkwijze goed mogelijk is, maar dat het wel een verschuiving in de meetresultaten veroorzaakt. Deze verschuiving zorgt weliswaar voor resultaten die realistischer zijn, maar om ze te kunnen gebruiken is het noodzakelijk om de huidige klinische drempelwaarden op deze parameters te herzien.

| Gefilterde CTP scan | Bloedvolume (CBV) | Debiet (CBF) | Doorstroomtijd (MTT) | Lek (PS) |

Fig. 9.2: Kwantitatieve afbeeldingen van enkele parameters uit het perfusiemodel. De meest linker afbeeldingen laten een gefilterde perfusiescan met een plakdikte van 0.8 mm zien (bovenaanzicht en zijaanzicht). De overige afbeeldingen geven de parameters uit het perfusiemodel weer. Deze parameters zijn berekend voor elke pixel in de scan. Zwart en blauw zijn lage waarden, groen en rood zijn hoge waarden. De hersenschors, de buitenste laag van de hersenen, verbruikt meer energie en heeft daarom een hoger bloedvolume en debiet. Het infarct is duidelijk te herkennen aan de verhoogde doorstroomtijd (het rode gebied) en het daarmee lage debiet. De kern van het infarct laat tevens een verlaagd bloedvolume zien.

Dat het gebruik van de werkwijze met dunne plakken leidt tot een verbetering van de detectie van kleine infarcten, werd bewezen in **hoofdstuk 6**. In dit onderzoek zijn, in willekeurige volgorde, 41 CTP scans van patiënten met een zeer klein infarct en 82 controlescans bekeken. Zowel met 0.8 mm als met 4.8 mm plakdikte. Op de 0.8 mm scans bleek de radioloog 66% van de infarcten te hebben gevonden, tegenover slechts 44% op de 4.8 mm scans. Het percentage terecht negatieve bevindingen lag in beide gevallen rond de 90%.

Er bestaat twijfel of CTP in zijn huidige vorm wel voldoende toegevoegde waarde heeft bij het behandelen van een acuut herseninfarct. Samengevat kan er uit dit werk echter geconcludeerd worden dat deze beeldvormende techniek de potentie heeft om nauwkeuriger en kwantitatiever te worden dan dat hij nu is. De uitdaging zit in het verkrijgen van goede resultaten met een minimale stralingsbelasting voor de patiënt. Door de toename in kennis én in computerkracht is het mogelijk om geavanceerde, modelgebaseerde analysemethoden

9

te gebruiken die wél het onderste uit de kan weten te halen. Al deze verbeteringen zullen in de loop van de tijd bijdragen aan een betere behandeling van herseninfarcten.
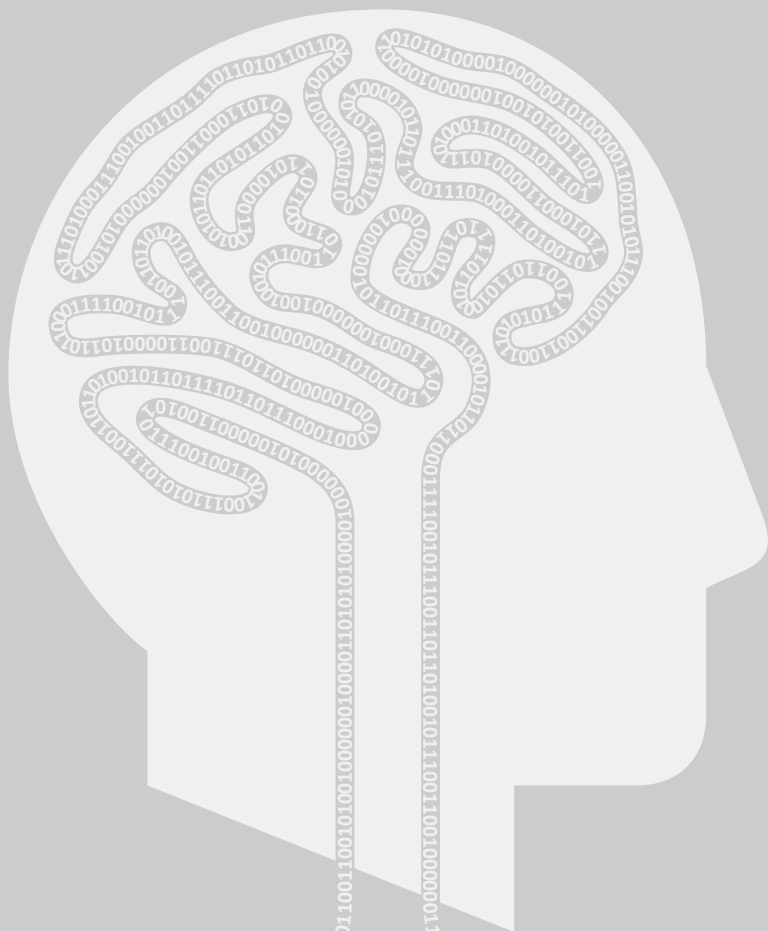
10

Dankwoord

Flink wat mensen hebben, ieder op eigen wijze, hun steentje bijgedragen aan dit proefschrift. Hierbij wil ik een aantal van hen bedanken.

Om te beginnen wil ik mijn co-promotoren, dr. ir. Hugo de Jong en dr. Birgitta Velthuis, en mijn promotor, prof. dr. ir. Max Viergever, bedanken. Hugo, jouw openheid en je betrokken en doelgerichte begeleiding van mijn onderzoek heb ik erg gewaardeerd. Ik vond het prettig dat je, ondanks je drukke agenda, altijd bereikbaar was voor een goed, informeel gesprek. Birgitta, zonder jouw bijdrage hadden er enkel computersimulaties in dit proefschrift gestaan. Bedankt voor je begeleiding en advies op radiologisch gebied. Max, ik vond je betrokkenheid en de nauwgezetheid van je reviews fascinerend, zeker gezien het grote aantal promoties dit jaar.

De leden van de beoordelingscommissie, prof. dr. G.J. Biessels, prof. dr. J. Hendrikse, prof. dr. B.W. Raaymakers, prof. dr. W.M. Prokop en prof. dr. E.T. van Bavel, wil ik bedanken voor hun bereidheid tot het beoordelen van dit proefschrift.

Beste dr. Jan Willem Dankbaar, bedankt voor al je advies en invulling op radiologisch gebied. Jij, en ook Alexander, hebben me daarnaast ontzettend geholpen door het scoren van alle scans. Het zou mooi zijn als we de komende jaren samen nog wat meer onderzoeken kunnen opzetten. Pieter, ook met jou heb ik fijn samen kunnen werken.

De nog niet genoemde betrokkenen bij het AIRSPACE project, dr. Henk Marquering, dr. Wiro Niessen, dr. Mariëlle Philippens, dr. Julien Milles, dr. ir. Jurgen de Hart, Alan, Jaap, Emilie, Fahmi, Renan, Luca en de mensen van STW, wil ik bedanken voor de prettige samenwerking en verbreding van ons onderzoek. Het is mooi om te zien hoe nieuw ontwikkelde methoden hun weg vinden naar ander onderzoek of naar de praktijk.

Dr. Kohsuke Kudo, *your contributions to the second chapter were very much appreciated. Thank you, not only for your help with the digital perfusion phantom, but also for your many valuable contributions to brain perfusion imaging research in general.*

Andere namen die ook zeker niet mogen ontbreken zijn die van mijn kamergenoten. Dat zijn, in chronologische volgorde, Mattijs, Alan, Casper, Jaap, Robert, Sandra, Remco en Wilco. Bedankt voor de altijd uitstekende sfeer en alle goddelijke kopjes espresso. Alan, nu zal je zo onderhand toch wel een goed woordje Nederlands moeten spreken; bedankt voor het prettige en ontspannen samenwerken in de eerste jaren van mijn onderzoek. Casper, het doet me een plezier dat ik jou, naast het klimmen, de komende jaren nog regelmatig als klifio zal tegenkomen in ons UMC. Jaap, jouw enthousiasme voor fancy algoritmen, brute computers en ongebruikelijke woorden is jouw kracht; laat dat enthousiasme zijn werk doen.

De heren klinisch fysici, Arnold Schilham, Bart Vermolen, Rob van Rooij en Bastiaan van Nierop, wil ik bedanken voor alle gezellige lunches, koffie, ijs, kattenfilmpjes en gesprekken van hoog niveau aan de koffietafel. Ook gaat mijn dank uit naar alle laboranten die onze koffie dikwijls aanvulden met een heerlijk stuk taart.

10

Hans, Gitta en alle oud-collega's van SVI wil ik bedanken voor de leuke afwisseling in de eerste jaren van mijn promotie. Tijdens mijn maandelijkse tweedaagse uitstapje naar Hilversum voelde het vaak alsof ik nooit weg was geweest. De sfeer was dan als vanouds en vaak werkte het ook inspirerend om even met een ander onderwerp bezig te zijn.

Ook wil ik graag mijn familie en vrienden bedanken. In het bijzonder Joris, Marcel en Wouter. Niet alleen voor onze prachtige studietijd in Eindhoven, maar ook omdat jullie, Joris en Marcel, als paranimf willen optreden. Ook kan ik wel kan zeggen dat jullie, Marcel en Wouter, mij geïnspireerd hebben om toch nog aan een promotieonderzoek te beginnen.

11

Publications

Peer-reviewed Publications

Horsch AD, Dankbaar JW, Stemerdink TA, Bennink E, Seeters T van, Kappelle LJ, Hofmeijer J, Jong HWAM de, Graaf Y van der, Velthuis BK, on behalf of the DUST investigators. Imaging findings associated with space-occupying edema in patients with large middle cerebral artery infarcts. *American Journal of Neuroradiology*. 2016:10.3174/ajnr.A4637.

Bennink E, Oosterbroek J, Horsch AD, Dankbaar JW, Velthuis BK, Viergever MA, Jong HWAM de. Influence of thin slice reconstruction on CT brain perfusion analysis. *PLOS ONE*. 2015;10(9):e0137766.

Bennink E, Horsch AD, Dankbaar JW, Velthuis BK, Viergever MA, Jong HWAM de. CT perfusion analysis by nonlinear regression for predicting hemorrhagic transformation in ischemic stroke. *Medical Physics*. 2015;42:4610-4618.

Oosterbroek J, Bennink E, Philippens MEP, Raaijmakers CPJ, Viergever MA, Jong HWAM de. Comparison of DCE-CT models for quantitative evaluation of Ktrans in larynx tumors. *Physics in Medicine and Biology*. 2015;60(9):3759-3773.

Cremers CH, Dankbaar JW, Vergouwen MD, Vos PC, Bennink E, Rinkel GJ, Velthuis BK, Schaaf IC van der. Different CT perfusion algorithms in the detection of delayed cerebral ischemia after aneurysmal subarachnoid hemorrhage. *Neuroradiology*. 2015;57(5):469-474.

Riordan AJ, Bennink E, Dankbaar JW, Viergever MA, Velthuis BK, Smit EJ, Jong HWAM de. Comparison of partial volume effects in arterial and venous contrast curves in CT brain perfusion imaging. *PLOS ONE*. 2014;9(5);e0097586.

Bennink E, Riordan AJ, Horsch AD, Dankbaar JW, Velthuis BK, Jong HWAM de. A fast nonlinear regression method for estimating permeability in CT perfusion imaging. *Journal of Cerebral Blood Flow and Metabolism*. 2013;33:1743-1751.

Riordan AJ, Bennink E, Viergever MA, Velthuis BK, Dankbaar JW, Jong HWAM de. CT brain perfusion protocol to eliminate the need for selecting a venous output function. *American Journal of Neuroradiology*. 2013;34(7):1353-1358.

Papers Submitted for Journal Publication

Horsch AD, Velthuis BK, Bennink E, Jong HWAM de, Seeters T van, Stemerdink T, Worp HB van der, Kappelle LJ, Hofmeijer J, Graaf Y van der, Mali WPTM, Dankbaar JW, on behalf of the DUST investigators. Blood-brain barrier permeability measurements with CT-perfusion predict prominent edema in acute ischemic stroke. Submitted for journal publication. 2016.

11

Barros RS, Bennink E, Posthuma J, Oosterbroek J, Majoie C, Jong HWAM de, Olabarriaga SD, Marquering H. High performance analysis of compressed dynamic CT perfusion image data for acute care of ischemic stroke. Submitted for journal publication. 2015.

Bennink E, Oosterbroek J, Kudo K, Viergever MA, Velthuis BK, Jong HWAM de. A fast non-linear regression method for CT brain perfusion analysis. Submitted for journal publication. 2015.

Papers in Conference Proceedings
Barros RS, Bennink E, Posthuma J, Oosterbroek J, Majoie C, Jong HWAM de, Olabarriaga SD, Marquering H. High performance analysis of compressed dynamic CT perfusion image data for acute care of ischemic stroke. In: *Proceedings of HPC-MICCAI*. 2015.

Bennink E, Oosterbroek J, Viergever MA, Velthuis BK, Jong HWAM de. A non-linear regression method for CT brain perfusion analysis. In: *Proceedings of SPIE*. 2015;9417:94171Q.

Oosterbroek J, Bennink E, Dankbaar JW, Horsch AD, Viergever MA, Velthuis BK, Jong HWAM de. Predicting stroke outcome using DCE-CT measured blood velocity. In: *Proceedings of SPIE*. 2015;9417:94170I.

Vos PC, Bennink E, Jong HWAM de, Velthuis BK, Viergever MA, Dankbaar JW. Automated prediction of tissue outcome after acute ischemic stroke in computed tomography perfusion images. In: *Proceedings of SPIE*. 2015;9414:941412.
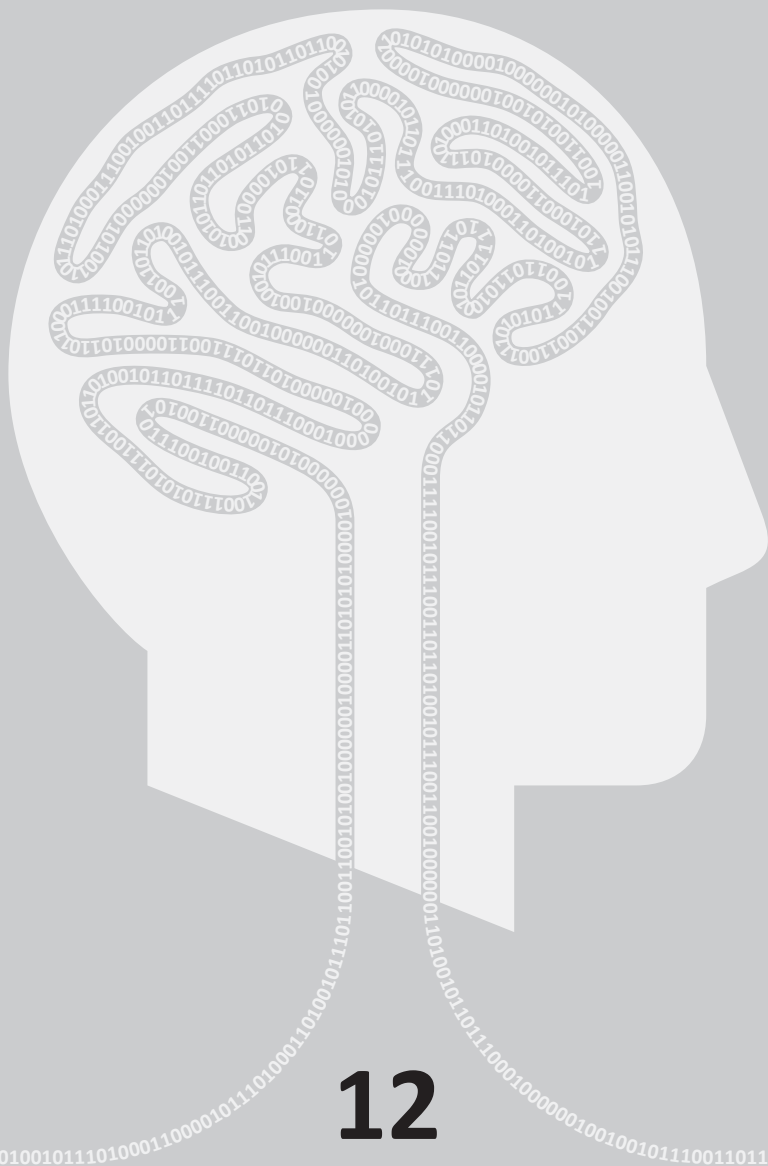
12

Curriculum Vitae

Edwin Bennink (Deventer, 1982) finished his pre-university education in 2000 in Deventer. Thereafter, he started a study in Biomedical Engineering at the Eindhoven University of Technology. During his specialization in biomedical image analysis, in the group of prof. dr. ir. Bart ter Haar Romeny, he went to Singapore and did research on brain atlases for intra-operative MR guidance, under the supervision of prof. dr. Wieslaw Nowinski. Supervised by dr. ir. Hans van Assen, he received the MSc degree (cum laude) in 2007 with his research on cardiac vessel detection and enhancement in cryomicrotome imaging.

From 2007 to 2011 he worked as a senior software developer for Scientific Volume Imaging, makers of the Huygens software for deconvolution, analysis and visualization of fluorescence microscopy images.

In September 2011, he started his research project on quantitative CT brain perfusion analysis at the University Medical Center Utrecht, under supervision of dr. ir. Hugo de Jong, dr. Birgitta Velthuis and prof. dr. ir. Max Viergever. This resulted in this PhD thesis.

As of November 2015, he started working as a scientific software developer and researcher at the Image Sciences Institute in Utrecht.

12